UNIVERSITY OF CALIFORNIA, IRVINE

Vascularized Organs-on-a-Chip for Human Disease Modeling and Drug Screening

DISSERTATION

Submitted in partial satisfaction of the requirements for the degree of

DOCTOR OF PHILOSOPHY

in Biological Sciences

by

Duc Thanh Thien Phan

Dissertation Committee

Professor Christopher C.W. Hughes, Chair

Professor Abraham P. Lee

Professor Matthew A. Inlay

Professor Melissa B. Lodoen

Professor Elliot E. Hui

2018

DEDICATION

To my parents and my godmother Hanna, for their unconditional love and support.

To Veronica, for her love and patience to walk with me through the ups and downs.

To my advisor Dr. Christopher C.W. Hughes, for his trust when others did not believe in me.

To science, for your gracefulness to let me poke a tiny hole through your boundary.

To humanity, here is my small contribution.

TABLE OF CONTENTS

LIST OF FIGURES

LIST OF TABLES

ACKNOWLEDGEMENTS

I would like to thank:

- My thesis advisor, **Dr. Christopher C.W. Hughes** for his trust, guidance, and support.
- My thesis committee members, **Dr. Abraham P. Lee, Dr. Matthew A. Inlay, Dr. Melissa B. Lodoen, and Dr. Elliot E. Hui**, for their valuable feedback throughout my graduate study.
- My collaborators, **Dr. Xiaolin Wang, Dr. Agua Sobrino, Da Zhao, and Brianna Craver,** for their significant contributions to my research.
- **Former and current members of Hughes Lab**, for their assistance and moral support.
- **Dr. Emma Flores-Kim** and **Dr. Christopher Schaumburg** for their advice and support to my professional development.
- **Friends and colleagues** whom I got to know throughout the years at UC Irvine.
- **Jiu-jitsu, my instructors Felipe Fogolin and AJ Albert, as well as many training partners** for teaching me resilience and perseverance.
- **Coffee**, for giving me strength to change the things I can, and allowing me to accept the things I cannot.

Sources of funding included:

- The National Institutes of Health (NIH) grants: UG3 (HL141799), UH2/UH3 (TR000481), and R01-PQD5 (CA180122).
- The National Aeronautics and Space Administration (NASA) grant: NNX13AD59G.
- UC Irvine I3 Exploratory Grant.

CURRICULUM VITAE

Duc Thanh Thien Phan

Education

Ph.D., Biological Sciences 2018
Field of Study: Vascular Biology/Microphysiological Systems
Ayala School of Biological Sciences, University of California, Irvine

M.S., Biological Sciences 2018
Ayala School of Biological Sciences, University of California, Irvine

B.S. (Cum Laude), Biomedical Engineering: Premedical 2012
Henry Samueli School of Engineering, University of California, Irvine

A.S. (with Honors), Biology 2010
Orange Coast College

Research Experience

Graduate Student Researcher 2014 – 2018
Department of Molecular Biology & Biochemistry
University of California, Irvine

Thesis Advisor: Dr. Christopher C.W. Hughes
Dissertation: Vascularized Organs-on-a-chip for Human Disease Modeling and Drug Screening

Laboratory Assistant 2012 – 2014
Department of Molecular Biology & Biochemistry
University of California, Irvine

Principal Investigator: Dr. Christopher C.W. Hughes

Teaching Experience

Teaching Assistant 2017 – 2018
Department of Molecular Biology & Biochemistry
University of California, Irvine

Courses: Molecular Biology Laboratory, Immunology, Biochemistry.

Publications

Wang X, Zhao D, **Phan DT**, Sun Q, Pei J, Liu J, Chen X, Yang B, Hughes CC, Zhang W, Lee AP. **A hydrostatic pressure-driven passive micropump enhanced with siphon-based autofill functions.** Lab Chip (In revision).

Urban G, Bache K, **Phan DT**, Sobrino A, Shmakov AK, Hachey SJ, Hughes CC, Baldi P. **Deep learning for drug discovery and cancer research: Automated-analysis of vascularization images**. IEEE/ACM Transactions on Computational Biology and Bioinformatics (Accepted).

Wang X*, **Phan DT***, George SC, Hughes CC, Lee AP. **3D anastomosed microvascular network model with living capillary networks and endothelial cell-lined microfluidic channels**. Methods Mol Bio. 2017;1612:325-344. (*** co-first authors**)

Phan DT, Bender RH, Andrejecsk JW, Sobrino A, Hachey SJ, George SC, Hughes CC. **Blood-brain barrier-on-a-chip: microphysiological systems that capture the complexity of the blood-central nervous system interface.** Exp Bio Med (Maywood). 2017.

Phan DT*, Wang X*, Craver BM, Sobrino A, Zhao D, Chen JC, Lee LY, George SC, Lee AP, Hughes CC. **A vascularized and perfused organ-on-a-chip platform for large-scale drug screening applications.** Lab Chip. 2017 Jan 31;17(3):511-520. (*** co-first authors**)

Sobrino A *, **Phan DT** *, Datta R, Wang X, Hachey SJ, Romero-López M, Gratton E, Lee AP, George SC, Hughes CC. **3D microtumors in vitro supported by perfused vascular networks**. Sci Rep. 2016 Aug 23;6:31589. (*** co-first authors**)

Arulmoli J, Wright HJ, **Phan DT**, Sheth U, Que RA, Botten GA, Keating M, Botvinick EL, Pathak MM, Zarembinski TI, Yanni DS, Razorenova OV, Hughes CC, Flanagan LA. **Combination scaffolds of salmon fibrin, hyaluronic acid, and laminin for human neural stem cell and vascular tissue engineering.** Acta Biomater. 2016 Oct 1;43:122-38.

Wang X, **Phan DT**, Zhao D, George SC, Hughes CC, Lee AP. **An on-chip microfluidic pressure regulator that facilitates reproducible loading of cells and hydrogels into microphysiological system platforms.** Lab Chip. 2016 Mar 7;16(5):868-76.

Wang X *, **Phan DT** *, Sobrino A, George SC, Hughes CC, Lee AP. **Engineering anastomosis between living capillary networks and endothelial cell-lined microfluidic channels.** Lab Chip. 2016 Jan 21;16(2):282-90. (*** co-first authors**)

Newman AC, Chou W, Welch-Reardon KM, Fong AH, Popson SA, **Phan DT**, Sandoval DR, Nguyen DP, Gershon PD, Hughes CC. **Analysis of stromal cell secretomes reveals a critical role for stromal cell-derived hepatocyte growth factor and fibronectin in angiogenesis.** Arterioscler Thromb Vasc Biol. 2013 Mar;33(3):513-22.

Presentations

Phan DT and Hughes CC. **A perfused blood-brain barrier-on-a-chip.** Vascular Biology 2017. 10/15 – 19/2017. Monterey, CA. (Keynote presentation)

Phan DT, Craver BM, Flanagan LA, Hughes CC. **A microphysiological system to model the human neurovascular unit.** The 19th International Vascular Biology Meeting. 10/30 – 11/05/2016. Boston, MA. (Poster presentation)

Phan DT, Wang X, Lee AP, Limoli CL, Flanagan LA, Hughes CC. **Development of a 3-D *in vitro* Perfused Human Neurovascular Unit-On-Chip.** Tissue Engineering and Regenerative Medicine International Society World Congress. 09/08 – 09/11/2015. Boston, MA. (Poster presentation)

Phan DT, Wang X, Lee AP, George SC, Hughes CC. **Improving anastomosis between microfluidic channels and perfused capillary networks in cultured 3D human microtissues.** Biomedical Engineering Society Annual Meeting. 10/22 – 10/25/2014. San Antonio, TX. (Poster presentation)

ABSTRACT OF THE DISSERTATION

Vascularized organs-on-a-chip for human disease modeling and drug screening

By

Duc Thanh Thien Phan

Doctor of Philosophy in Biological Sciences

University of California, Irvine, 2018

Professor Christopher C.W. Hughes, Chair

Despite continuous advances in studying human diseases and drug screening methodology, only a small fraction of drug candidates achieve approval for clinical use due to the lack of efficacy and/or adverse effects. A major challenge in studying human diseases and in identifying drug candidates that target these diseases, is the lack of an effective model that captures different aspects of human physiology. Studies are still heavily reliant on monolayer cell cultures or on animal models, neither of which can fully recapitulate the human body and its disease stages. Microphysiological systems/organs-on-a-chip (MPS/OOC) are designed to bridge the gap between monolayer cell culture and animal models. This body of research aims to develop novel MPS/OOC supported by a true living human vasculature to mimic human organ functions, model human diseases, and utilize these platforms to advance drug discovery and development.

CHAPTER 1

Introduction

1.1 Challenges in studying human diseases and developing new therapeutic drugs

Despite continuous advances in studying human diseases and drug screening methodology, only a small fraction of drug candidates achieve approval for clinical use. The estimated annual cost for new drug research and development is $2.6 billion per marketed drug, yet over 80% of drug candidates fail during phase II and later due to the lack of efficacy and/or adverse effects [1]. For instance, Alzheimer's disease (AD) remains an uncured disease, and several large drug trials designed to lower the amyloid peptide load in the brain of patients with Alzheimer's disease have failed in the past decade due to their lack of efficacy [2]. Cancer is the second leading cause of death in the U.S, yet many adjuvant and combination anticancer therapies often carry adverse effects in the cardiovascular system, such as amplifying cardiotoxicity and increasing risk of heart failure in patients [3]. Evidently, the current strategy to study human diseases and develop new drugs to target them is not as effective as it should be.

A major challenge in studying human diseases and in identifying drug candidates that target these diseases, is the lack of an effective model that captures different aspects of human physiology. Studies are still heavily reliant on 2-dimensional (2D) cultures of a single cell type or on animal models, neither of which can fully mimic the complexities of the human body and its disease stages. 2D monocultures, while they are easier and simpler to adapt and study in the laboratory, cannot recapitulate the 3-dimensional (3D) structure of human tissues and organs, as well as tissue-specific, multicellular interactions that are present *in vivo*. Conversely, while animal models can introduce the 3D tissue structures and organ functions, they are expensive and time-consuming, yet cannot truly capture human disease due to differences in anatomy and physiology between rodents and humans. For instance, drug metabolism in rodents is different from human, so toxic effects often cannot be detected during animal studies [4]. More

importantly, not all human diseases, for instance neurodenerative diseases such as amyotrophic lateral sclerosis or Alzheimer's disease, can be studied using animal models as some diseases are human-specific, or their humanized-animal models cannot reflect all pathological aspects found in human [5].

These limitations have led to a growing interest in developing 3D *in vitro* cell culture models to bridge the gap between 2D monocultures and animal models. The majority of 3D cell culture models are in static form, where cells are dispersed in a mixture of natural or synthetic extracellular matrix (ECM) or self-assembled into cellular clusters known as organoids [6, 7]. While these 3D static models have been more effective than 2D monoculture models to study the molecular basis of cell-cell and cell-matrix interactions, they still have limitations in representing the organ-level architecture and multi-organ interactions through the blood circulation system. Blood flow through the vasculature delivers nutrients and oxygen to organs, removes metabolic waste, and introduces dynamic mechanical and chemical cues to the tissue microenvironment that influence organ development and function in health and disease [8-10]. Thus, there is a need for 3D cell culture models that incorporate dynamic fluid flow to mimic the blood circulation system.

1.2 Microphysiological Systems and Organs-on-a-chip

Microphysiological systems (MPS) are designed to further bridge the gap between 2D monocultures, 3D static cell culture models, and animal models. These systems introduce dynamic fluid flow to mimic the blood circulation system within a 3D environment that encapsulates human cells to better model the native tissues. The goal in developing MPS is not to re-create a whole living organ, but a tissue unit with relevant cellular structures and functions of that particular organ [8, 11]. MPS combine advances in microfluidic technology and 3D cell culture

techniques to recapitulate a substantial level of complexity found *in vivo,* including 3D heterogeneous cellular structure, cell–cell and cell-matrix interactions, the presence of a complex extracellular matrix (ECM), perfused vasculature, and biomechanical forces (*e.g.* shear forces generated by fluid flow) [11]. Because MPS utilizes photolithographic techniques used in computer microchip manufacturing to create the housing micro-structures for cells and the ECM, they are also known as "organs-on-a-chip" (OOC). Thus, the two terms MPS/OOC have been used interchangeably to describe this category of 3D culture platforms with dynamic fluid flow.

In recent years, efforts to develop MPS/OOC have been focused on recreating human organs such as heart, liver, lung, and brain, as well as "diseases-on-a-chip" to model human diseases for basic science research [12-16]. While these models have introduced dynamic fluid flow to 3D cell culture, and demonstrated significant improvements in mimicking human organs and disease stages, they still lack a true living vasculature that has a critical role in delivering nutrients, oxygen, and many drugs *in vivo*. In the body, the vasculature is formed by endothelial cells (EC) and supporting cells such as pericytes (PC), smooth muscle cells, and stromal cells [17]. Together, they create a barrier structure, and play active roles in regulating molecular transportation across this barrier. While some MPS/OOC have introduced EC into their systems, most stop short at simply culturing a monolayer of EC along the surfaces of a pre-fabricated microfluidic channel. This approach is a step forward in MPS/OCC development, but it cannot fully capture the structural and functional complexity of the vasculature *in vivo*. Vascular development *in vivo* is a complex, multi-step process [17, 18]. However, vascular formation and development has been studied extensively, and certain aspects of this process have been re-created *in vitro* [18-20]. Thus, it is possible to re-create a living vasculature and incorporate it into MPS/OOC through understanding and harnessing this multi-step process.

1.3 Vasculogenesis and angiogenesis

Vasculogenesis

Vasculogenesis is the process of forming blood vessels *de novo* by EC during embryo development. Early vascularization begins when angioblasts differentiate into different types of EC and hematopoietic stem cells differentiate into blood cells, and together they form blood islands in the mesoderm of the yolk sac [17, 18]. Angioblasts migrate to developing organs as the embryo continues to grow, and form a primitive plexus at the base of the heart tube. This primitive plexus is the starting point for expansion and remodeling of a vascular network through the process of angiogenesis [18, 21].

Angiogenesis

Angiogenesis is the process of forming blood vessels from a pre-existing vasculature, where new vessels sprout out from mature vessels and subsequently remodel to create an intricate vascular network [21, 22]. Angiogenesis itself is a multi-step process consisting of degradation of the basement membrane, sprouting of EC into the ECM, lumen formation, anastomosis, and formation of a new basement membrane [18, 19, 21]. Angiogenesis occurs in response to angiogenic stimuli and is highly coordinated by EC and the perivascular cells. As EC become activated by angiogenic factors, they secrete destabilizing factors and matrix proteases, and migrate into the ECM [21]. As EC continue to sprout out from the existing vessel, they align into cords and form intracellular vacuoles. Lumens of neighboring EC then fuse to form an elongated, intercellular lumen. EC are now polarized with a basal surface facing the ECM and an apical surface facing the lumen. Lumenized vessels can either continue to extend, branch out, or fuse with adjacent vessels in a process called anastomosis [21]. This process continues until a

mature vascular network is formed, in which EC return to a quiescent stage, re-establish a mature basement membrane, and recruit perivascular cells (SMC and/or pericytes) back to the basal surface [21].

1.4 Vascularized MPS and OOC

While various *in vitro* vascular models, both in 2D and 3D, have long been established, the majority are still limited to static culture systems [19]. Within the 3D vascular model category, vasculogenesis and angiogenesis can be recapitulated *in vitro*, but due to the static culture environment, these vessels are not often perfusable [19]. In recent years, attempts to create 3D perfused vascular models have been made [23]. However, not all methods are suitable to incorporate into MPS/OOC for large-scale modeling of human diseases and drug screening applications. It is our vision to incorporate a true living vasculature, capable of supporting tissue survival in the MPS/OOC to model human diseases, and to utilize these platforms to improve the drug-development pipeline.

Our strategy to achieve this objective is divided into 3 steps (Figure 1.1). At the fundamental level (Step 1), we will combine knowledge in vasculogenesis and angiogenesis with advances in microfluidic technology to create a vascularized MPS that is capable of scaling up. This vascularized MPS/OOC is a generic human micro-tissue, consisting of a perfused, living vascular network with associated perivascular cells, embedded in a 3D extracellular environment. At the intermediate level (Step 2), the vascularized MPS/OOC is transformed into a tissue-specific MPS, such as a vascularized micro-brain or vascularized micro-liver, by optimizing the cellular and extracellular components specific to that tissue/organ in the human body. At the top level (Step 3), this tissue-specific MPS/OOC is transformed into a disease-specific MPS, such as vascularized micro-tumor in the brain or liver, by manipulating or

disrupting cellular homeostasis. We hope this strategy will not only address the current challenges in disease modeling and drug development, but also contribute to future research breakthroughs.

1.5 References

1. DiMasi, J.A., H.G. Grabowski, and R.W. Hansen, *Innovation in the pharmaceutical industry: New estimates of R&D costs.* J Health Econ, 2016. **47**: p. 20-33.
2. Anderson, R.M., et al., *Why do so many clinical trials of therapies for Alzheimer's disease fail?* Lancet, 2017. **390**(10110): p. 2327-2329.
3. Albini, A., et al., *Cardiotoxicity of anticancer drugs: the need for cardio-oncology and cardio-oncological prevention.* J Natl Cancer Inst, 2010. **102**(1): p. 14-25.
4. Martignoni, M., G.M. Groothuis, and R. de Kanter, *Species differences between mouse, rat, dog, monkey and human CYP-mediated drug metabolism, inhibition and induction.* Expert Opin Drug Metab Toxicol, 2006. **2**(6): p. 875-94.
5. Brehm, M.A., et al., *Overcoming current limitations in humanized mouse research.* J Infect Dis, 2013. **208 Suppl 2**: p. S125-30.
6. Mroue, R. and M.J. Bissell, *Three-dimensional cultures of mouse mammary epithelial cells.* Methods Mol Biol, 2013. **945**: p. 221-50.
7. Sato, T. and H. Clevers, *Growing self-organizing mini-guts from a single intestinal stem cell: mechanism and applications.* Science, 2013. **340**(6137): p. 1190-4.
8. Bhatia, S.N. and D.E. Ingber, *Microfluidic organs-on-chips.* Nat Biotechnol, 2014. **32**(8): p. 760-72.
9. Ingber, D.E., *Mechanobiology and diseases of mechanotransduction.* Ann Med, 2003. **35**(8): p. 564-77.
10. Mammoto, T., A. Mammoto, and D.E. Ingber, *Mechanobiology and developmental control.* Annu Rev Cell Dev Biol, 2013. **29**: p. 27-61.
11. Low, L.A. and D.A. Tagle, *Tissue chips - innovative tools for drug development and disease modeling.* Lab Chip, 2017. **17**(18): p. 3026-3036.
12. Brown, J.A., et al., *Recreating blood-brain barrier physiology and structure on chip: A novel neurovascular microfluidic bioreactor.* Biomicrofluidics, 2015. **9**(5): p. 054124.
13. Esch, M.B., et al., *Modular, pumpless body-on-a-chip platform for the co-culture of GI tract epithelium and 3D primary liver tissue.* Lab Chip, 2016. **16**(14): p. 2719-29.
14. Huh, D., et al., *Reconstituting organ-level lung functions on a chip.* Science, 2010. **328**(5986): p. 1662-8.
15. Jeon, J.S., et al., *Human 3D vascularized organotypic microfluidic assays to study breast cancer cell extravasation.* Proc Natl Acad Sci U S A, 2015. **112**(1): p. 214-9.
16. Mathur, A., et al., *Human iPSC-based cardiac microphysiological system for drug screening applications.* Sci Rep, 2015. **5**: p. 8883.
17. Potente, M. and T. Makinen, *Vascular heterogeneity and specialization in development and disease.* Nat Rev Mol Cell Biol, 2017. **18**(8): p. 477-494.
18. Patan, S., *Vasculogenesis and angiogenesis.* Cancer Treat Res, 2004. **117**: p. 3-32.
19. Tahergorabi, Z. and M. Khazaei, *A review on angiogenesis and its assays.* Iran J Basic Med Sci, 2012. **15**(6): p. 1110-26.
20. Vailhe, B., D. Vittet, and J.J. Feige, *In vitro models of vasculogenesis and angiogenesis.* Lab Invest, 2001. **81**(4): p. 439-52.
21. Carmeliet, P. and R.K. Jain, *Molecular mechanisms and clinical applications of angiogenesis.* Nature, 2011. **473**(7347): p. 298-307.
22. Chung, A.S. and N. Ferrara, *Developmental and pathological angiogenesis.* Annu Rev Cell Dev Biol, 2011. **27**: p. 563-84.

23. Kim, S., et al., *Vasculature-On-A-Chip for In Vitro Disease Models.* Bioengineering (Basel), 2017. **4**(1).

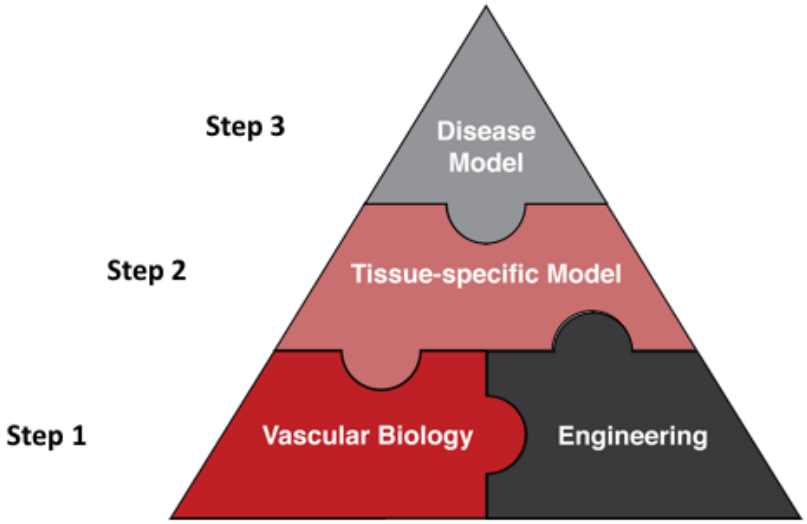

Figure 1.1: Strategy to develop vascularized organs-on-a-chip for human disease modeling and drug screening. At the fundamental level (Step 1), knowledge in vasculogenesis and angiogenesis is combined with advances in microfluidic technology to create a vascularized MPS/OOC that is capable of scaling up. At the intermediate level (Step 2), the vascularized MPS/OOC is transformed into a human tissue-specific MPS/OCC. At the top level (Step 3), tissue-specific MPS/OOC is transformed into a human disease-specific MPS/OOC.

CHAPTER 2

Engineering anastomosis between living capillary networks and endothelial cell-lined microfluidic channels enhances physiological leak-free perfusion

Xiaolin Wang, ‡ Duc T.T. Phan, ‡ Steven C. George, Christopher C.W. Hughes * and Abraham P. Lee *

(‡ Contributed equally as first authors, * Contributed equally as senior corresponding authors)

Originally published in Lab on a Chip 2016, 16:282-290

2.1 Abstract

This paper reports a method for generating an intact and perfusable microvascular network that connects to microfluidic channels without appreciable leakage. This platform incorporates different stages of vascular development including vasculogenesis, endothelial cell (EC) lining, sprouting angiogenesis, and anastomosis in sequential order. After formation of a capillary network inside the tissue chamber via vasculogenesis, the adjacent microfluidic channels are lined with a monolayer of ECs, which then serve as the high-pressure input ("artery") and low pressure output ("vein") conduits. To promote a tight interconnection between the artery/vein and the capillary network, sprouting angiogenesis is induced, which promotes anastomosis of the vasculature inside the tissue chamber with the EC lining along the microfluidic channels. Flow of fluorescent microparticles confirms the perfusability of the lumenized microvascular network, and minimal leakage of 70 kDa FITC-dextran confirms physiologic tightness of the EC junctions and completeness of the interconnections between artery/vein and the capillary network. This versatile device design and its robust construction methodology establish a physiological transport model of interconnected perfused vessels from artery to vascularized tissue to vein. The system has utility in a wide range of organ-on-a-chip applications as it enables the physiological vascular interconnection of multiple on-chip tissue constructs that can serve as disease models for drug screening.

2.2 Introduction

The cardiovascular-based circulation system plays a vital role in maintaining homeostasis of the human body. The blood vessel system comprises a closed network of arteries, veins and capillaries that allow blood to circulate throughout the body for gas exchange and mass transportation, which is essential to maintaining organ viability. Therefore, in order to mimic the characteristics and functions of organs *in vitro*, it is necessary to integrate a functional 3D microvasculature system for a more physiological organ-on-a-chip [1, 2].

Towards this goal several research groups have developed different 3D *in vitro* microvascular models using microfluidic technology to better study vascular biology [3]. Microfluidic structure design allows for the confinement of cells to restricted regions with controlled cellular interactions based on patterned tissue chamber designs. Furthermore, microfluidic flow control can establish complex microenvironment concentrations at physiological levels by regulating chemical factors (*e.g.* molecular gradients) or mechanical factors (*e.g.* shear force from interstitial flow). One strategy for developing a 3D microvascular model is to create microfabricated vessel scaffolds by lining microfluidic channels with ECs. Since the geometries of these scaffolds are pre-determined by the microfabricated patterns, the imposed shear stress on the lined ECs can be precisely controlled based on the microchannel dimension and applied flow rate [4-6]. An alternative strategy is to seed cells in 3D extracellular matrix (ECM), which allows spontaneous formation and remodeling of vascular networks through vasculogenesis and angiogenesis [7-12]. Compared to the EC lining strategy, this strategy closely mimics vascular development *in vivo*. However, the disadvantage is that although the microvascular morphology (*e.g.* number of branches, average branch length, average vessel diameter, *etc.*) can be regulated by different control factors (*e.g.* paracrine signaling, cell-seeding

density and hydrogel mechanical properties, *etc.*), the microvascular network pattern cannot be well controlled and easily perfused [13].

Recognizing the need to better replicate the *in vivo* vasculature, we have developed a novel microfluidic device with robust methodology that combines the above-mentioned two strategies into an advanced 3D microvascular network model. This model would need to closely emulate the intact physiological blood vessel network with tight interconnections between artery/vein and capillary vessel network. Further, it is essential that these interconnections be without non-physiological leakage. Therefore, in order to mimic the complete and contiguous microvascular network with intact and perfusable lumen, the engineering artery/vein and capillary network must fuse with each other tightly in a process known as anastomosis [14]. In our design, the capillary network is induced *via* vasculogenesis in a middle tissue chamber and EC linings along the microfluidic channel on either side serve as the artery and vein. Anastomosis is induced bi-directionally with our methodology, guaranteeing a good connection between EC lining along microfluidic channel and capillaries inside the tissue chamber. First, some ECs will migrate out from tissue chamber and proliferate along microfluidic channel during vasculogenesis process, facilitating the connection with subsequent EC lining. Second, sprouting of lined EC monolayer on the matrix interface is induced to invade into ECM and form connection with the capillary network inside tissue chamber. Thus, this microfluidic platform enables multiple stages of microvascular network development such as vasculogenesis, EC lining, angiogenesis, and anastomosis to take place on a single platform. Furthermore, perfusion of 70 kDa FITC-dextran validates tight connection between the lined ECs inside microfluidic channels and the capillary network inside the tissue chamber without non-physiological leakage. The significance of this work is in the prevention of non-physiologic leakage from vasculature into ECM, which is critically important for drug screening applications [15]. In

addition, the platform can provide a promising avenue for the integration of multiple organ-on-chips towards the vision of body-on-chip by establishing the vascular interfaces from artery to vein [16, 17].

2.3 Materials and Methods

Microfluidic Device Design

Figure 2.1 illustrated the concept of a decoupling device design by using four medium reservoirs with different hydrostatic pressures that could separately control flow to the tissue chamber and along the microfluidic channel. The former resulted in interstitial flow across the tissue chamber that induced vasculogenesis, and the latter induced shear stress on the lined EC within the microfluidic channels. The decoupling of these two microfluidic flows also allowed for precise control of the transendothelial flow conditions that promoted sprouting angiogenesis as well as formation and maintenance of anastomosis.

The entire device structure consisted of three central millimeter-sized diamond tissue chambers (1 × 2 mm) and two side square cross-sectional microfluidic channels (100 × 100 μm) (Figure 2.1B) that connected to the tissue chambers through a series of communication pores (Figure 2.1C). Based on the quantitative analysis of Laplace pressure at the gel–air interface, the widths of both communication pores and chamber-connecting channels were optimized to prevent gel bursting (or leaking) into side microfluidic channels from pressure built-up during the gel loading process (Figure 2.1S). In our design, the burst pressure ($P_{\text{burst-max}}$ = 3983 Pa) of communication pores with a width of 50 μm was much higher than the advancing pressure ($P_{\text{advancing-min}}$= 1655 Pa) of the chamber-connecting channels with a width of 200 μm, calculated based on the Young–Laplace equation [18]. Since there was a large pressure range (ΔP = 2328 Pa) between the burst pressure and advancing pressure, there was a low probability of gel bursting into the side microfluidic channels during loading, as long as the applied gel loading pressure was within the pressure boundary ($P_{\text{advancing-min}} < P_{\text{loading}} < P_{\text{burst-max}}$). Therefore, the communication pores functioned as capillary burst valves to prevent gel from flowing out of the tissue chambers and into the outer channels [19]. In addition, the hourglass shaped

communication pores, with gently sloping curved edges, were designed to precisely stop advancing gel at a specific position closest to the microfluidic channel ($D_{gel\text{-}max}$ = 20 μm) with relatively flat gel–air interface (Figure 2.1C). This enabled the formation of a smooth EC monolayer on the gel interface at the communication pore, a critical condition for EC lining and sprouting angiogenesis. Furthermore, since the time needed for vasculogenesis was longer than that for EC lining, the cell loading port configuration allowed EC lining at later days after embedding cells inside the tissue chambers for capillaries formation. Both cell loading inlet ports for the EC lining were designed with a wider opening than the media inlet ports in order to prevent cell blocking when introducing cells for EC lining (Figure 2.1D). In both cell loading outlet channels, an obstacle array was integrated as a sieve to concentrate cells inside the microfluidic channels during the EC lining process (Figure 2.1D). This procedure facilitated sufficient contact of ECs with the laminin-coated microfluidic channel, which was essential for EC lining.

Finite-element simulations on the pressure distribution and velocity profiles for the device were performed using COMSOL Multiphysics 4.3 (Comsol Inc., Burlington, MA, USA). In the 3D microfluidic model, the Brinkman equation was employed for momentum transportation through a porous fibrin gel confined in the tissue chamber and driven by the hydrostatic pressure drop. Due to the low permeability (1.5×10^{-13} m^2) of fibrin gels, which created high hydraulic resistance, only small volumes of media flowed into the tissue chamber. Furthermore, due to the fully symmetrical configuration of communication pores along both side microfluidic channels, the pressure drop across each tissue chamber from the top communication pore to the bottom one was almost the same ($\Delta P_{chamber}$ ~ 5 mm H_2O), which induced a uniform interstitial flow profile inside each tissue chamber to stimulate vasculogenesis (Figure 2.1E). When loading cells for EC lining, the particle tracing module was coupled with the fluidic flow module to track trajectories of cells inside the microfluidic

channel. The simulation result demonstrated that the loaded cells only travelled from cell loading inlet port to cell loading outlet port and did not enter the vertical section of side microfluidic channels by using withdrawal mode (Figure 2.1D).

The microfluidic device was made of polydimethylsiloxane (PDMS) (Sylgard-184, Dow Corning) by micro-molding from SU-8 patterned silicon wafers using standard soft lithography techniques. The height of the microfluidic channels and the tissue chambers were all 100 μm. After plasma bonding the microfluidic chip with the PDMS coated glass slide, four bottomless plastic vials were glued at four media reservoir ports using the PDMS mixed with curing agent. Fabricated devices were autoclaved at 121 °C for 30 minutes before being used for experiments.

Cell Culture

Human endothelial colony forming cell-derived ECs (ECFC-ECs) were isolated from cord blood as previously described [20] and expanded on gelatin-coated flasks in EGM-2 (Lonza). ECFC-ECs were transduced with lentivirus constructs (Addgene) to express blue fluorescent protein (BFP), green fluorescent protein (GFP), or mCherry fluorescent protein and used between passages 4–7. Normal human lung fibroblasts (NHLFs) were purchased from Lonza, cultured in DMEM (Corning) containing 10% Fetal Bovine Serum (FBS, Gemini Bio Products), and used between passages 5–8. All cell types were grown in a 37 °C/5% CO_2/20% O_2 incubator in 100% humidified air.

Experimental procedures and fluidic flow control

The cell–matrix mixture was prepared by suspending ECs (5×10^6 cells per mL) and NHLFs (5×10^6 cells per mL) in fibrinogen solution (10 mg mL^{-1}, Sigma-Aldrich) [21-23]. The suspension was then mixed with 50 U mL^{-1} thrombin (Sigma-Aldrich) for a final concentration of 3 U mL^{-1} and

quickly injected into tissue chambers through the gel loading port (A to B) using a micropipettor. The gel was allowed to polymerize in the incubator at 37 °C for 15 minutes. Next, laminin (1 mg mL^{-1}, Life Technologies) was introduced through the cell loading port (G to H, and I to J) to coat the inner surface of the microfluidic channels as the basement membrane. These four cell loading ports were then blocked by plugs, and EGM-2 with full supplements was loaded through the media reservoir ports (C to D, and E to F). Pre-coating the microfluidic channels with laminin before adding culture medium was crucial to stimulate EC adherence to PDMS when lining, as well as EC migration outward from the tissue chamber during vasculogenesis. The initial pressure drop to maintain the physiological level of mechanical stimuli on vasculogenesis was established by filling the reservoirs to different culture medium heights (V1: 23 mm H_2O, V2: 8 mm H_2O, V3: 18 mm H_2O, V4: 3 mm H_2O). After 12 hours, the fully supplemented EGM-2 within both channels were replaced by EGM-2 without basic fibroblast growth factor (bFGF) and vascular endothelial growth factor (VEGF), and leveled at the same initial pressure drop. After formation of a capillary network inside the tissue chambers *via* vasculogenesis, a pipette tip containing high density (2×10^7 cells per mL) ECs was inserted into the cell loading inlet port (I) and medium was withdrawn from the corresponding cell loading outlet port (J) until the cells filled up the microfluidic channel. The device was then incubated at 37 °C for 2 hours to allow ECs to adhere to all side walls, and reverse flow (J to I) was then gently applied to remove non-adhering ECs from the microfluidic channel. By re-establishing flow under the same initial pressure drop, adhered ECs elongated to form a monolayer in response to shear stress generated by the pressure drop along the microfluidic channel ($\Delta P_{channel}$ = 15 mm H_2O). Meanwhile, the basal-to-apical transendothelial flow across the matrix–cell interface pinned at communication pores triggered the transition of lined ECs from a quiescent to an invasive phenotype leading to sprouting angiogenesis [10, 24]. To promote the angiogenesis process, a positive VEGF gradient was

also utilized in our methodology [25, 26], which was induced by switching the medium inside "arterial" microfluidic channel to the fully supplemented EGM-2. After two days, the other microfluidic channel was lined with ECs using the same cell loading procedure, except that the hydrostatic pressure distribution (V1: 18 mm H_2O, V2: 3 mm H_2O, V3: 23 mm H_2O, V4: 8 mm H_2O) and the positive VEGF gradient direction were reversed.

Immunostaining and imaging

For immunostaining, the device was fixed by flowing 4% paraformaldehyde (Sigma-Aldrich) for 1 hour at room temperature, following by overnight PBS wash at 4 °C. Blocking, washing, antibody incubation, and nuclei staining steps were also conducted by flowing reagents through the microfluidic channels overnight at 4 °C. Static images and time-lapse image sequences were taken using a SPOT Pursuit High Speed Cooled CCD camera (SPOT Imaging).

Shear stress estimation along the microfluidic channels

The average wall shear stress along microfluidic channels is estimated based on the following equation [4]:

$$\bar{\tau} = \frac{4\mu\left(1+\varepsilon^2\right)V}{c^2}\ \frac{A}{P}$$

where μ is the dynamic viscosity of fluid flow, ε is the aspect ratio of microfluidic channel semi-minor axis c and semi-major axis b, V is the average fluid velocity inside the microfluidic channel, A is the cross-sectional area of the microfluidic channel, and P is the perimeter of the microfluidic channel.

Dextran perfusion and permeability quantification

For evaluating perfusion of microvascular networks, medium was replaced with DPBS with similar hydrostatic pressure profile, and the device was positioned onto a microscope stage. 70 kDa-FITC dextran (Sigma-Aldrich) was added to the reservoir with highest hydrostatic pressure to a final concentration of 50 μg mL−1 and allowed to perfuse through the microfluidic channel. A time-lapse image sequence was recorded for 15 minutes.

For vascular permeability quantification, the device was set up in a similar manner as described above. Once the device was mounted on the microscope stage, an image of background fluorescent intensity was acquired. After allowing FITC-dextran to fully perfuse the microvascular network for 15 minutes, time-lapse images were acquired every 15 minutes for a time course of 45 minutes. The diffusive component of the solute permeability coefficient P was calculated using the equation previously described [27], by quantifying background average fluorescence intensity (Ib), initial average fluorescence intensity (Ii) step change after FITC-dextran influx reached equilibrium at the initial time point, and final average fluorescence intensity (If) at the final time point, which can be expressed as:

$$P = \frac{D}{4} \times \left(\frac{I_f - I_i}{\Delta t} \right) \frac{1}{I_i - I_b}$$

where D is the average diameter of the microvessels, and Δt is the time interval between the initial time point and the final time point.

2.4 Results

Gel loading and vasculogenesis inside the tissue chamber

By optimizing the structure of the communication pore and analyzing the relative values of burst pressure at the communication pore and advancing pressure at the chamber-connecting channel we have been able to not only prevent gel bursting, but also precisely control the gel interface at a pre-defined position aligned with the microfluidic channel wall. Figure 2.2a showed the fibrin gel raised to the vertexes of communication pores with a flat gel–air interface without bursting into the microfluidic channels, which could not be achieved with the previous design (Fig. 2.2S) [21-23]. After establishing interstitial flow across the tissue chamber, ECFC-ECs formed vascular fragments as early as day 2, and continued to develop into a capillary network through day 5. By day 7, the capillary network was lumenized and interconnected (Figure 2.2b). Figure 2.2c showed the CD 31 immunostaining image of the developed capillary network inside tissue chamber. Importantly, the laminin coating inside the microfluidic channels promoted migration of EC out from the tissue chamber through the communication pore and onto the surface of the channels, thereby facilitating interconnection of the capillary network with the outer channels (Figure 2.2d). This is in line with reports that laminin is also a potent chemoattractant for EC migration besides being a major component of basement membrane [28]. To verify perfusion of the developed capillary network, 15 μm diameter fluorescent microparticles were introduced into the high pressure outer channel and these then flowed through the microvascular network from one communication pore to the other and out into the low pressure outer channel, as shown in Figure 2.2e and a movie clip (http://www.rsc.org/suppdata/c5/lc/c5lc01050k/c5lc01050k2.mp4).

EC lining along the microfluidic channels

Since the microfluidic channels were coated with laminin and subsequently lined with an EC monolayer, its cross sectional area decreased from 100 μm × 100 μm to approximately 90 μm × 90 μm. The average fluid velocity was ~4300 μm s^{-1}, calculated from CFD analysis and the dynamic viscosity of the cell culture medium EGM-2 was 1×10^{-3} Pa s. Therefore, the calculated average wall shear stress was 3.82 dyn/cm^2, which was close to the average shear stress of 4 dyn/cm^2 in normal microvasculature [29].

After 24 hours under laminar shear stress, the ECs lining the outer channel proliferated and formed a monolayer. By 48 hours after lining, the EC monolayer became confluent, and ECs adopted an elongated morphology and aligned with the direction of laminar flow established inside the channel (Figure 2.3A). In contrast, when ECs migrated out from the tissue chamber during vasculogenesis (in the absence of EC added directly to the outer channel), ECs only coated a small portion of the channel, near the communication pore (Figure 2.3D). EC lining resulted in the entire inner surface of the microfluidic channels being covered with ECs, which then represent the artery (high pressure) and vein (low pressure) of our 3D microvascular model (Figure 2.3B and C). The lined EC monolayer remained intact along the channel surface for more than 7 days after lining without any collapse or regression.

Sprouting angiogenesis and anastomosis

Since the independent capillary network and artery/vein were formed by vasculogenesis and EC lining respectively, it was necessary to interconnect them together to form the intact microvascular network. After the EC lining process, a confluent EC monolayer formed on the gel interface at the communication pore, as shown in Figure 2.4A. By applying a basal-to-apical transendothelial flow as

well as generating a positive VEGF gradient, the lined ECs at the cell–matrix interface invaded into the 3D fibrin gel and formed microvascular sprouts as early as 24 hours post-lining (Figure 2.4B). After 48 hours, highly branched and abundant sprouts further extended into the gel, which provided a precondition for anastomosis with the capillary network inside the tissue chamber (Figure 2.4C).

Anastomosis was achieved by two processes with our methodology (Figure 2.4D). From inside the tissue chamber, mCherry-expressing (red) ECs (ECs-mCherry) migrated outward to the laminin-coated microfluidic channel to connect with the lined BFP-labeled ECs (ECs-BFP) in the channels. From the outer microfluidic channels, the lined ECs-BFP invaded into the 3D gel and formed sprouts (Figure 2.4C) to connect with the capillaries in the tissue chamber. These bidirectional processes produced a tight connection at the communication pore between EC lining along the microfluidic channels and the capillary network inside the tissue chamber.

Multi-step microvascular network development

By integrating vasculogenesis and EC lining strategies, an intact and perfusable microvascular network of artery/vein and capillaries could be developed in this microfluidic device *via* a multi-step process. Figure 2.5 showed development of the microvascular network through 12 days. Vasculogenesis of ECs-mCherry started to occur 3 days after introducing cell-seeded fibrin gels into the tissue chamber. ECs-BFP were added to an outer channel at this point. After 24 hours post-lining, these lined ECs-BFP began to elongate and form connections with ECs-mCherry through the communication pore. On day 5, the other channel was lined with EC-BFP and the direction of interstitial flow, which was also the transendothelial flow direction, was reversed to promote remodeling of the capillaries inside the tissue chamber and to stimulate angiogenic sprouting of lined ECs. In addition, ECs-mCherry also migrated out from the tissue chamber and interlaced with ECs-

BFP lining the microfluidic channel. ECs-BFP along both microfluidic channels continued to proliferate, elongate, and form connections with the microvascular network inside the tissue chamber thereafter. By day 12, a fully lumenized capillary network inside the tissue chamber had anastomosed with both EC-lined microfluidic channels to form the intact microvascular network.

Perfusion in the absence of non-physiological leakage

To verify whether non-physiological leakage was present in the developed anastomotic microvascular network, 70 kDa FITC-dextran was introduced into the vessels, as shown in Figure 2.6A and movie clip (http://www.rsc.org/suppdata/c5/lc/c5lc01050k/c5lc01050k1.mp4). After loading dextran from left to right in an EC-lined microfluidic channel for 4 minutes (the lower channel in the figure), it quickly flowed into the capillary network through the communication pore. Over time, the fluorescence intensity in the lumen of microvessels increased due to the intensive dextran influx. Finally, dextran passed through the capillaries and flowed into the low pressure side microfluidic channel and exited within 15 minutes, validating the connectivity and perfusability of the microvascular network. More importantly, no dextran was observed outside the vessel during the 15 minutes perfusion (and only minimal leakage at 45 minute), including the communication pore region where lined ECs connect to the microvascular network (Figure 2.6B). This demonstrated the strong barrier property of the microvascular network, and the tightness of the anastomosis.

The reason we chose 70 kDa dextran to test barrier function is that it has a molecular weight close to human serum albumin (MW ~ 66.5 kDa) which is the main protein of human plasma. In addition, 4 kDa dextran was also perfused into the developed 3D microvascular network (Figure 2.3S). As expected, its transportation rate across vascular wall into the interstitial space was faster than that of 70 kDa dextran due to the small molecular weight, which was the same as that *in vivo*.

Finally, quantitative assessment of the permeability coefficient at the interconnection region was performed on both the anastomotic and non-anastomotic microvascular network with 70 kDa dextran. The fluorescence image at 0 minute was considered as background, and the fluorescence images at 15 minute and 45 minute were utilized to calculate the initial average fluorescence intensity and final average intensity, respectively. The average vessel diameter around the communication pore was 50 μm, and the time interval between the initial time point and final point was 30 minutes. The permeability coefficient of 70 kDa FITC-dextran for a non-anastomotic microvascular network was measured to be 6.1×10^{-8} cm/s ($n = 2$), which was 2.18 fold higher than that of 2.8×10^{-8} cm/s ($n = 2$) for the anastomotic microvascular network. This result further confirmed the tight interconnection between artery/vein and capillary network with our bidirectional anastomosis process.

2.5 Discussion

This model is both biology-driven and engineering-inspired. The microvascular network formed inside tissue chamber is biology-driven *via* vasculogenesis, thus better recapitulating the capillary network *in vivo* compared to other pre-patterned network approaches utilized in previously published studies [30, 31]. At the outer microfluidic channels, our engineering approach to line EC and control shear stress allows better mimicking of artery/vein, and facilitates anastomosis of the microvascular network. Compared to previous 3D microvascular models, our model provides an intact and perfusable microvascular system with artery/vein and capillary network tightly interconnected without appreciable leakage. This model represents a major advance in tools available for vascular biology research. Traditional studies of biotransportation across the blood vessel wall have been done using Transwell assays, where EC are plated on one side of a Transwell membrane and perivascular cells are plated on the other side to mimic the blood vessel basement membrane. However, due to the Transwell membrane thickness, this method fails to capture the close interactions between EC and perivascular cells, as well as the basement membrane that they share *in vivo*. Thus, the blood barrier and transport properties are not fully recapitulated. With our model, intravascular physiological transport and EC-perivascular interactions can be better studied in real time with fluorescent imaging. In addition, other types of cells can be co-cultured inside the tissue chamber to produce a specific vascularized organ-on-a-chip (*e.g.*, heart, liver, tumor, *etc.*). Since each functional organ unit with this design has its respective vascular interface, multiple organ-on-chips can be interconnected artery-to-artery and vein-to-vein *via* the EC-lined microfluidic channels, forming a basic 3D microvascular model to study organ-to-organ interactions. This model can also be applied to drug screening by eliciting the reaction of different organs to the same drugs or other chemical substances. However, there are certain limitations in our approach. While lining EC inside the

microfluidic channels promotes anastomosis and limits leakage, the production process is more complex, requiring multiple additional steps. Consequently, this method cannot easily be scaled-up for high-throughput screening applications. In addition, while the EC-lined microfluidic channels mimic the inner layer of larger vessels, the lack of smooth muscle cell coverage at the outer layer limits vasoconstriction, an important mechanism in vascular regulation. We also note that the average diameter of the microvessels in the device (50 μm) is larger than that of the typical capillaries (10–20 μm) *in vivo*. Control of microvessel diameter is a complex process, dependent upon flow rate, shear, pressure, presence of pericytes/smooth muscle cells, and stiffness of the matrix. This is an interesting phenomenon that we will be further exploring.

2.6 Conclusion

In this paper, we developed an advanced 3D microvascular model by integrating vasculogenesis and EC lining strategies on one novel microfluidic device. This model is based on a robust multi-step process enabled by engineering the microfluidic device to include a microenvironment conducive for physiological vascular network development. The microvascular networks we can form in this device have excellent vascular barrier properties, and show minimal leakage. A major advantage of this model is the ability to create intact and perfusable microvascular networks including "arteries", "veins" and capillaries that can undergo remodeling. This device can be customized for the development of specific vascularized micro-organs inside on-chip tissue chambers by co-culturing with other cell types. The vascular interfaces developed here could interconnect multiple organ units towards the vision of a human "body-on-a-chip".

2.7 References

1. Lee H, C.M., Jeon NL, *Microvasculature: An essential component for organ-on-chip systems.* MRS Bulletin. Cambridge University Press, 2014. **39**(1): p. 51-59.
2. Schimek, K., et al., *Integrating biological vasculature into a multi-organ-chip microsystem.* Lab Chip, 2013. **13**(18): p. 3588-98.
3. Hasan, A., et al., *Microfluidic techniques for development of 3D vascularized tissue.* Biomaterials, 2014. **35**(26): p. 7308-25.
4. Esch, M.B., et al., *Characterization of in vitro endothelial linings grown within microfluidic channels.* Tissue Eng Part A, 2011. **17**(23-24): p. 2965-71.
5. Booth, R., S. Noh, and H. Kim, *A multiple-channel, multiple-assay platform for characterization of full-range shear stress effects on vascular endothelial cells.* Lab Chip, 2014. **14**(11): p. 1880-90.
6. Bischel, L.L., et al., *Tubeless microfluidic angiogenesis assay with three-dimensional endothelial-lined microvessels.* Biomaterials, 2013. **34**(5): p. 1471-7.
7. Lee, H., et al., *A bioengineered array of 3D microvessels for vascular permeability assay.* Microvasc Res, 2014. **91**: p. 90-8.
8. Kim, S., et al., *Engineering of functional, perfusable 3D microvascular networks on a chip.* Lab Chip, 2013. **13**(8): p. 1489-500.
9. Yeon, J.H., et al., *In vitro formation and characterization of a perfusable three-dimensional tubular capillary network in microfluidic devices.* Lab Chip, 2012. **12**(16): p. 2815-22.
10. Vickerman, V. and R.D. Kamm, *Mechanism of a flow-gated angiogenesis switch: early signaling events at cell-matrix and cell-cell junctions.* Integr Biol (Camb), 2012. **4**(8): p. 863-74.
11. Young, E.W., *Advances in microfluidic cell culture systems for studying angiogenesis.* J Lab Autom, 2013. **18**(6): p. 427-36.
12. Chiu, L.L., et al., *Perfusable branching microvessel bed for vascularization of engineered tissues.* Proc Natl Acad Sci U S A, 2012. **109**(50): p. E3414-23.
13. Whisler, J.A., M.B. Chen, and R.D. Kamm, *Control of perfusable microvascular network morphology using a multiculture microfluidic system.* Tissue Eng Part C Methods, 2014. **20**(7): p. 543-52.
14. Diaz-Santana, A., M. Shan, and A.D. Stroock, *Endothelial cell dynamics during anastomosis in vitro.* Integr Biol (Camb), 2015. **7**(4): p. 454-66.
15. Chan, C.Y., et al., *Accelerating drug discovery via organs-on-chips.* Lab Chip, 2013. **13**(24): p. 4697-710.
16. Huh, D., et al., *Microengineered physiological biomimicry: organs-on-chips.* Lab Chip, 2012. **12**(12): p. 2156-64.
17. Bhatia, S.N. and D.E. Ingber, *Microfluidic organs-on-chips.* Nat Biotechnol, 2014. **32**(8): p. 760-72.
18. Huang, C.P., et al., *Engineering microscale cellular niches for three-dimensional multicellular co-cultures.* Lab Chip, 2009. **9**(12): p. 1740-8.
19. Cho, H., et al., *How the capillary burst microvalve works.* J Colloid Interface Sci, 2007. **306**(2): p. 379-85.

20. Chen, X., et al., *Rapid anastomosis of endothelial progenitor cell-derived vessels with host vasculature is promoted by a high density of cotransplanted fibroblasts.* Tissue Eng Part A, 2010. **16**(2): p. 585-94.
21. Moya, M.L., et al., *In vitro perfused human capillary networks.* Tissue Eng Part C Methods, 2013. **19**(9): p. 730-7.
22. Hsu, Y.H., et al., *A microfluidic platform for generating large-scale nearly identical human microphysiological vascularized tissue arrays.* Lab Chip, 2013. **13**(15): p. 2990-8.
23. Hsu, Y.H., et al., *Full range physiological mass transport control in 3D tissue cultures.* Lab Chip, 2013. **13**(1): p. 81-9.
24. Vickerman, V., et al., *Design, fabrication and implementation of a novel multi-parameter control microfluidic platform for three-dimensional cell culture and real-time imaging.* Lab Chip, 2008. **8**(9): p. 1468-77.
25. Song, J.W. and L.L. Munn, *Fluid forces control endothelial sprouting.* Proc Natl Acad Sci U S A, 2011. **108**(37): p. 15342-7.
26. Song, J.W., D. Bazou, and L.L. Munn, *Anastomosis of endothelial sprouts forms new vessels in a tissue analogue of angiogenesis.* Integr Biol (Camb), 2012. **4**(8): p. 857-62.
27. Jeon, J.S., et al., *Generation of 3D functional microvascular networks with human mesenchymal stem cells in microfluidic systems.* Integr Biol (Camb), 2014. **6**(5): p. 555-63.
28. Simon-Assmann, P., et al., *Role of laminins in physiological and pathological angiogenesis.* Int J Dev Biol, 2011. **55**(4-5): p. 455-65.
29. Buchanan, C.F., et al., *Three-dimensional microfluidic collagen hydrogels for investigating flow-mediated tumor-endothelial signaling and vascular organization.* Tissue Eng Part C Methods, 2014. **20**(1): p. 64-75.
30. Miller, J.S., et al., *Rapid casting of patterned vascular networks for perfusable engineered three-dimensional tissues.* Nat Mater, 2012. **11**(9): p. 768-74.
31. Zheng, Y., et al., *In vitro microvessels for the study of angiogenesis and thrombosis.* Proc Natl Acad Sci U S A, 2012. **109**(24): p. 9342-7.

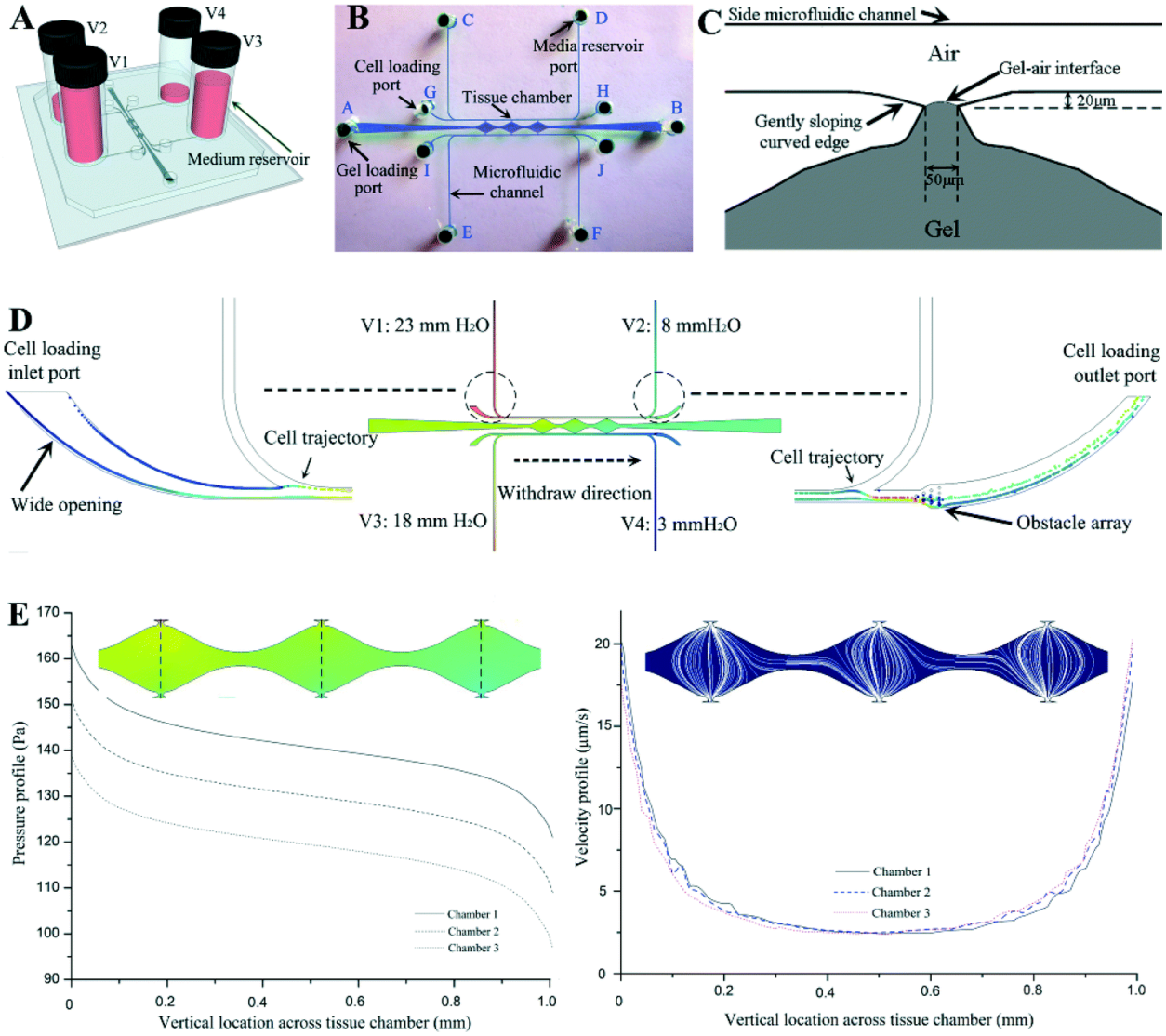

Figure 2.1: Microfluidic device design. (A) Schematic of decoupling design with four media reservoirs containing different medium volume. (B) Top-view of channel structure and ports for gel loading, cell loading and media reservoir. (C) Schematic of the optimized hourglass shaped communication pore design that can precisely stop advancing gel at its vertexes with relatively flat gel–air interface, and enable the formation of a smooth EC monolayer on the gel interface. (D) Simulation result on pressure distribution inside the entire device, and the particle tracing from cell loading inlet port with wide opening to cell loading outlet port with obstacle array through withdrawal mode. (E) Simulation results on pressure drop and velocity profile of interstitial flow across three tissue chambers.

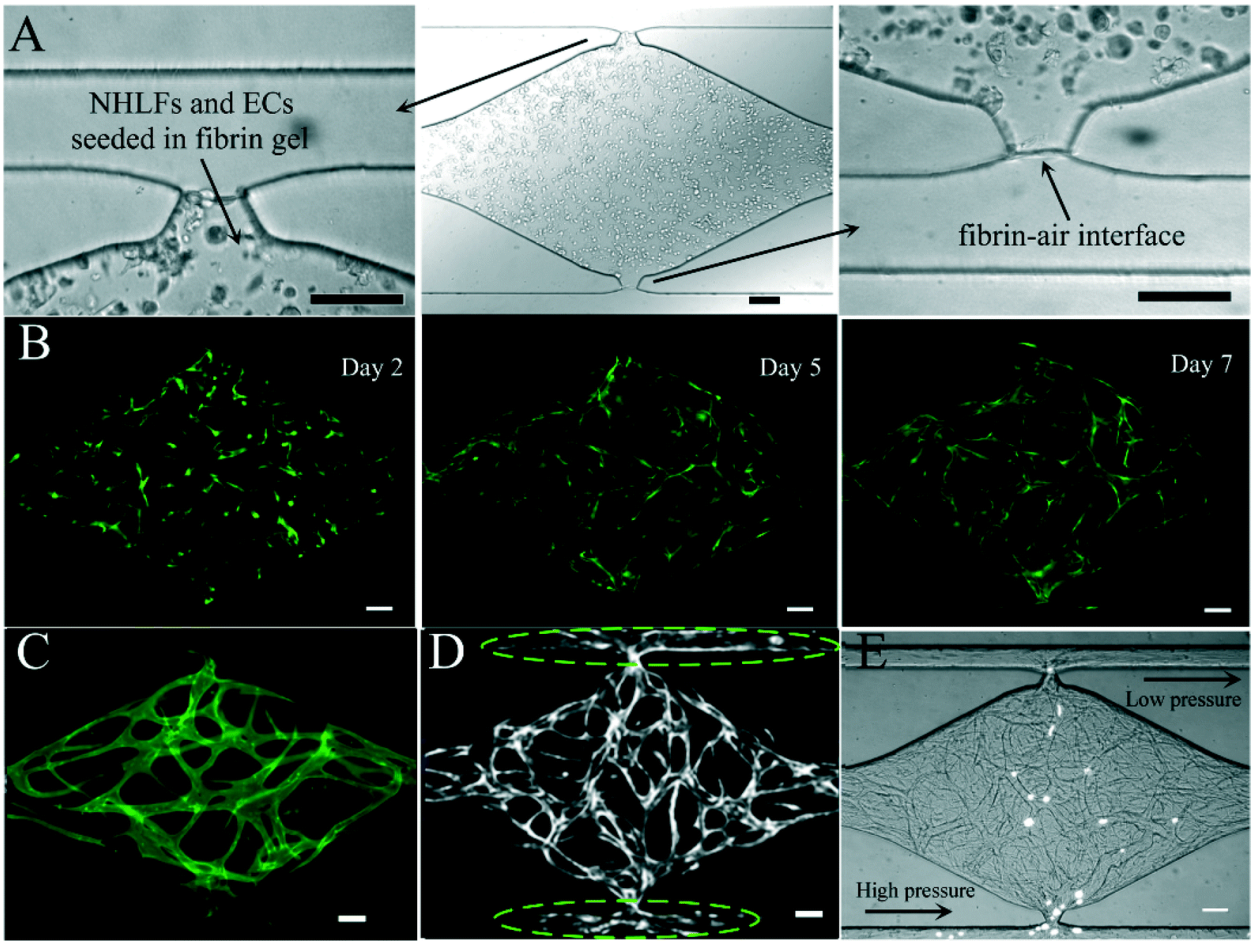

Figure 2.2: Experimental results on cell-seeded gel loading and vasculogenesis inside the tissue chamber. (A) Cell-seeded gel loading was arrested at a pre-defined location closed to the side microfluidic channel resulting in a flat gel–air interface without bursting. (B) Progression of vasculogenesis over time. (C) CD31 immunostaining image of a capillary network inside a tissue chamber. (D) ECs migrate out from tissue chamber and move along the microfluidic channel adjacent to the communication pore, as indicated by dashed ellipse. (E) Perfusion of 15 μm fluorescent microparticles inside vessel lumens. Scale bars: 100 μm.

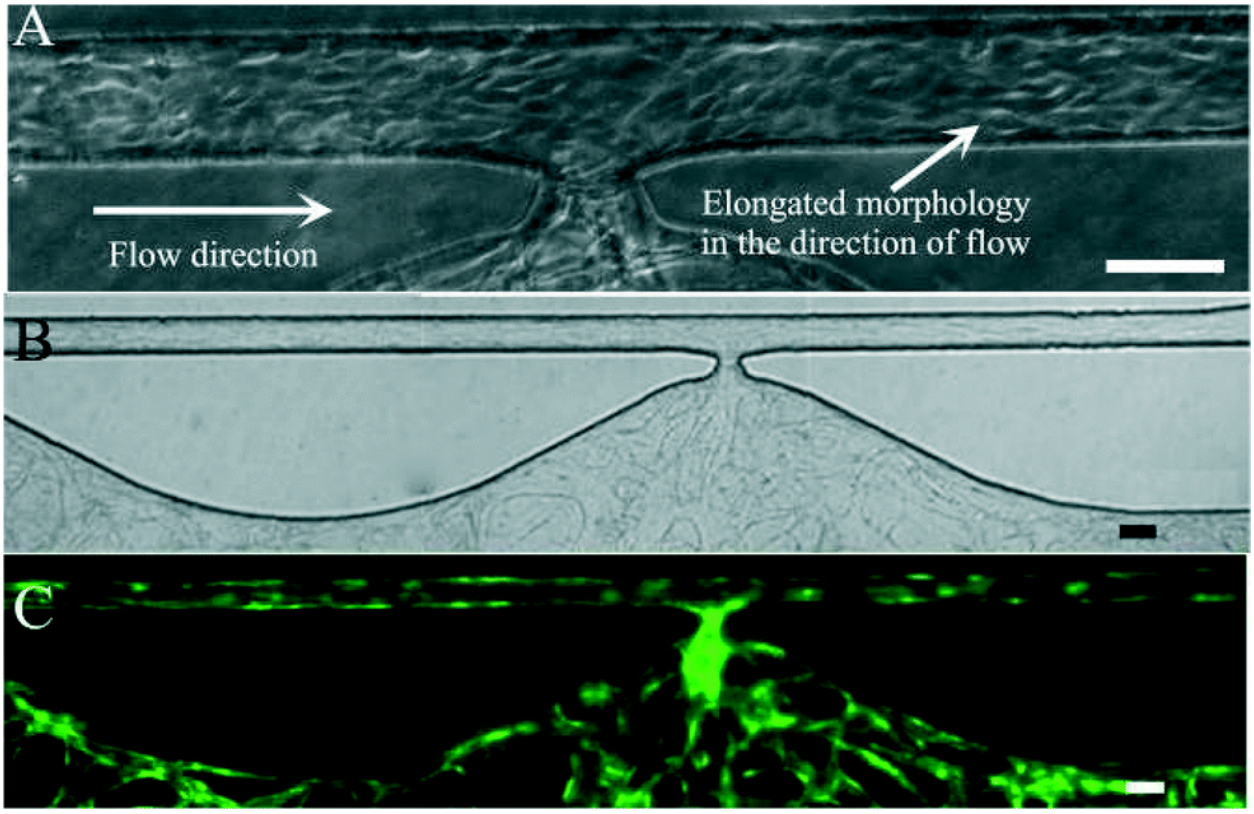

Figure 2.3: EC lining along microfluidic channel. (A) ECs with elongated morphology in the direction of fluidic flow. (B) Bright field image of EC lining along entire microfluidic channel after vasculogenesis. (C) Corresponding fluorescent image. Scale bars: 100 μm.

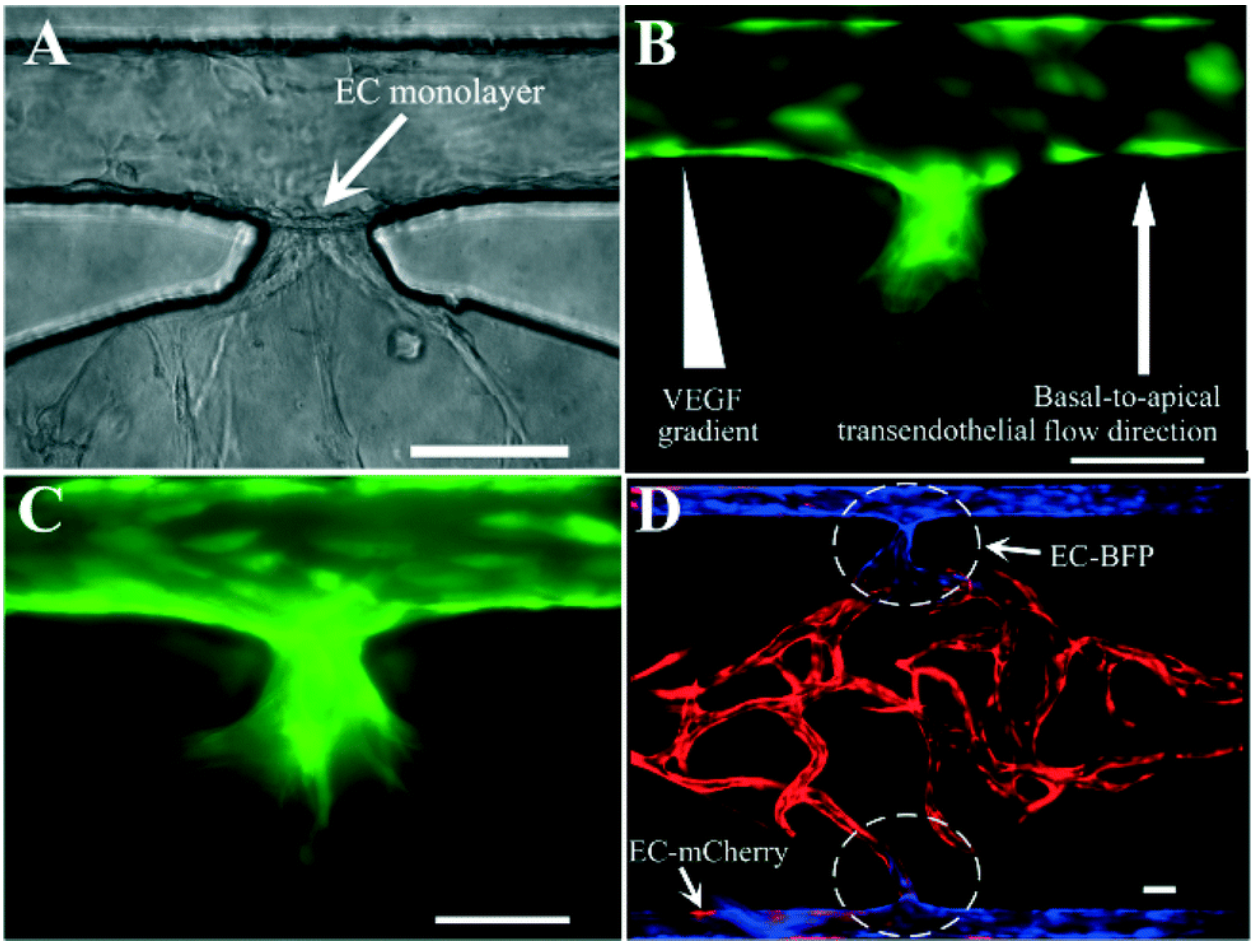

Figure 2.4: Sprouting angiogenesis and anastomosis. (A) Formation of an EC monolayer on the gel interface at the communication pore after EC lining. (B) Invasion of microvascular sprouts from the lined EC monolayer into the gel after 24 hours. (C) More sprouts and deep invasion after 48 hours post-lining. (D) Tight interconnection between EC lining along the outer channel and the capillary network inside tissue chamber by anastomosis with bidirectional migration. Scale bars: 100 μm.

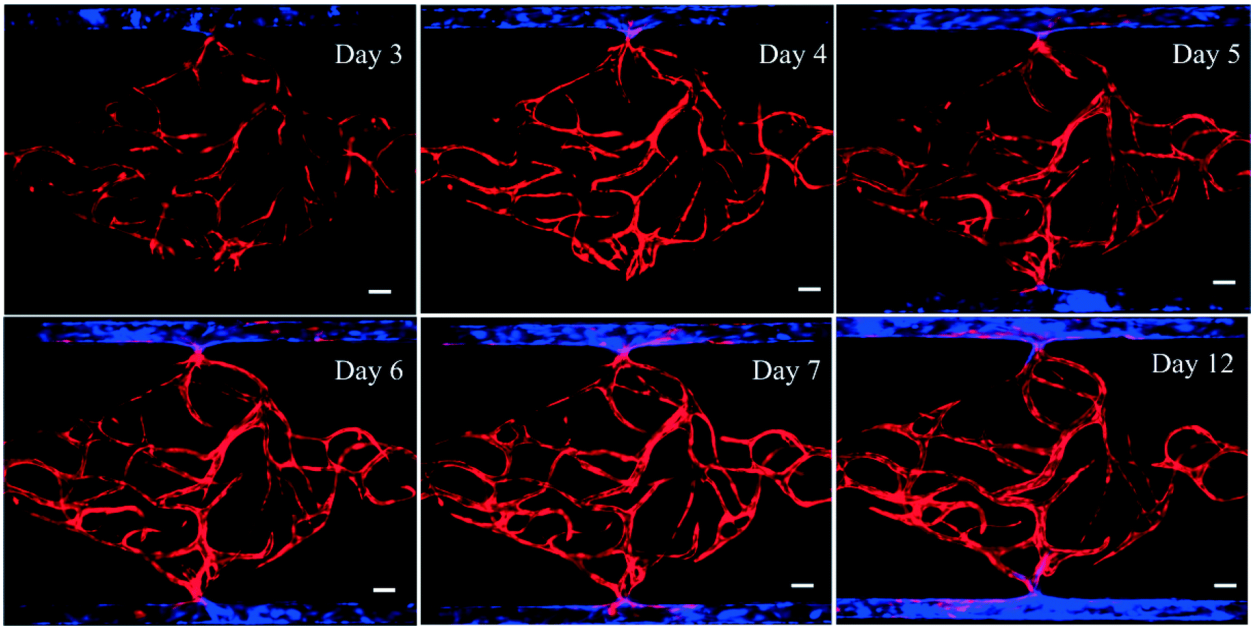

Figure 2.5: Formation of intact and perfusable microvascular network with artery/vein and capillary network by multi-step processes throughout 12 days. Scale bars: 100 μm.

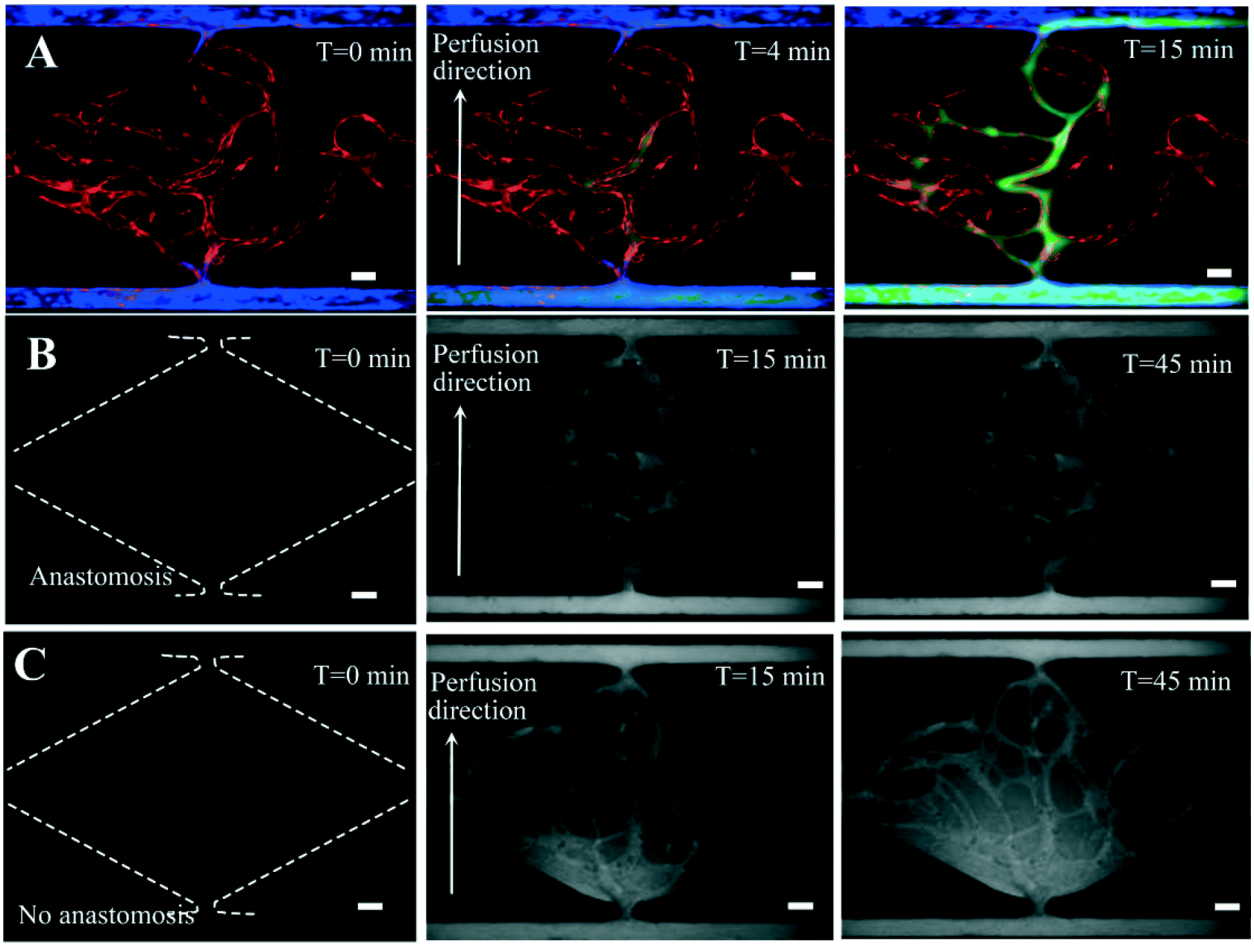

Figure 2.6: 70 kDa dextran perfusion test and permeability coefficient measurement. (A) Fluorescence images showing dextran perfusion in the absence of non-physiological leakage. (B) Time lapse images of intensity change in anastomotic microvascular network for permeability coefficient measurement. (C) Time lapse images of intensity change in non-anastomotic microvascular network as a control. Scale bars: 100 μm.

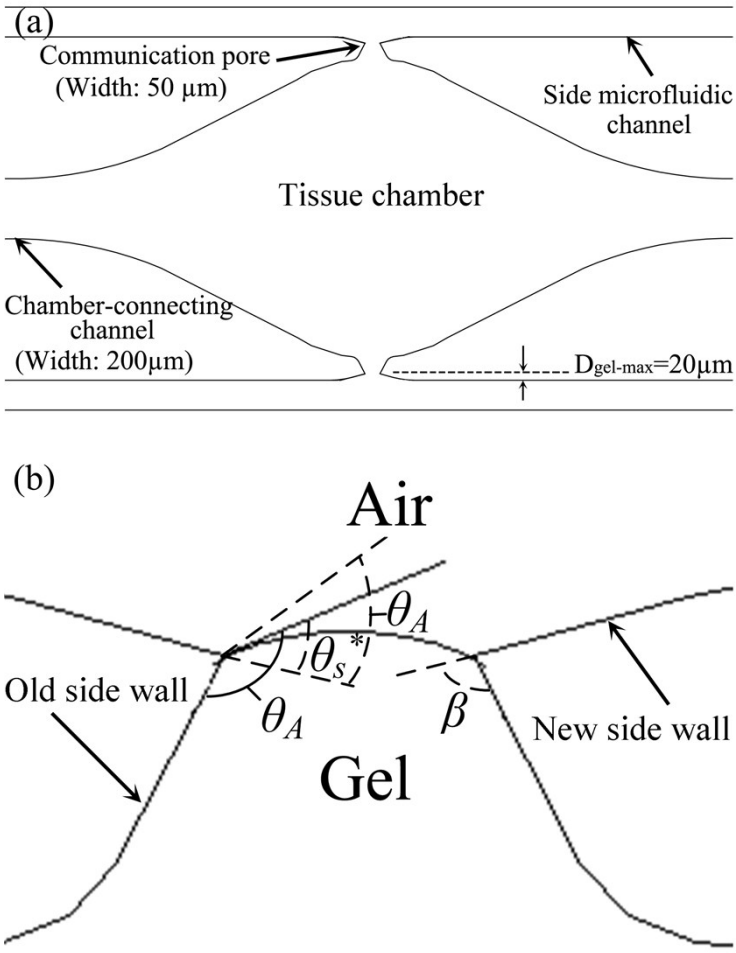

Figure 2.1S: (a) Schematic and dimensions of one tissue chamber with optimized communication pore design. (b) Different contact angle of gel interface with side walls of designed communication pore and the quantitative analysis of Laplace pressure at the gel-air interface during the loading process.

The pressure difference exerted on the gel-air interface during loading process can be analyzed by Young-Laplace equation expressed as:

$$P_{gel} - P_{air} = -2\gamma(\cos\theta_s / w + \cos\theta_v / h)$$

where P_{gel} is the gel pressure inside loading channel, γ is surface tension, w and h are width and height of microfluidic channel where the interface is located, θ_s is the contact angle formed between gel interface and side walls, and θ_v is the contact angle of gel interface with the top wall and bottom wall.

When the contact angles with all walls exceed the critical advancing contact angle θ_A (i.e. θ_S

$\geq\theta_A$ and $\theta_V \geq\theta_A$), the interface will burst to induce gel movement. Therefore, the pressure difference for gel bursting interface can be given by:

$$P_{gel-burst} - P_{air} = -2\gamma(\cos\theta_A / w + \cos\theta_A / h)$$

Therefore, for chamber-connecting channel of our design with 200 μm in width and 100 μm in height, its advancing pressure is 1655 Pa by assuming γ = 0.072 N m^{-1}, θ_A=140°.

As shown in Fig. S1b, the expanded new side wall with gentle slope is utilized as the capillary burst valve in our design, which can trap the gel as closely as possible to the microfluidic channel. When the meniscus meets the new side wall, its contact angle reduces

from θ_A to $\theta_S^*=\theta_A - \beta$, where β is the angle between old side wall and new side wall, thus the gel stops instantly. The gel interface will bulge with the gradually build-up pressure, until its contact angle with new side wall reach up to θ_A, which also means the contact angle with old side wall reaches up to $\theta_A^*=\theta_A + \beta$. It is noted that maximum contact angle for liquid meniscus cannot exceed 180°, thus the critical bursting contact angle with old side wall for capillary burst valve should be β_A^*=min $\{\theta_A + \beta, 180^o\}$ Therefore, the burst pressure for capillary burst valve $P_{valve\text{-}burst}$ can be expressed as:

$$P_{valve-burst} - P_{air} = -2\gamma(\cos\theta_A^* / w + \cos\theta_A / h)$$

Therefore, for communication pore of our design with 50 μm in width and 100 μm in height, its burst pressure is 3983 Pa by assuming γ = 0.072 N m^{-1}, θ_A=140° and θ_A^*=180°.

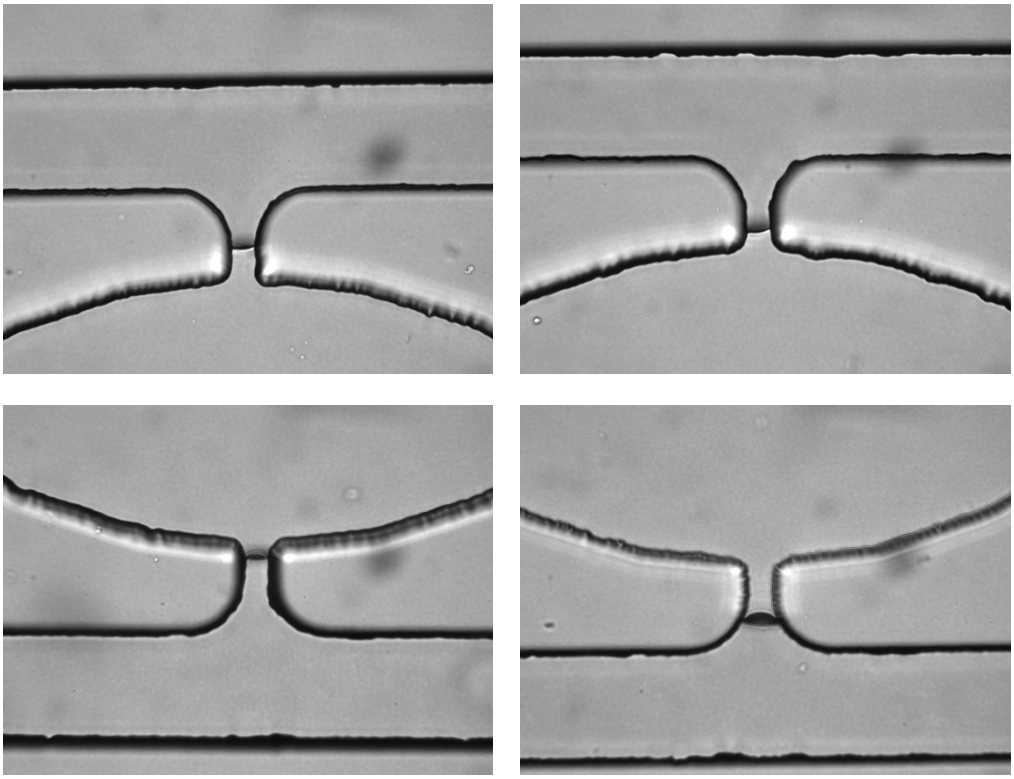

Figure 2.2S: Gel loading with previous communication pore design. Although it can prevent gel bursting to certain extents, it is difficult to pin the gel at specific location.

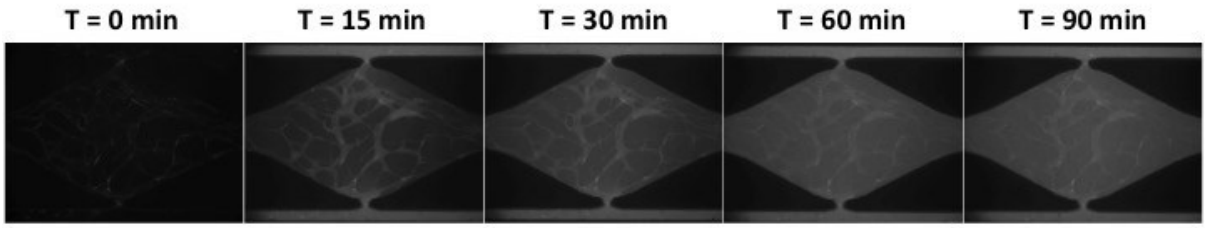

Figure 2.3S: Experimental result on 4 kDa dextran perfusion into the 3D microvascular network, and its transportation rate across vascular wall into the interstitial space was faster than that of 70 kDa dextran due to the small molecular weight.

CHAPTER 3

3D microtumors *in vitro* supported by perfused vascular networks

Agua Sobrino, * Duc T.T. Phan, * Rupsa Datta, Xiaolin Wang, Stephanie J. Hachey, Monica Romero-Lopez, Enrico Gratton, Abraham P. Lee, Steven C. George, and Christopher C.W. Hughes

(* Contributed equally as first authors)

Originally published in Scientific Reports 2016, 6:31589.

3.1 Abstract

There is a growing interest in developing microphysiological systems that can be used to model both normal and pathological human organs *in vitro*. This "organs-on-chips" approach aims to capture key structural and physiological characteristics of the target tissue. Here we describe *in vitro* vascularized microtumors (VMTs). This "tumor-on-a-chip" platform incorporates human tumor and stromal cells that grow in a 3D extracellular matrix and that depend for survival on nutrient delivery through living, perfused microvessels. Both colorectal and breast cancer cells grow vigorously in the platform and respond to standard-of-care therapies, showing reduced growth and/or regression. Vascular-targeting agents with different mechanisms of action can also be distinguished, and we find that drugs targeting only VEGFRs (Apatinib and Vandetanib) are not effective, whereas drugs that target VEGFRs, PDGFR and Tie2 (Linifanib and Cabozantinib) do regress the vasculature. Tumors in the VMT show strong metabolic heterogeneity when imaged using NADH Fluorescent Lifetime Imaging Microscopy and, compared to their surrounding stroma, many show a higher free/bound NADH ratio consistent with their known preference for aerobic glycolysis. The VMT platform provides a unique model for studying vascularized solid tumors *in vitro*.

3.2 Introduction

Despite some recent successes cancer remains one of the leading causes of morbidity and mortality worldwide. New drugs come to market slowly, their development is enormously expensive, and many provide only modest improvements in quality or extension of life [1]. Part of the problem is that we lack good *in vitro* models, and so our understanding of tumor behavior in a complex 3D environment is limited and drug screens are often misleading.

Although tumors are complex three-dimensional (3D) structures with their own unique microenvironments, many studies ignore this complexity in the interest of simplicity and convenience. Studies are often performed using cell lines growing as two-dimensional (2D) monolayers in plastic dishes, and the role of matrix, stromal cells, and vasculature is ignored. 2D monocultures do not accurately mimic the complex interplay between tumor cells and their extracellular environment, and a growing body of evidence has emerged demonstrating differences in the phenotype of tumor cells when cultured in 3D [2 – 4]. For example, proliferation rates may differ, metabolic profiles may be altered, and dose-response curves for some drugs can differ by orders of magnitude [5, 6]. This may result from targets not being expressed in 2D, from survival pathways being activated in 3D, or from contributions by stromal cells. Compounding these deficiencies is the fact that tumors receive nutrients and therapeutics through the vasculature, and this component of the tumor microenvironment has never been previously included in *in vitro* tumor models.

The growing use of tumor spheroids addresses some of these shortcomings – the cells are in a 3D environment and stromal cells may be present [7]. However, there is no vasculature and many tumor cell types, especially those with a highly invasive phenotype, do not readily form

spheroids, and so cannot be assayed in these systems. Patient-derived xenograft (PDX) models maintain the tumor microenvironment[8], but are time-consuming, expensive, and limited by the supply of tissue.

To address the concerns with current tumor models we have developed a microphysiological system that incorporates human cells in a 3D extracellular matrix (ECM), supported by perfused human microvessels [9 – 12]. The vessels are enveloped by perivascular cells, have physiologic flow, and deliver nutrients to the tissue. We refer to this "base" tissue as a vascularized micro-organ (VMO). The microfabricated platform is transparent, allowing for non-invasive optical imaging of the tissues. We have now incorporated tumor cells into the VMO platform to create vascularized microtumors (VMTs). Growth of the VMTs can be tracked through fluorescent protein expression, and fluorescence lifetime imaging microscopy (FLIM) can monitor their metabolic status [13]. We find that both the tumors and the vasculature are sensitive to standard-of-care chemotherapeutics, that the tumors show considerable metabolic heterogeneity, that their metabolic state differs significantly from the stroma, and that this can be altered by chemotherapeutic drugs. The VMT platform is thus an ideal model for studying tumor-vasculature interactions, tumor metabolism, and response of tumor cells and vasculature to anti-cancer drugs.

3.3 Materials and Methods

Design of the microfluidic platform

The device consists of 2 straight microfluidic channels separated by 3 diamond-shaped tissue chambers (1 × 2 × 0.1–0.12 mm). The channels are connected to 2 media inlets and outlets on each side. On top of each inlet and outlet, a large medium reservoir is attached to establish hydrostatic pressure (10 mm H_2O) across the microfluidic channel and a 5-mm H_2O interstitial pressure across the tissue chambers. The channels are connected on either side of the tissue chamber via a communication pore 50 μm wide. The pore is designed with a unique curved opening that mimics the capillary burst valve to prevent the fibrin gel from bursting into the microfluidic channels when seeding the device, while also bringing the gel boundary close to the straight microfluidic channels to facilitate anastomosis of the vascular network inside the issue chambers.

Microfabrication of the PDMS microfluidic device

The microfluidic device is created using standard PDMS soft lithography. To develop the mold, a 100 μm layer of SU-8 is spin-coated onto Si-wafer (RCA-1 cleaned and 2% HF treated), following by a single mask photolithography step to pattern the tissue chamber, communication pores, and fluidic channels. The microfabricated SU-8 mold is silanized with trichlorosilane ($C_8H_4Cl_3F_{13}Si$) in a vacuum chamber. To fabricate the microfluidic device, an 8 mm-thick layer of PDMS (Dow Corning) is molded onto the SU-8 mold, degassed in a vacuum chamber, and allowed to solidify at 70 °C overnight. The PDMS microfluidic device is de-molded, hole-punched, and bonded to a 1 mm-thick membrane of PDMS attached to a microscope coverslip slide (Corning). Medium reservoirs are attached to the bonded device using PDMS and allowed

to solidify at 70 °C overnight. The device is subsequently sterilized by autoclaving at 120 °C before use.

Cell culture

Human endothelial colony forming cell-derived ECs (ECFC-ECs) are isolated from cord blood and expanded on gelatin-coated flasks in EGM-2 (Lonza). The methods were carried out in accordance with the approved guidelines and with approval from UC Irvine's Institutional Review Board. ECFC-ECs are transduced with lentivirus to express fluorescent proteins (mCherry, or GFP) and used between passages 4–7. Normal human lung fibroblasts (NHLFs) are purchased from Lonza, cultured in DMEM (Corning) containing 10% Fetal Bovine Serum (FBS, Gemini Bio Products). While the cells in different lots all express NG2 and CD90 there are considerable differences between lots. We select lots for further studies based on higher NG2 and CD90 expression as these perform better as perivascular cells. We use them between passages 5–8. Colorectal cancer cell lines (SW620, SW480, and HCT116), breast cancer cell lines (MDA-MB-231, and MCF-7), and a melanoma cell line (MNT-1) were obtained from UC Irvine's Chao Family Comprehensive Cancer Center and transduced with lentivirus to express fluorescent proteins (mCherry, GFP, or Azurite Blue). All cancer cell lines are cultured in 10% FBS DMEM. All cell types are grown in a 37 °C, 5% CO_2 and 20% O_2 incubator in 100% humidified air. Lentiviral constructs to express mCherry and GFP (LeGO-C2, LeGO-V2) were gifts from Boris Fehse (Addgene plasmids # 27339 and 27340), and lentiviral construct to express Azurite Blue was a gift from Pantelis Tsoulfas (Addgene plasmid # 36086).

Seeding the devices

Fibrinogen solution is prepared by dissolving 70% clottable bovine fibrinogen (Sigma-Aldrich) in 1× Dulbecco's Phosphate Buffered Saline with Ca^{2+}/Mg^{2+} (LifeTechnologies) to a final concentration of 10 mg/mL. NHLFs and ECFC-ECs are harvested and resuspended in fibrinogen solution, each at a concentration of 5×10^6 cells/mL. To create a tumor microtissue, cancer cells are then harvested and resuspended in the mixture at a concentration of 200,000 cells/mL. The final cell-matrix suspension is mixed with thrombin (50 U/mL, Sigma-Aldrich) for a final concentration of 3 U/mL, quickly seeded into the microtissue chambers, and allowed to polymerize in a 37 °C incubator for 15 minutes. Laminin (1 mg/mL, LifeTechnologies) is then loaded into the microfluidic channels through medium inlets and incubated at 37 °C for an additional 15 minutes to stimulate ECFC-EC anastomosis with the microfluidic channels. After incubation, culture medium (EGM-2, Lonza) is introduced into the microfluidic channels and subsequently medium reservoirs to establish a 5-mm H_2O interstitial pressure across the tissue chambers. Medium in reservoirs is changed and leveled every other day to maintain interstitial flow. Anastomosis of the vascular network is confirmed by introducing 70 kDa FITC or Rhodamine B-dextran (LifeTechnologies) to the medium reservoir on day 7 post-embedding, and visualization using fluorescent microscopy.

Drug exposure in the device

To assess drug screening experiments, cells in the microfluidic device were exposed to reported *in vivo*plasma concentrations of different FDA approved anti-cancer drugs or a standard dose of 100 nM. 5-Fluoruracil (5-FU), Vincristine, Sorafenib and Taxol were obtained from the NIH-MPS Training Compound Collection at Evotec. Oxaliplatin, Pazopanib, Linifanib, Apatinib

and CP-673451 were purchased from Selleck Chemicals. Vemurafenib, Vandetanib, Cabozantinib and Sorafenib were obtained from National Cancer Institute (NCI) plate sets. All compounds were dissolved in dimethyl sulfoxide (DMSO) and added in the medium with less than 0.01% DMSO. For hormone response in breast cancer cell lines, Estradiol (Sigma-Aldrich) was used at physiological plasma concentration. Estradiol was dissolved in 100% ethanol and added in the medium with less than 0.001% Ethanol. For a typical screening assay, after 5–8 days of cells cultured in the microdevice, media from the device is replaced by media containing the drug at the desired concentration, and delivered through the microfluidic channels using the hydrostatic pressure gradient.

Time-lapse image sequences and time course image analysis

For tumor and vessel quantification within the microfluidic device, and time-lapse image sequences, time course images were taken using a SPOT Pursuit High Speed Cooled CCD camera (SPOT Imaging). For tumor quantitative analysis, fluorescent intensity of mCherry, GFP, or Azurite Blue was analyzed using ImageJ software (National Institute of Health). Vessel fluorescent intensity of mCherry was used for vessel quantitative analysis. Total vessel length and total number of branch points was performed using AngioTool (National Cancer Institute). Vessel diameter were determined using the MATLAB subroutine, RAVE, developed by Seaman *et al*. [55]. Final values were normalized to time zero of drug exposure. Three replicates (microtissue chambers) were examined per experiment. Confocal imaging of fluorescence reporters was performed on a Zeiss LSM 710 microscope (Carl Zeiss, Jena, Germany) using a 20x air objective, 0.5 N.A. (EC Plan-Neofluor, Carl Zeiss, Oberkochen, Germany). GFP was excited with 488 nm and signal collected between 493–581 nm. mCherry was excited with 561 nm and emission collected between 578–696 nm. mRFP was excited with 561 and emission

collected between 582–754 nm. Azurite Blue was excited at 405 nm and emission collected between 410–585 nm. Image acquisition and post processing was done using Zen software (Zeiss, Germany). Where adjustments were made to images these were performed on the entire image, and all images in that experimental group were adjusted to the same settings. To reduce confusion, some images have been re-colored to maintain consistent color-coding throughout the paper. Thus vessels are shown as red and tumor cells as green, although in some cases EC were expressing GFP and the tumor cells were expressing mCherry (or mRFP). We have seen no differences in cell behavior when they express GFP vs mCherry or mRFP.

Vascular permeability quantification

For vascular permeability quantification, medium is replaced by DPBS with similar hydrostatic pressure profile, and the device is positioned onto a microscope stage. 70 kDa-FITC or 150 kDa FITC-dextran (Sigma-Aldrich) is introduced to the reservoir with highest hydrostatic pressure to a final concentration of 50 μg/mL, and allowed to perfuse through the microfluidic channel. An image of background fluorescent intensity is acquired prior to addition of the dye. After allowing FITC-dextran to fully perfuse the microvascular network (15 minutes), time-lapse images are acquired every 15 minutes for a time course of 90 minutes. The diffusive component of the solute permeability coefficient P is calculated using the equation previously described [56] by quantifying the background average fluorescence intensity (I_b), the initial average fluorescence intensity (I_i) step change after FITC-dextran influx reached equilibrium at the initial time point, and the final average fluorescence intensity (I_f) of 12 central regions of tissue chamber. Three independent experiments for 70 kDa and 150 kDa permeability coefficient quantification are obtained for statistical analysis.

Collagen I image acquisition

Second harmonic generation (SHG) signal was acquired using the microscopic system developed by the Laboratory of Fluorescent Dynamics (LFD) at UCI [57]. A Ti:Sapphire laser (Mai Tai, Spectra Physics, Irvine, CA) was used for two-photon fluorescence excitation, with a wavelength of 740 nm and an incident power in the sample of 20 mW. The signal was collected using a long working distance water objective (LUMPlanFl 40x/0.80 W, Olympus, Tokyo, Japan). The SHG signal was obtained using a 320 nm- 390 nm bandpass filter. Images were taken every 5 μm through the sample with a depth of view of 740 μm. Data acquisition was performed in SimFCS (software developed by the LFD). The images were analyzed with the free ctFIRE MATLAB version (http://loci.wisc.edu/software/ctfire), extracting the information corresponding to fiber length of 3 replicates for every time point.

Immunofluorescent staining

For immunofluorescent staining, devices were fixed by flowing 4% paraformaldehyde (Sigma-Aldrich) for 2 h at room temperature, followed by an overnight PBS wash at 4 °C. Blocking, washing, antibody incubation, and nuclei staining steps are also conducted by flowing reagents through the microfluidic channels overnight at 4 °C. Collagen IV was observed by staining using rabbit anti-human Collagen IV polyclonal antibody (AbD-Serotec 2150-0150, Bio-Rad) followed by Alexa 408 Donkey anti-rabbit secondary antibody. Confocal imaging of stained collagen IV was performed on Zeiss LSM 710 microscope (Carl Zeiss, Jena, Germany) using a 20x air objective, 0.5 N.A. (EC Plan-Neofluar, Carl Zeiss, Oberkochen, Germany), excited with 405 nm and emission signal was collected between 410–585 nm. The vascular network was observed by staining with PE/Cy7 anti-human CD31 antibody (BioLegend).

Perivascular cells were visualized using antibodies to NG2 (Millipore EMD/MAB5384) and PDGFR-β (Cell Signaling/3169) at 1:200 dilution. Secondary antibody was Alexa Fluor 488 (ThermoFisher), used at 1:300.

Fluorescence lifetime image acquisition and analysis

Fluorescence lifetime imaging microscopy (FLIM) of reduced nicotinamide adenosine dinucleotide (NADH) was performed on a Zeiss LSM 710 microscope (Carl Zeiss, Jena, Germany) using a 20x air objective, 0.5 N.A. (EC Plan-Neofluar, Carl Zeiss, Oberkochen, Germany) with two photon excitation of 740 nm (titanium:sapphire MaiTai laser from Spectra-Physics, Mountain View, CA). Image scan speed was 25.21 μs/pixel and image size is 256 × 256 pixels. For NADH FLIM of the whole chambers, a 2 by 2 tile scan was performed. 460/80 nm bandpass filter was employed as emission filter and a photomultiplier tube (H7422P-40, Hamamatsu, Japan) was used for detection. FLIM data was acquired using A320 FastFLIM FLIMbox (ISS, Champaign, IL). For acquisition and FLIM data analysis SimFCS software, developed at the Laboratory for Fluorescence Dynamics (LFD, UC Irvine), was used. For analysis of FLIM data, the phasor approach was used. In this method, lifetime information from every pixel of the image is transformed into a phasor on the phasor plot to create the FLIM phasor distribution, as described previously [58]. By NADH FLIM phasor analysis, we can map the free to protein bound NADH distribution in the images which can be correlated to the metabolic status of the biological sample [13, 33].

Cell viability assay

2D screening experiments in tumor cells were assessed using the colorimetric XTT-cell viability assay according to the manufacturer's protocol (Sigma). Briefly, HCT116 were seeded

into 96-well plates in 100 μL at plating densities of 5,000. Tumor cell density was selected according to the doubling time of the cell line to determine tumor cell proliferation. After cells were seeded, the plates were incubated at 37 °C, 5% CO_2, 95% air and 100% relative humidity for 24 h prior to addition of drugs. For optimal comparison between 2D and 3D, the drug screening schedule in 2D was selected to match the one used in the microfluidic device. XTT absorbance values at 450 nm (corrected at 690 nm) were measured using a microplate spectrophotometer. Three replicates for each exposure concentration were examined. Results were expressed as percent cell viability for each concentration with respect to DMSO controls.

Statistical analysis

Data represent mean ± s.d unless otherwise stated. The differences between experimental groups of equal variance were analyzed using Student's t test. Estimated means, standard deviation, and significance levels were calculated using GraphPad software. Number of replicates is indicated in the legends. The level of significance was set at $p < 0.05$.

3.4 Results

Establishment of Vascularized Micro-Organs

The VMO platform allows for the reproducible creation of perfused vascular networks *in vitro*. These networks support physiologic flow and can deliver nutrients to surrounding tissues sufficient to support robust growth. The platform is constructed using standard photolithography from polydimethyl siloxane (PDMS) [12] and consists of two outer microfluidic channels that act as arteriole (high pressure) and venule (low pressure), connected by three tissue chambers, into which is injected a slurry of ECM and cells (Figure 3.1a). Over the course of 5–7 days EC self-assemble into an interconnected network that anastomoses with the outer channels. EC migrate into the outer channels, forming a tight seal, and over time, line the surface of the channel. At this point flow through the device switches from interstitial to intraluminal. Flow is generated by a hydrostatic head (Figure 3.1a). We routinely transduce EC with mCherry for easy visualization of the network (Figure 3.1b). Vessel-like fragments appear within 2–3 days and a complete network is apparent by 5–7 days (Figure 3.1c and Figure 3.1S.a). Perfusion of the vascular network with 70 kDa FITC-dextran reveals the vessels to be minimally leaky (Figure 3.1d, https://media.nature.com/original/nature-assets/srep/2016/160823/srep31589/extref/srep31589-s2.mov). We calculate the degree of leakage by measuring the increase of fluorescence signal in the extracellular compartment over time and this gives a permeability of 4.5×10^{-7} cm/s for 70 kDa-dextran, and 1.2×10^{-7} cm/s for 150 kDa-dextran (Figure 3.1S.b) which are in line with values obtained for capillaries *in vivo [14]*.

Stromal cells are required for proper formation of the vascular networks [15, 16], and a subset of these consistently envelop the newly-formed vessels, forming tight appositions (Figure 3.1e). These cells are both $NG2^{+}$ and PDGFR-β^{+} (Figure 3.1f), consistent with a pericyte

phenotype [17, 18]. Once established, the vessels rapidly lay down a collagen IV-rich basement membrane (Figure 3.1g) The stromal cells also express multiple other extracellular matrix proteins, including Collagen I (Figure 3.1S.c), that are required for lumen formation [16, 19].

Establishment of Vascularized Micro-Tumors (VMTs) and response to drugs

We next incorporated tumor cells into the platform to create VMTs. The human colorectal cancer (CRC) cell line HCT116 was transduced to express GFP and introduced to the tissue chambers along with the EC, matrix and stromal cells. By day 6, when the microvasculature had formed, the tumor cells had proliferated to form small spheroids (Figure 3.2a). Perivascular cells wrapped around a subset of the microvessels (Figure 3.2S) and vessels were found within and around the tumor spheroids (https://media.nature.com/original/nature-assets/srep/2016/160823/srep31589/extref/srep31589-s3.mov). Tumor spheroids were often found in close apposition to microvessels (Figure 3.2S), consistent with tumor behavior *in vivo* [20]. Perfusion of the tumor-associated vascular network was confirmed using fluorescently-tagged dextran (Figure 3.3S). In addition to HCT116 we tested two other CRC lines (SW620 and SW480), two breast cancer lines (MCF-7 and MDA-MB-231), and a melanoma cell line (MNT-1) (Figure 3.2b and e). In each case a vascular network formed that supported growth of the tumors. Interestingly, the tumors showed reproducibly different patterns of growth – SW480 and MCF-7 grew as tight colonies, whereas MDA-MB-231 and MNT-1 showed considerably more diffuse, invasive growth patterns (Figure 3.2b). We also saw significant differences in growth rate, vascular development and collagen synthesis in each VMT model (Figure 3.4S), suggesting that each tumor cell line may be uniquely remodeling its microenvironment.

To test whether CRC VMTs respond to standard anticancer therapies we screened several FDA-approved drugs and drug combinations, including FOLFOX (5-FU, Leucovorin and Oxaliplatin), the standard-of-care chemotherapy for CRC. By 48 h FOLFOX had significantly reduced tumor growth compared to control (Figure 3.2c and d), and by 96 h the tumors had regressed to below their starting volume. Importantly, even after drug removal the suppressive effect continued, confirming the cytotoxic rather than cytostatic effect of FOLFOX treatment. Also of note is the observation that the vascular network is largely unaffected, a finding we address in greater detail below.

We also tested as single agents several drugs with differing modes of action: 5-FU is a cytotoxic, cell-cycle–specific agent; Oxaliplatin is a cytotoxic platinum analog, and cell-cycle–nonspecific agent that induces DNA damage; Vincristine is a cell-cycle-specific M-phase agent; and, Sorafenib, is a small MW multikinase inhibitor that targets the vascular endothelial growth factor receptor (VEGFR) family, and platelet-derived growth factor receptor-β (PDGFR-β). It also inhibits the serine/threonine kinase Raf, which makes it useful in targeting tumors, such as HCT116, that carry the oncogenic KRAS mutation. To model a clinical regimen, drugs were added at concentrations that mirror patient plasma trough levels, and were removed after 48 h. VMTs were then cultured for an additional 2 days. All four drugs significantly reduced tumor growth, and when compared to data from 2D cultures, dose response curves showed a significant right shift (higher IC50 values), indicating drug resistance in the VMTs (Figure 3.2e and 3.5S.a and b). It is unlikely that partition of drugs into PDMS is an issue in our device as there is a constant and relatively high convective flow through the microfluidic channels. The Peclet number represents the ratio of mass transport by convection to diffusion and in our device is equal to ~6.5×10^3 for a small molecular weight drug such as Sorafenib. Thus, although there

may be some adsorption to the PDMS as the medium flows through the outer channels, this will not significantly reduce the concentration of the drug that reaches the tumor cells. In addition, protein adsorption and EC lining of the channels further limits loss of drug to the PDMS [21, 22].

There is considerable diversity in responses to drugs between tumors from different organs, and even within tumors from the same organ [20]. Responsiveness depends on mutational burden, gene expression patterns, and on the local microenvironment. In light of this we also tested two additional CRC lines as well as two breast cancer lines. The two CRC lines SW480 and SW620 are derived from the same patient, but from the primary site and from a lymph node metastasis, respectively. The lines have a largely overlapping mutation profile that differs from HCT116. We noted clear differences in response to a panel of drugs, with SW620 being significantly more drug resistant than HCT116 (Figure 3.5S.c and d). Cells carrying p53 mutations are known to be relatively resistant to the apoptosis-inducing drug 5-FU, and we see this reproduced in the VMTs where SW620 (p53 mutant) are significantly more resistant to 5-FU than HCT116, which are wild-type for p53 (Figure 3.5S.c and d).

We next examined the response of the triple-negative breast cancer line MDA-MB-231 to the standard-of-care chemotherapeutic Taxol – a mitotic disrupter. When left untreated for 96 h, the tumor cells grew rapidly and were highly invasive (Figure 3.2f and g and compare to HCT116 in panel 3.2c). In contrast, cells treated with Taxol showed greatly reduced migration and growth. As expected, tumor vasculature was also disrupted in response to Taxol, in addition to its direct effects on tumor cells (Figure 3.2f and g) MCF-7 cells (Estrogen Receptor (ER) alpha (α)+; Progesterone Receptor (PR)+) were similarly responsive to Taxol (Figure 3.2h) We also examined the response of both cell lines to additional currently-used chemotherapeutic

drugs as well as their response to physiological concentrations of 10 nM Estradiol (E2), which is important in breast cancer hormone-therapy. We found that whereas both cell lines are sensitive to Oxaliplatin, 5-FU and Taxol, they respond differently to E2 (Figure 3.2h). As expected, MCF-7 cells, which are ERα+, showed an increase in tumor proliferation in response to E2, whereas the growth of MDA-MB-231 (ERα− and ERβ+) was moderately inhibited by the presence of the hormone (Figure 3.2h). This result is in agreement with the proposed use of E2-agonists for the treatment of triple negative breast cancer [23]. A third tumor type – melanoma (MNT-1 (Figure 3.2b) and A375 cells (not shown)) – also grows well in the VMT platform, reinforcing the utility of this system for the study of multiple tumor cell lines.

Vasculature as a drug target

A key feature of tumor progression is the angiogenic switch [20]. The formation of new blood vessels in and around the tumor can be driven by a number of tumor-derived factors, a key family being the VEGFs. Targeting these growth factors and their receptors has proven moderately successful in the treatment of several human cancers, including cervical [24], glioblastoma [25], and metastatic CRC [26], especially in combination with more established anti-cancer agents. We therefore examined the effect of several anti-angiogenic drugs on stability of the vascular network. Importantly, we use Endothelial Colony-Forming Cell (ECFC)-derived EC in the VMT as these have been suggested to be a good model for tumor EC [27]. Pazopanib is one of a new generation of tyrosine kinase inhibitors, with potent activity against VEGFRs, and to a lesser extent, PDGFR. Addition of Pazopanib resulted in a dose-dependent decrease in total vessel length, total number of junctions and lumen diameter after 72 h of drug exposure (Figure 3.3a and b). The multikinase inhibitor Sorafenib is a widely-used antiangiogenic agent, whereas the mitosis inhibitor Vincristine is known to behave as a vascular disrupting agent in the

tumor microenvironment [28, 29] Exposure of vessels to these reagents clearly distinguishes their modes of action: in both cases we see a significant decrease in total vessel length and total number of branch points after 96 h of drug exposure (Figure 3.3c to e). However, regression of newly-forming (angiogenic) vessels is observed only with Sorafenib, while complete disruption of the network is observed after treatment with Vincristine (Figure 3.3c and d). We next compared 10 clinically-approved receptor tyrosine kinase (RTK) inhibitors known to target VEGFR2, PDGFR, Tie2 and/or FGFR1 among others, using a standard dose of 100 nM (Figure 3.3f). Compounds such as Apatinib and Vandetanib that target only VEGFR2 were not effective in disrupting the vascular networks, whereas compounds that inhibit both VEGFR2 and PDGFR, such as Axitinib and Pazopanib, were more effective. In line with this, combined use of PDGFR inhibitors and Apatinib increased the effectiveness of the VEGFR2 inhibitor. Finally, we identify Linifanib and Cabozantinib as being most effective in this assay, quite possibly due to their activity against Tie2, in addition to their inhibition of VEGFR2 and PDGFR. We also found that the effect of Linifanib persisted longer after removal than for other drugs tested (Figure 3.6S), in line with its success in intermittent dosing regimes in preclinical studies [30].

Many drugs, including both Sorafenib and Vincristine, are thought to have dual effects in the tumor microenvironment, targeting both the tumor and the blood vessels that support it (see above). We looked for these dual effects in the VMT platform. We found that FOLFOX treatment reduces tumor growth by 70% while inhibiting vascular growth at most by 30% (Figure 3.7S). In contrast to FOLFOX, the antiangiogenic drug Pazopanib was more effective targeting vessels, while Oxaliplatin and 5-FU, not surprisingly, were more effective against tumor (Figure 3.8S and Figure 3.3g and h). These results translate to IC50 ratios (tumor growth: total vessel length) of 10.7, 7.1, 0.3, and 0.15 for Pazopanib, Vincristine, Oxaliplatin, and 5-FU,

respectively (Figure 3.3h). For Sorafenib, which targets angiogenesis through the VEGFRs and PDGFR-β, and tumor growth and proliferation directly through Raf kinase, the ratio was closer to 1 (Figure 3.8S and 3.3h). The VMT platform can, therefore, distinguish between the multiple modes of action of currently-used RTK inhibitors.

Tumor metabolism and metabolic response to drugs

Cellular metabolism is a potentially powerful biomarker for cellular state and response to drugs [31, 32]. NADH is the major electron acceptor in glycolysis and electron donor in oxidative phosphorylation, and the rate of glycolysis in cells has been found to correlate strongly with the ratio of free to bound NADH [33]. This ratio can be determined by examining the rate of fluorescence decay of NADH, which is extended when NADH is protein-bound [34]. Fluorescence Lifetime Imaging Microscopy (FLIM) is a label-free imaging modality that when coupled with the phasor approach to data analysis can report on free/bound NADH ratios at single pixel resolution [13, 33]. We first used FLIM to examine the metabolic profile of the vasculature in VMOs (Figure 3.9S.a), and confirmed that potassium cyanide (KCN), a known blocker of the respiratory mitochondrial transport chain, induced a shift from bound to free NADH (Figure 3.9S.b and c), in line with inhibition of OxPhos [35]. Interestingly, when we looked at high resolution (Figure 3.4a) we found a higher relative level of free NADH in the EC (blue/white – see phasor plot in 4a (iii) for mapping) compared to either the perivascular cells investing the vessels or the interstitial stromal cells. This result suggests that EC are more glycolytic than stromal cells, which is consistent with published reports [36, 37]. We also examined the metabolic profile of the vasculature in the presence or absence of flow, which limits nutrient delivery but not oxygen delivery (which diffuses freely through the PDMS). Under no-flow conditions the EC showed a decrease in free NADH (Figure 3.10S), suggestive of

a shift away from a higher glycolytic rate (high glucose consumption/low ATP yield) to perhaps an increase in oxidative phosphorylation (lower glucose consumption/higher ATP yield), although the latter has not been confirmed.

As described above, cellular metabolism is a potentially powerful tumor biomarker and target. Cancer cells often rely on glycolysis, uncoupled from OxPhos and independent of local O_2 concentrations, for energy production (known as aerobic glycolysis or the Warburg effect) [38]. We next asked whether the FLIM-phasor approach could be used in VMTs to interrogate tumor cell metabolism and the response of cells to chemotherapeutic challenge. As shown in Figure 3.4b we found much higher NADH free/bound ratios in MCF-7 breast cancer cells (blue/white) relative to other cells in the surrounding microenvironment (red), including vascular and stromal cells. This suggests that the tumor cells are more glycolytic than the surrounding cells, which is consistent with their known preference for aerobic glycolysis. There is a growing interest in tumor heterogeneity, and in particular in metabolic heterogeneity within tumors [33, 39]. High resolution FLIM imaging of just the tumor in (b) shows a clear pattern of high free NADH interspersed with areas of high bound NADH (Figure 3.4c), consistent with distinct domains of metabolic activity, and in line with what has been seem in colon tumors *in vivo* [33]. Additional FLIM images of MCF-7 cells are shown in Figure 3.11S where again, metabolic heterogeneity is clearly evident.

We next mapped the FLIM signatures of three additional tumor cell lines and compared these to the FLIM signature of their surrounding microenvironments (Figure 3.5a). Similar to MCF-7, both MDA-MB-231 and HCT116 had a significantly higher NADH free/bound ratio than their surrounding stroma, whereas SW620 were indistinguishable. We next treated MCF-7 cells with 5-FU and compared the NADH free/bound ratio to that in untreated cells (Figure

3.5b). Notably, we saw a strong decrease in the ratio of free/bound NADH in the treated cells, consistent with a slowed glycolytic rate. It should be noted that 5-FU induces apoptosis. which also leads to high levels of bound NADH (red) [40]. Importantly, the metabolic profile of the stroma remained unchanged in response to 5-FU (Figure 3.5b). Taken together, these data suggest a hierarchy of free/bound NADH (and potentially aerobic glycolytic rate) in the cells of the tumor microenvironment, from tumor (highest glycolytic rate/lowest OxPhos profile) to EC (moderate glycolytic rate) to stroma (lowest glycolytic rate/highest OxPhos profile), and furthermore suggest that inhibiting glycolysis may be an effective strategy to target tumor cells as well as their associated vasculature.

3.5 Discussion

We have developed a vascularized micro-organ (VMO) platform that can be configured for tumor studies. The vascularized microtumors (VMTs) capture some of the complexity of *in vivo* tumors, including 3D structure, extracellular matrix, the presence of stromal cells and the delivery of nutrients and drugs through a perfused vascular network. Importantly, the microvessels are not pre-patterned as they are in several recently published models [41, 42], which allows for remodeling in response to physiologic cues or pharmacologic therapy. Despite the relative complexity of the tissue, the platform is simple, requiring no external pumps, tubing, or robotics. Fluid flow is driven by gravity and the device can be readily configured to a 96-well plate format. The vessels are invested with cells expressing pericyte markers and their permeability characteristics match vessels *in vivo*.

The platform supports multiple tumor types, including invasive cells, such as MDA-MB-231, that do not readily form spheroids. We observed significant differences in IC50 doses for multiple drugs when 2D cultures were compared to the 3D VMT platform, which compares well with previous work using 3D cultures [2, 43, 44, 45]. We also suspect that the relative complexity of the microenvironment may contribute to these differences. It is important to note however, that the VMTs still lack some components of *in vivo*tumors, most notably, an immune component. While addition of macrophages to the VMT is trivial, incorporating an adaptive immune component will require sourcing of entirely autologous cells. These could be derived from the tumor, or generated from iPS cells. EC have previously been derived from iPS cells [46, 47] and so this goal may be within reach. Importantly, tumor cells with defined mutations retain their characteristic responses to chemotherapeutics in the VMT platform – SW620 cells, which carry a p53 mutation were considerably more resistant to 5-FU than HCT116, which express

wild-type p53 [48]. We have generated VMTs with six cancer cell lines so far, including three CRC lines, two breast cancer lines and a melanoma line, suggesting that the platform should be amenable to study of most cancer cell lines.

The development of new anticancer treatments includes identification of compounds that target cell signaling pathways involved in pathological EC proliferation, migration and morphogenesis [49, 50]. We have shown that the microvessels in the VMT platform are sensitive to the effects of both anti-angiogenic (Pazopanib, Linifanib, Cabozantinib, Axitinib, etc.) and vascular disrupting agents (Vincristine, Taxol), thus the platform can be used to identify reagents that target tumor cells directly, or indirectly through effects on the vasculature. Interestingly, the hierarchy of drug effectiveness we see (Figure 3.3f) matches well with data from zebrafish studies [51]. We have also noted enhanced angiogenic sprouting in the presence of tumor cells, as well as enhanced vascular leakage (unpublished observations).

A particularly exciting potential use for the VMT platform is in the study of metabolic changes in tumor and stroma in response to drug treatments. EC have previously been reported to show a preference for glycolytic activity [36] allowing oxygen to diffuse into deeper proliferating tissues, and the higher relative level of free NADH compared to the surrounding stroma in the VMT platform supports this finding. We find that multiple tumor cell types (e.g. MCF-7, MDA-MB-231, HCT116) are shifted even more in the direction of free NADH (aerobic glycolysis) relative to the stroma, suggesting that there is a hierarchy of glycolytic rate from stroma (lowest), through EC, up to tumor (highest). There is a growing awareness of the potential for reducing tumor drug resistance through metabolic targeting [52 – 54] and our data support the idea that reducing glycolysis may have some specificity for glycolysis-dependent tumors, and perhaps, their associated vasculature. In support of this we found that 5-FU, while

severely disrupting the NADH free/bound ratio in MCF-7 tumor cells had no effect on the stromal NADH free/bound ratio. Importantly, we also see strong metabolic heterogeneity in the tumors, consistent with previously reported *in vivo* studies [33]. There is a growing awareness that tumors may become drug-resistant, at least in part, through a metabolic switch to OxPhos (a reverse-Warburg effect), making the targeting of this a promising therapeutic approach. The VMT platform could prove ideal for identifying suitable drugs.

Future improvements to the VMT platform will include the incorporation of tumor-derived matrix and the use of plasma-containing medium that more fully reflects the composition of the fluid bathing tumor cells *in vivo*. Finally, the VMO platform is clearly suitable as a base for other organ systems, including for example, heart, liver, pancreas and the blood-brain barrier.

3.6 Acknowledgements

The authors thank Michaela Hatch and Kimberly Lim for help with cell culture. This work was supported by the following grants: UH3 TR000481 (SCG), R01 PQD5-CA180122 (CCWH) and R01 PQ24- CA170879 (SCG). CCWH receives support from the Chao Family Comprehensive Cancer Center (CFCCC) through an NCI Center Grant, P30A062203.

3.7 Contribution

C.C.W.H. and S.C.G. conceived the project, interpreted data and wrote the manuscript. A.P.L. contributed to platform design and edited the manuscript. A.S. and D.T.T.P. performed experiments, interpreted data and wrote the manuscript. X.W. and D.T.T.P. contributed to platform design, E.G. developed the SimFCS software for the analysis of the fluorescence images, R.D. performed experiments and analyzed the microscopy data. S.J.H. and M.R.-L. performed experiments and interpreted data. All authors read and approved the manuscript.

3.8 Conflict of interests

C.C.W.H., S.C.G. and A.P.L. are founders, and members of the scientific advisory board, of 4Design Biosciences, LLC and Kino Biosciences Inc.

3.9 References

1. Paul, S. M. *et al.* How to improve R&D productivity: the pharmaceutical industry's grand challenge. *Nat Rev Drug Discov* **9,** 203–214, doi: 10.1038/nrd3078 (2010).
2. Chitcholtan, K., Asselin, E., Parent, S., Sykes, P. H. & Evans, J. J. Differences in growth properties of endometrial cancer in three dimensional (3D) culture and 2D cell monolayer. *Exp Cell Res* **319,** 75–87, doi:10.1016/j.yexcr.2012.09.012 (2013).
3. Kenny, P. A. & Bissell, M. J. Tumor reversion: correction of malignant behavior by microenvironmental cues. *International journal of cancer. Journal international du cancer* **107,** 688–695, doi:10.1002/ijc.11491 (2003).
4. Yamada,K.M.&Cukierman,E.Modelingtissuemorphogenesisandcancerin3D.*Cell***130,**601–610,doi:10.1016/j.cell.2007.08.006(2007).
5. Santini, M. T. *et al.* MG-63 human osteosarcoma cells grown in monolayer and as three-dimensional tumor spheroids present a different metabolic profile: a (1)H NMR study. *FEBS Lett* **557,** 148–154 (2004).
6. Wrzesinski, K. *et al.* The cultural divide: exponential growth in classical 2D and metabolic equilibrium in 3D environments. *Plos One* **9,** e106973, doi:10.1371/journal.pone.0106973 (2014).
7. Levinger, I., Ventura, Y. & Vago, R. Life is three dimensional-as *in vitro* cancer cultures should be. *Adv Cancer Res* **121,** 383–414, doi:10.1016/B978-0-12-800249-0.00009-3 (2014).
8. Siolas, D. & Hannon, G. J. Patient-derived tumor xenografts: transforming clinical samples into mouse models. *Cancer Res* **73,** 5315–5319, doi:10.1158/0008-5472.CAN-13-1069 (2013).
9. Heylman, C., Sobrino, A., Shirure, V. S., Hughes, C. C. & George, S. C. A strategy for integrating essential three-dimensional microphysiological systems of human organs for realistic anticancer drug screening. *Experimental biology and medicine*, doi:10.1177/1535370214525295 (2014).
10. Hsu, Y. H. *et al.* Full range physiological mass transport control in 3D tissue cultures. *Lab on a chip* **13,** 81–89, doi:10.1039/c2lc40787f (2013).
11. Hsu, Y. H., Moya, M. L., Hughes, C. C., George, S. C. & Lee, A. P. A microfluidic platform for generating large-scale nearly identical human microphysiological vascularized tissue arrays. *Lab on a chip* **13,** 2990–2998, doi:10.1039/c3lc50424g (2013).
12. Moya, M. L., Hsu, Y. H., Lee, A. P., Hughes, C. C. & George, S. C. *In vitro* perfused human capillary networks. *Tissue engineering. Part C, Methods* **19,** 730–737, doi:10.1089/ten.TEC.2012.0430 (2013).
13. Stringari, C. *et al.* Phasor approach to fluorescence lifetime microscopy distinguishes different metabolic states of germ cells in a live tissue. *Proc Natl Acad Sci USA* **108,** 13582–13587, doi:10.1073/pnas.1108161108 (2011).
14. Yuan, W., Lv, Y., Zeng, M. & Fu, B. M. Non-invasive measurement of solute permeability in cerebral microvessels of the rat. *Microvasc Res* **77,** 166–173, doi:10.1016/j.mvr.2008.08.004 (2009).
15. Nakatsu, M. N. & Hughes, C. C. An optimized three-dimensional *in vitro* model for the analysis of angiogenesis. *Methods in enzymology* **443,** 65–82, doi:10.1016/S0076-6879(08)02004-1 (2008).

16. Newman, A. C., Nakatsu, M. N., Chou, W., Gershon, P. D. & Hughes, C. C. The requirement for fibroblasts in angiogenesis: fibroblast-derived matrix proteins are essential for endothelial cell lumen formation. *Mol Biol Cell* **22,** 3791–3800, doi:10.1091/mbc.E11-05-0393 (2011).
17. Berthod, F., Symes, J., Tremblay, N., Medin, J. A. & Auger, F. A. Spontaneous fibroblast-derived pericyte recruitment in a human tissue-engineered angiogenesis model *in vitro*. *J Cell Physiol* **227,** 2130–2137, doi:10.1002/jcp.22943 (2012).
18. Lin, S. L., Kisseleva, T., Brenner, D. A. & Duffield, J. S. Pericytes and perivascular fibroblasts are the primary source of collagen-producing cells in obstructive fibrosis of the kidney. *Am J Pathol* **173,** 1617–1627, doi:10.2353/ajpath.2008.080433 (2008).
19. Sacharidou, A. *et al.* Endothelial lumen signaling complexes control 3D matrix-specific tubulogenesis through interdependent Cdc42- and MT1-MMP-mediated events. *Blood* **115,** 5259–5269, doi:10.1182/blood-2009-11-252692 (2010).
20. Hanahan, D. & Weinberg, R. A. Hallmarks of cancer: the next generation. *Cell* **144,** 646–674, doi:10.1016/j.cell.2011.02.013 (2011).
21. Ostuni, E., Chen, C. S., Ingber, D. E. & Whitesides, G. M. Deposition of proteins and cells in arrays of microwells. *Langmuir* **17,** 2828–2834 (2001).
22. Toepke, M. W. & Beebe, D. J. PDMS absorption of small molecules and consequences in microfluidic applications. *Lab on a chip* **6,** 1484–1486, doi:10.1039/b612140c (2006).
23. Reese, J. M. *et al.* ERbeta1: characterization, prognosis, and evaluation of treatment strategies in ERalpha-positive and -negative breast cancer. *BMC Cancer* **14,** 749, doi:10.1186/1471-2407-14-749 (2014).
24. Tewari, K. S. *et al.* Improved survival with bevacizumab in advanced cervical cancer. *N Engl J Med* **370,** 734–743, doi:10.1056/NEJMoa1309748 (2014).
25. Arrillaga-Romany, I., Reardon, D. A. & Wen, P. Y. Current status of antiangiogenic therapies for glioblastomas. *Expert Opin Investig Drugs* **23,** 199–210, doi:10.1517/13543784.2014.856880 (2014).
26. Ferrarotto, R. & Hoff, P. M. Antiangiogenic drugs for colorectal cancer: exploring new possibilities. *Clin Colorectal Cancer* **12,** 1–7, doi:10.1016/j.clcc.2012.06.002 (2013).
27. Bagley, R. G. *et al.* Endothelial precursor cells as a model of tumor endothelium: characterization and comparison with mature endothelial cells. *Cancer Res* **63,** 5866–5873 (2003).
28. Awada, A. *et al.* Phase I safety and pharmacokinetics of BAY 43-9006 administered for 21 days on/7 days off in patients with advanced, refractory solid tumours. *Br J Cancer* **92,** 1855–1861, doi:10.1038/sj.bjc.6602584 (2005).
29. Baguley, B. C., Holdaway, K. M., Thomsen, L. L., Zhuang, L. & Zwi, L. J. Inhibition of growth of colon 38 adenocarcinoma by vinblastine and colchicine: evidence for a vascular mechanism. *Eur J Cancer* **27,** 482–487 (1991).
30. Albert, D. H. *et al.* Preclinical activity of ABT-869, a multitargeted receptor tyrosine kinase inhibitor. *Mol Cancer Ther* **5,** 995–1006, doi:10.1158/1535-7163.MCT-05-0410 (2006).
31. Heikal, A. A. Intracellular coenzymes as natural biomarkers for metabolic activities and mitochondrial anomalies. *Biomark Med* **4,** 241–263, doi:10.2217/bmm.10.1 (2010).
32. Zhao, Y., Butler, E. B. & Tan, M. Targeting cellular metabolism to improve cancer therapeutics. *Cell Death Dis* **4,** e532, doi:10.1038/cddis.2013.60 (2013).

33. Pate, K. T. *et al.* Wnt signaling directs a metabolic program of glycolysis and angiogenesis in colon cancer. *EMBO J* **33,** 1454–1473, doi:10.15252/embj.201488598 (2014).
34. Skala, M. C. *et al. In vivo* multiphoton fluorescence lifetime imaging of protein-bound and free nicotinamide adenine dinucleotide in normal and precancerous epithelia. *J Biomed Opt* **12,** 024014, doi:10.1117/1.2717503 (2007).
35. Bird, D. K. *et al.* Metabolic mapping of MCF10A human breast cells via multiphoton fluorescence lifetime imaging of the coenzyme NADH. *Cancer Res* **65,** 8766–8773, doi:10.1158/0008-5472.CAN-04-3922 (2005).
36. Harjes, U., Bensaad, K. & Harris, A. L. Endothelial cell metabolism and implications for cancer therapy. *Br J Cancer* **107,** 1207–1212, doi:10.1038/bjc.2012.398 (2012).
37. Peters, K. *et al.* Changes in human endothelial cell energy metabolic capacities during *in vitro* cultivation. The role of "aerobic glycolysis" and proliferation. *Cell Physiol Biochem* **24,** 483–492, doi:10.1159/000257490 (2009).
38. Warburg, O. On the origin of cancer cells. *Science* **123,** 309–314 (1956).
39. Sengupta, D. & Pratx, G. Imaging metabolic heterogeneity in cancer. *Mol Cancer* **15,** 4, doi:10.1186/s12943-015-0481-3 (2016).
40. Wang, H. W. *et al.* Differentiation of apoptosis from necrosis by dynamic changes of reduced nicotinamide adenine dinucleotide fluorescence lifetime in live cells. *J Biomed Opt* **13,** 054011, doi:10.1117/1.2975831 (2008).
41. Miller, J. S. *et al.* Rapid casting of patterned vascular networks for perfusable engineered three-dimensional tissues. *Nat Mater* **11,** 768–774, doi:10.1038/nmat3357 (2012).
42. Zheng, Y. *et al. In vitro* microvessels for the study of angiogenesis and thrombosis. *Proc Natl Acad Sci USA* **109,** 9342–9347, doi:10.1073/pnas.1201240109 (2012).
43. Aljitawi, O. S. *et al.* A novel three-dimensional stromal-based model for *in vitro* chemotherapy sensitivity testing of leukemia cells. *Leuk Lymphoma* **55,** 378–391, doi:10.3109/10428194.2013.793323 (2014).
44. Longati, P. *et al.* 3D pancreatic carcinoma spheroids induce a matrix-rich, chemoresistant phenotype offering a better model for drug testing. *BMC Cancer* **13,** 95, doi:10.1186/1471-2407-13-95 (2013).
45. Perche, F. & Torchilin, V. P. Cancer cell spheroids as a model to evaluate chemotherapy protocols. *Cancer Biol Ther* **13,** 1205–1213, doi:10.4161/cbt.21353 (2012).
46. Adams, W. J. *et al.* Functional vascular endothelium derived from human induced pluripotent stem cells. *Stem Cell Reports* **1,** 105–113, doi:10.1016/j.stemcr.2013.06.007 (2013).
47. Hewitt, K. J. *et al.* Epigenetic and phenotypic profile of fibroblasts derived from induced pluripotent stem cells. *Plos One* **6,** e17128, doi:10.1371/journal.pone.0017128 (2011).
48. Sui, X. *et al.* JNK confers 5-fluorouracil resistance in p53-deficient and mutant p53-expressing colon cancer cells by inducing survival autophagy. *Sci Rep* **4,** 4694, doi:10.1038/srep04694 (2014).
49. Ferrara, N. & Kerbel, R. S. Angiogenesis as a therapeutic target. *Nature* **438,** 967–974, doi:10.1038/nature04483 (2005).
50. Thorpe, P. E. Vascular targeting agents as cancer therapeutics. *Clin Cancer Res* **10,** 415–427 (2004).

51. Chimote, G. *et al.* Comparison of effects of anti-angiogenic agents in the zebrafish efficacy-toxicity model for translational anti-angiogenic drug discovery. *Drug Des Devel Ther* **8,** 1107–1123, doi:10.2147/DDDT.S55621 (2014).
52. Bost, F., Decoux-Poullot, A. G., Tanti, J. F. & Clavel, S. Energy disruptors: rising stars in anticancer therapy? *Oncogenesis* **5,** e188, doi:10.1038/oncsis.2015.46 (2016).
53. Ganapathy-Kanniappan, S. & Geschwind, J. F. Tumor glycolysis as a target for cancer therapy: progress and prospects. *Mol Cancer* **12,** 152, doi:10.1186/1476-4598-12-152 (2013).
54. Pavlova, N. N. & Thompson, C. B. The Emerging Hallmarks of Cancer Metabolism. *Cell metabolism* **23,** 27–47, doi:10.1016/j.cmet.2015.12.006 (2016).
55. Seaman, M. E., Peirce, S. M. & Kelly, K. Rapid analysis of vessel elements (RAVE): a tool for studying physiologic, pathologic and tumor angiogenesis. *PLoS One* **6,** e20807, doi:10.1371/journal.pone.0020807 (2011).
56. Jeon, J. S. *et al.* Generation of 3D functional microvascular networks with human mesenchymal stem cells in microfluidic systems. *Integrative biology: quantitative biosciences from nano to macro* **6,** 555–563, doi:10.1039/c3ib40267c (2014).
57. Crosignani, V., Jahid, S., Dvornikov, A. S. & Gratton, E. A deep tissue fluorescence imaging system with enhanced SHG detection capabilities. *Microsc Res Tech* **77,** 368–373, doi:10.1002/jemt.22354 (2014).
58. Digman, M. A., Caiolfa, V. R., Zamai, M. & Gratton, E. The phasor approach to fluorescence lifetime imaging analysis. *Biophys J* **94,** L14–16, doi:10.1529/biophysj.107.120154 (2008).

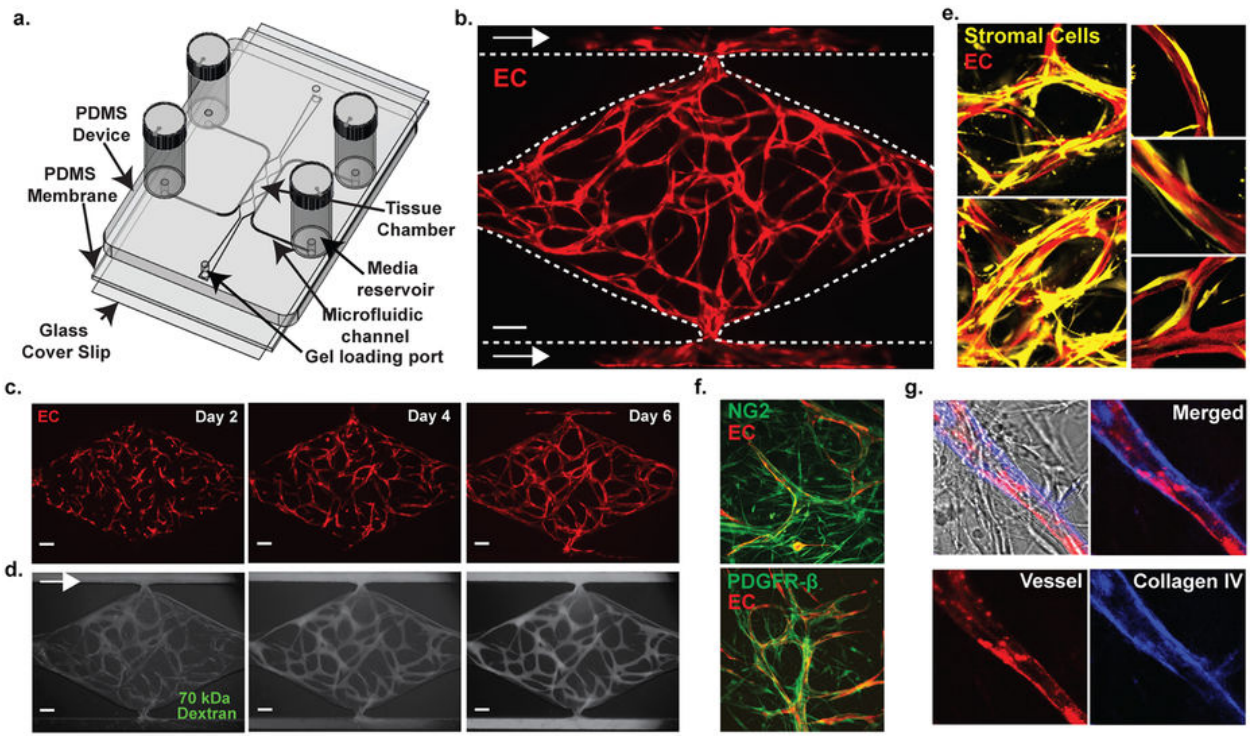

Figure 3.1: A vascularized micro-organ platform. (**a**) A schematic of the microfluidic platform. The VMO platform consists of a thick layer of PDMS containing patterned tissue chambers and microfluidic channels, bonded to a thin PDMS membrane and a glass cover slip. Three tissue chambers at the center are connected to two adjacent channels by two capillary burst valves that retain the mixture of cells and ECM inside the chambers. At the two ends of the tissue chambers are two gel loading ports, through which is introduced the cell-ECM suspension. Four media reservoirs are attached to the inlets and outlets of the microfluidic channels. (**b**) Representative tissue chamber with a fully-developed vascular network on day 7. Lentivirally-transduced EC (ECFC-EC, red) were visualized by confocal microscopy. Supporting stromal cells are unlabeled. EC migrate outward and anastomose with the microfluidic channels. (Scale bar 100 μm) (**c**) Representative time course of vascular network development (day 2, 4 and 6) (scale bar 100 μm). (**d**) Representative time course of 70 kDa FITC-dextran perfusion through the vascular network on day 7. Inflow was top left and outflow bottom right. The vascular network is fully perfused within 15 minutes. EC were labeled with mCherry. (Scale bar 100 μm). (**e**) Confocal imaging of lentivirally-transduced EC (red) and stromal cells (yellow) reveals that many take up a perivascular position. High magnification views on the right. (**f**) Immunostaining for PDGFR-β and NG2 (both green). EC are expressing mCherry. (**g**) Collagen IV staining (blue) identifies basement membrane deposition.

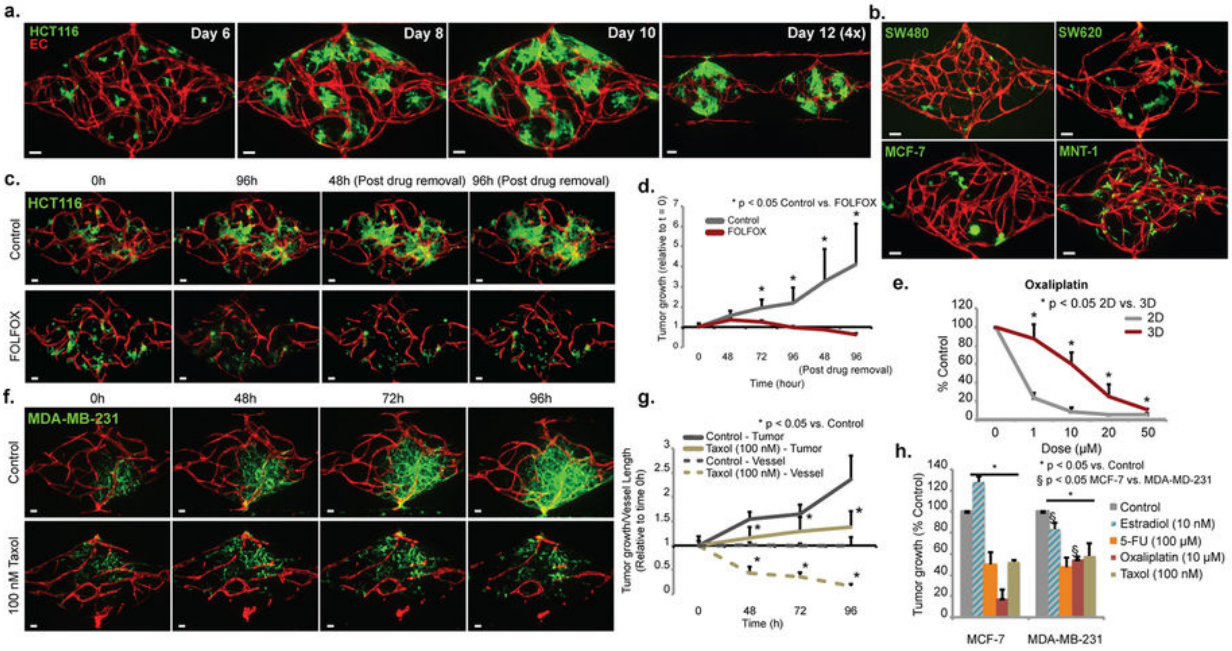

Figure 3.2: A vascularized micro-tumor platform and validations of anti-cancer drug treatment on tumor growth. (**a**) Time course of HCT116 growth in the VMT. Lentivirally-transduced HCT116 (green) and EC (red) were visualized by confocal microscopy. Stromal/perivascular cells were unlabeled. (Scale bar 100 μm). (**b**) The VMT platform supports growth of multiple tumor cell types, including additional CRC (SW620, SW480), breast cancer (MCF-7) and melanoma (MNT-1). Images were taken between days 10 and 12. (**c,d**) Time course of HCT116 (green) response to FOLFOX (10 μM Folinic acid (leucovorin), 100 μM 5-FU, and 5 μM Oxaliplatin) in the VMT. Data are shown relative to t = 0, which is time of first exposure to drug (usually 6–8 days after initiation of culture). Cells were also monitored for 96 h after drug removal. Error bars show mean ± s.d of 3 replicates (n = 2) ($p < 0.05$ control vs treated FOLFOX). (Scale bar 50 μm). (**e**) Dose-response of Oxaliplatin on HCT116 cells. VMTs or cells growing in 2D were exposed to drug for 48 h, and tumor cell number and viability were assessed by fluorescence intensity measurement or XTT assay. Data are normalized to time zero of drug exposure and shown as percentage of control. Error bars show mean ± s.d (n = 3) ($p < 0.05$, 2D vs VMT). (**f,g**) Time course of MDA-MB-231 cells exposed to Taxol (100 nM). Data are normalized to first day of drug exposure. Error bars show mean ± s.d of 3 replicates ($p < 0.05$ control vs treated Taxol). (**h**) Differential effects of anti-tumor drugs on the breast cancer cell lines MCF-7 (ERα+) and MDA-MB-231 (triple-negative). VMTs were first exposed to E2/drugs between days 6 and 8 and cultured for an additional 96 h. Drugs were removed from the media at 48 h. Data are normalized to first day of drug exposure and are shown as percentage of control. Error bars show mean ± s.d (n = 2–4) (*$p < 0.05$ vs control; $^{§}p < 0.05$ MCF-7 vs MDA-MB-231).

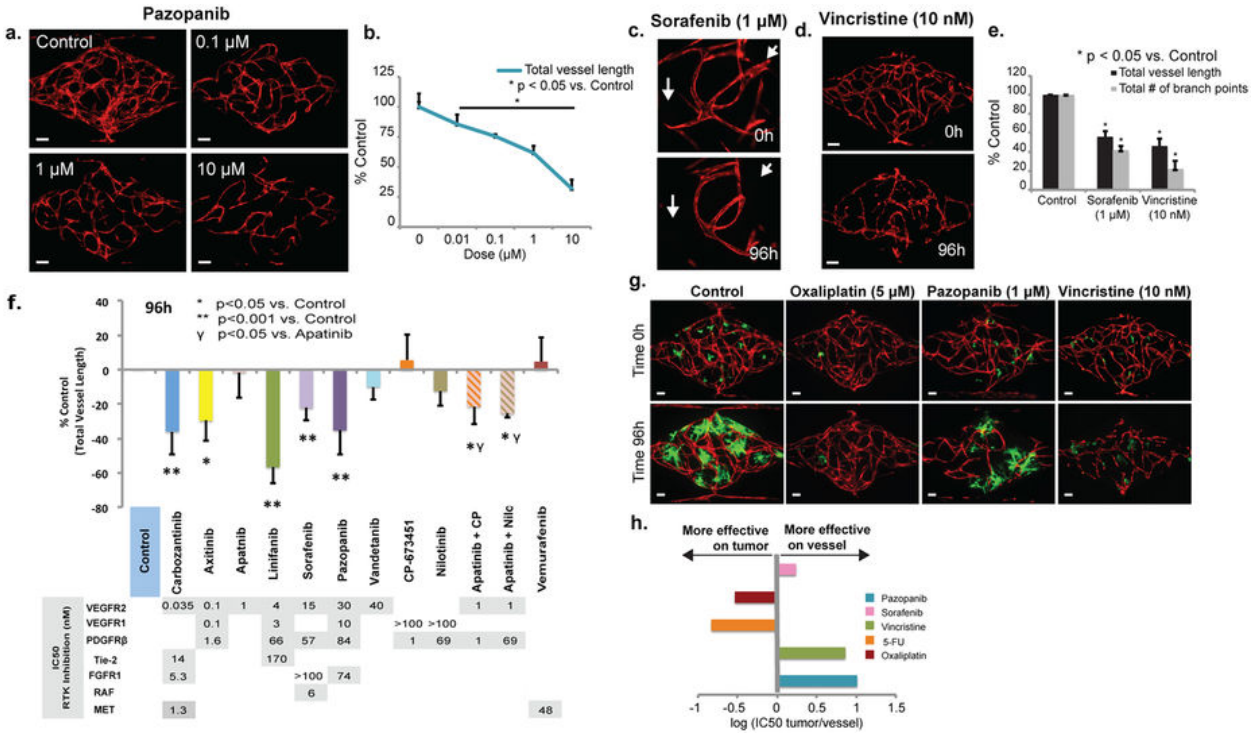

Figure 3.3: Validation of anti-angiogenic drug treatment in the vascularized micro-tumor**.** (**a,b**) Effect of Pazopanib on vascular network integrity. VMOs were exposed to drug from day 4 to 6. Data are normalized to day of first drug exposure and are shown as percentage of control. Error bars show mean ± s.d (n = 3) ($p < 0.05$ vs control). (**c–e**) Effect of the anti-vascular agents, Sorafenib (1 µM) and Vincristine (10 nM) on total vessel length and total number of branch points in the VMO. VMOs were exposed to the drug between days 5 to 7 and cultured for an additional 96 h. Error bars show mean ± s.d (n = 3) ($p < 0.05$ vs control). Sorafenib induces vessel regression (**c**), whereas vincristine induces vascular damage (**d**). (**f**) Effect of 10 different RTK inhibitors on vascular network integrity. VMOs were exposed to drugs between days 5 and 7 and cultured for an additional 96 h. Data are normalized to first day of drug exposure and are shown as percentage of control. Error bars show mean ± s.d (n = 3- 5) (*$p < 0.05$ vs control; **$p < 0.001$; $^{\gamma}p < 0.05$ vs Apatinib alone). (**g**) Anti-cancer drugs that target tumor, vasculature, or both. HCT116 tumor cells in a VMT exposed to Pazopanib (1 µM), Oxaliplatin (5 µM) and Vincristine (10 nM). Images before and after drug exposure are of the same VMT (Scale bar 100 µm). (**h**) Summary of the relative $IC50_{tumor}/IC50_{vessel}$ values (from (**g**) and data not shown) plotted on a log scale. Drugs extending to the right are more effective, relatively, on vessels, whereas those on the left are more effective on tumor cells.

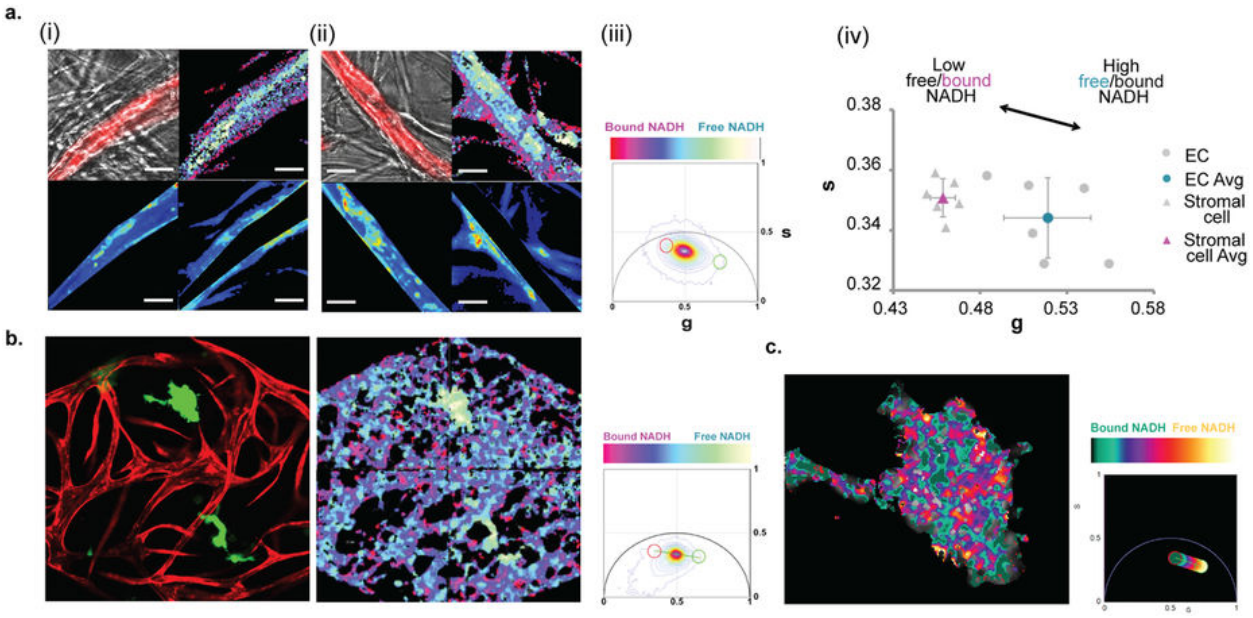

Figure 3.4: Metabolic profile in the vascularized micro-tumor. (**a**) Two different tissue chambers are shown in (i) and (ii). For each: EC (red) overlaid on the bright-field image (top left); 2PE-FLIM map of EC forming vessels and wrapped with perivascular cells (top right); Vessel and perivascular cell regions of interest (ROIs) were selected by manual masking and the average NADH phasor in each of these ROIs was calculated for ECs forming vessels (bottom left) and for the perivascular cells (bottom right), as described in Materials and Methods. Scale bar 20 µm. (iii) NADH FLIM phasor distribution used to create the free/bound NADH color scale. (iv) the average phasors for the ECs and the perivascular cells. Error bars show mean ± s.d of 6 replicates ($n = 3$, $p < 0.05$). (**b**) Left: confocal image of MCF-7 breast tumor cells (red) and vasculature (green). Right: 2PE-NADH FLIM map of the same VMT, and the NADH FLIM phasor distribution used to create the free/bound NADH color scale. (**c**) High resolution 2PE-NADH FLIM map of the tumor shown in (**b**) demonstrating metabolic heterogeneity, and the NADH FLIM phasor distribution used to create the free/bound NADH color scale.

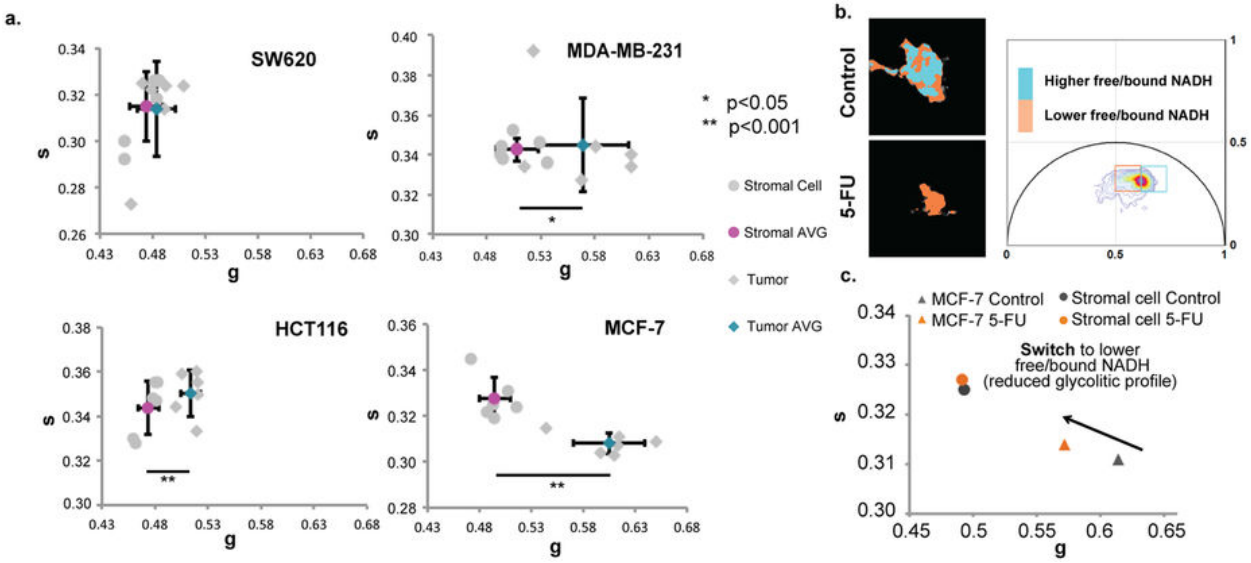

Figure 3.5: Differences in metabolic profile of cancer cells in the vascularized micro-tumor. (**a**) Phasor scatter plots comparing SW620, HCT116, MCF-7 and MDA-MB-231 to their surrounding stroma. Error bars show mean ± s.d ($p < 0.01$ for MCF-7 and HCT116; $p < 0.05$ for MDA-MB-231). (**b**) Top left: NADH FLIM map of MCF-7 cells treated with control or 5-FU (100 µM). Two colors, cyan and orange are used to depict two lifetime phasor distributions with cyan representing a higher free/bound NADH ratio, while orange shows a comparatively lower free/bound NADH ratio. Top right: phasor plot showing NADH phasor distribution. (**c**) Scatter plot showing the NADH phasors for the treated and non-treated conditions for the tumor and stroma shown in (**b**).

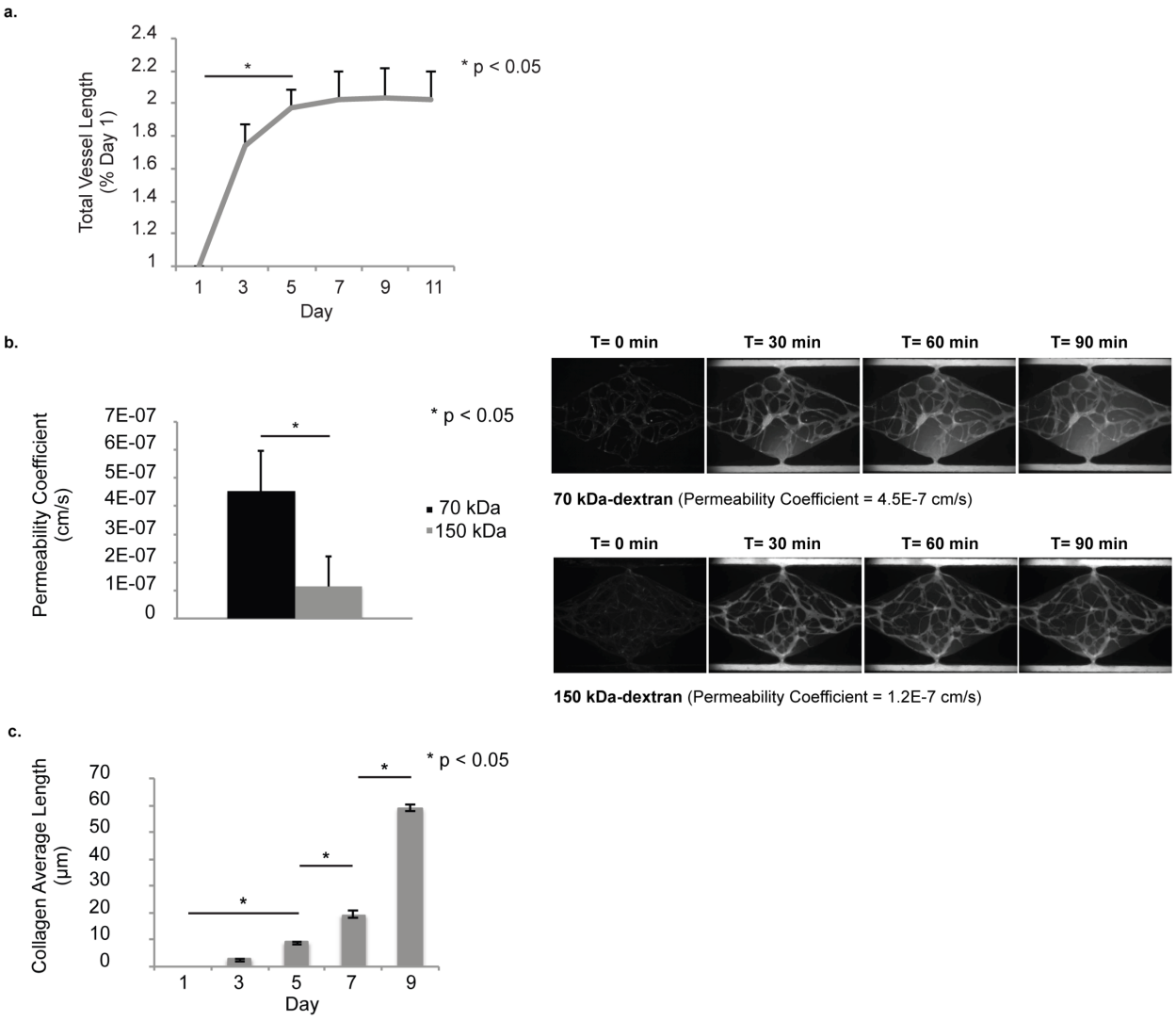

Figure 3.1S: (a) Total vessel length over time, quantified using AngioTool. Error bars represent mean ± s.d of 3 replicates from a representative experiment ($p< 0.05$) (n= 3). (b) Permeability coefficients of the vascular networks perfused with 70 kDa and 150 kDa FITC-dextran for 90 minutes. Error bars mean ± s.d (n = 3) ($p< 0.05$). (c) Time course of collagen I increase in the VMO. Devices were fixed in 4% PFA at different time points and quantification was done using second harmonic generation imaging as described in Material and Methods. Error bars mean ± s.d of 3 replicates ($p< 0.05$).

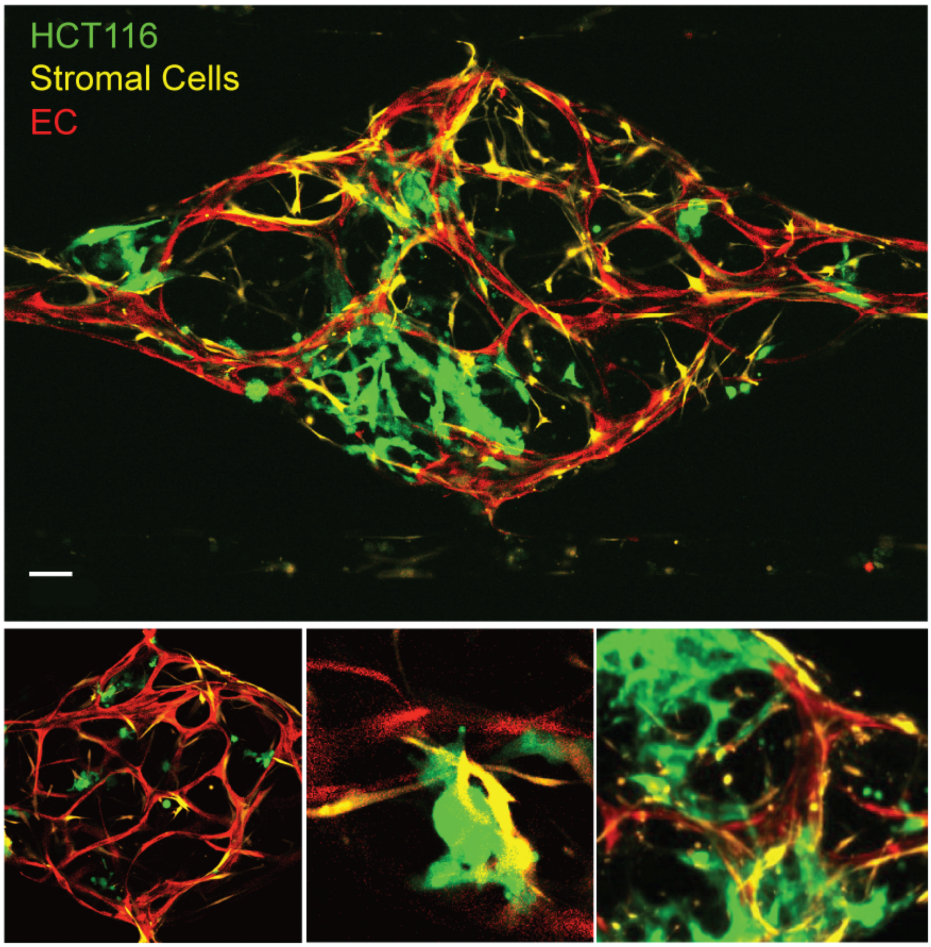

Figure 3.2S: Interactions between microvessels, stromal cells and HCT116 tumor cells. Many of the stromal cells take up a perivascular position. Lentivirally-transduced HCT116 (green), stromal/perivascular cells (yellow) and EC (red) were visualized by confocal microscopy (Scale bar 100 μm).

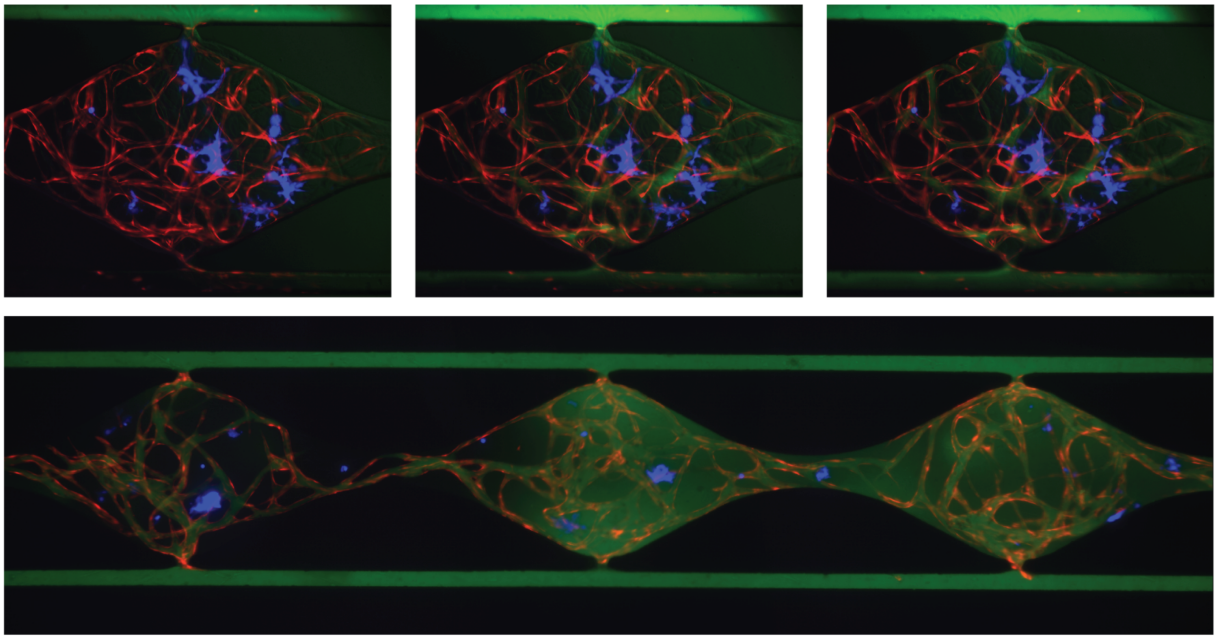

Figure 3.3S: 70 kDa fluorescently-labeled dextran perfusion through 3D VMT. Upper panels show a time course of 70 kDa FITC-dextran (green) flowing through a vascular network (red) in the presence of HCT116 tumor cells (blue). Lower panel shows 70 kDa FITC-dextran flowing through 3 VMTs connected in series.

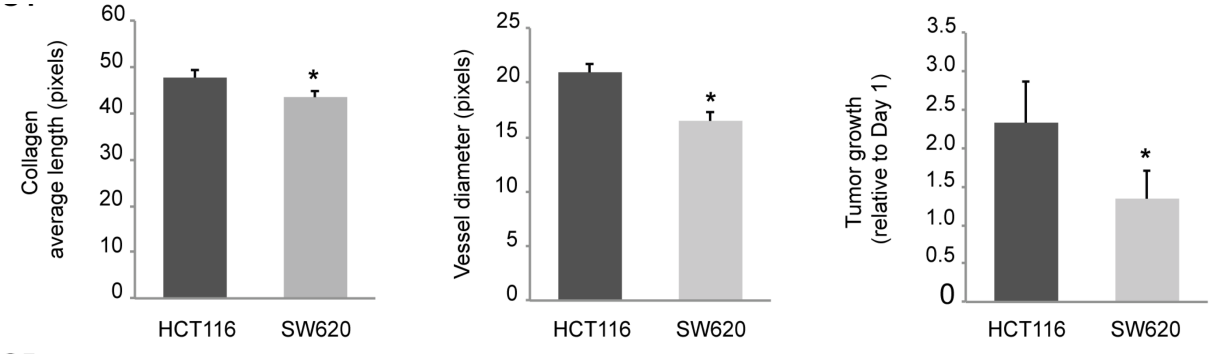

Figure 3.4S: Collagen synthesis, vascular development and tumor growth rate of two different CRC cell lines (SW620 and HCT116). The same number of SW620 and HCT116 tumor cells were co-cultured with EC and stromal cells. Indicated parameters were determined at day 7 of culture. Image J was used for tumor growth quantification. Total vessel length over time was quantified using AngioTool. Vessel diameter was quantified using the MATLAB subroutine (RAVE), and Collagen I content was determined using second harmonic generation imaging as described in Material and Methods. Error bars show mean ± s.d of 3 replicates ($p < 0.05$).

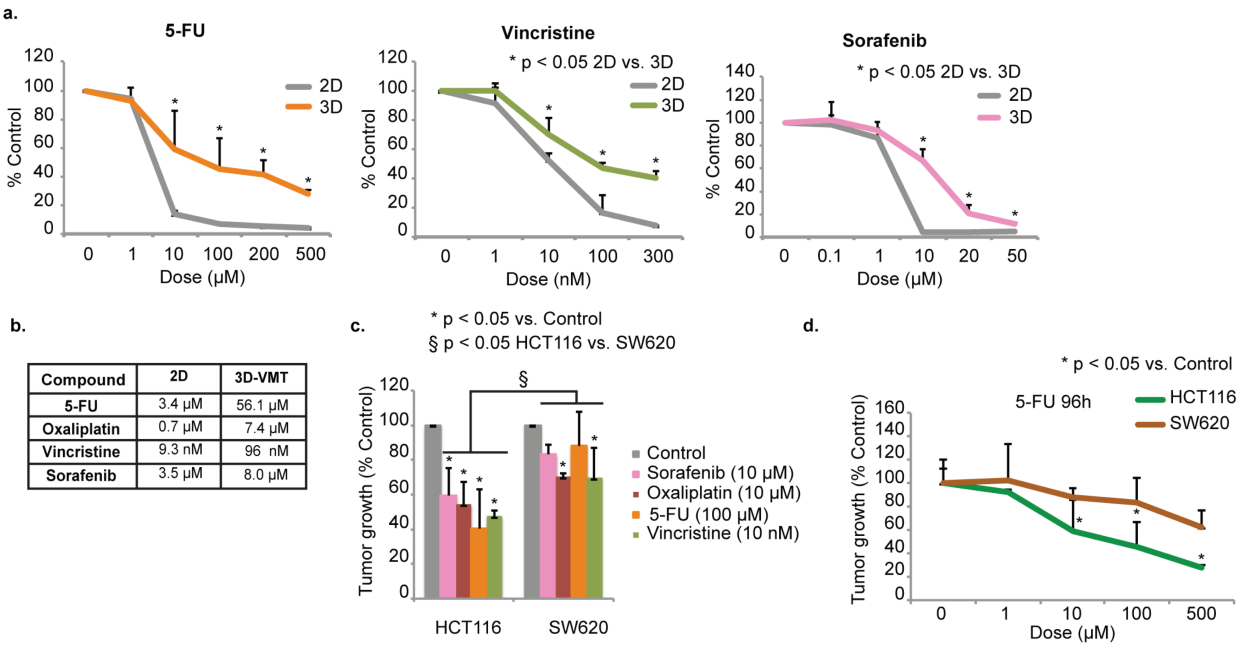

Compound	2D	3D-VMT
5-FU	3.4 μM	56.1 μM
Oxaliplatin	0.7 μM	7.4 μM
Vincristine	9.3 nM	96 nM
Sorafenib	3.5 μM	8.0 μM

Figure 3.5S: (a) Dose response curves for 3 FDA-approved anti-cancer agents, 5-FU, Vincristine and Sorafenib, on HCT116 cells. VMTs or cells growing in 2D were exposed to the drugs for 48 h, and tumor cell number and viability were then assessed, either by fluorescence intensity measurement or XTT assay. Data are normalized to time zero of drug exposure and shown as percentage of control. Three replicates per experiment, error bars show mean ± s.d (n = 3- 7) ($p< 0.05$, 2D vs VMT). (b) Calculated IC50 values for 4 FDA-approved anti-cancer drugs, including the drugs shown in (a) for both 2D and 3D cultures. (c) Tumor drug screening comparison between two CRC that carry different mutations. HCT116 (CTNNB1, CDKN2A, KRAS, PIK3CA, MLH1) and SW620 (KRAS, MAP2K4, TP53, MYC, SMAD4) VMTs were first exposed to drugs between days 6 and 8 and cultured for an additional 96 h. Drugs were removed from the media at 48 h. Data are normalized to first day of drug exposure and are shown as percentage of control. Three replicates per experiment, error bars show mean ± s.d (n = 2- 4) (*$p< 0.05$ vs control; § $p< 0.05$ HCT116 vs SW620). (d) 5-FU dose response comparison between HCT116 and SW620. Data are normalized to first day of drug exposure and are shown as percentage of control. Error bars show mean ± s.d from 3 replicates (n = 2) ($p< 0.05$).

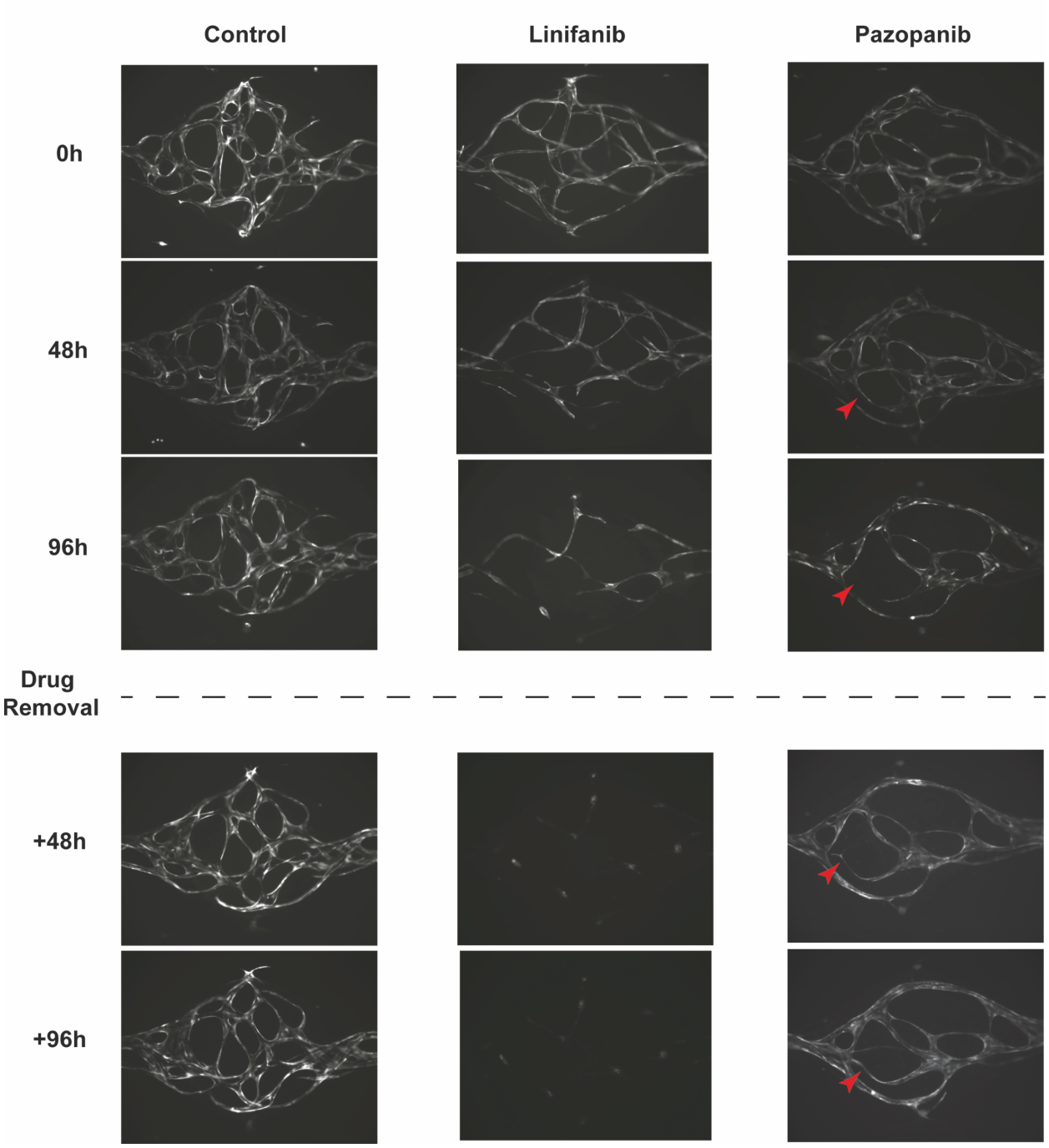

Figure 3.6S: Effect of the anti-vascular agents Linifanib (100 nM) and Pazopanib (100 nM) in the VMO. VMOs were exposed to the drug at day 5 and cultured for an additional 96 h. Drug was then removed, and the VMO were cultured again for an additional 96 h.

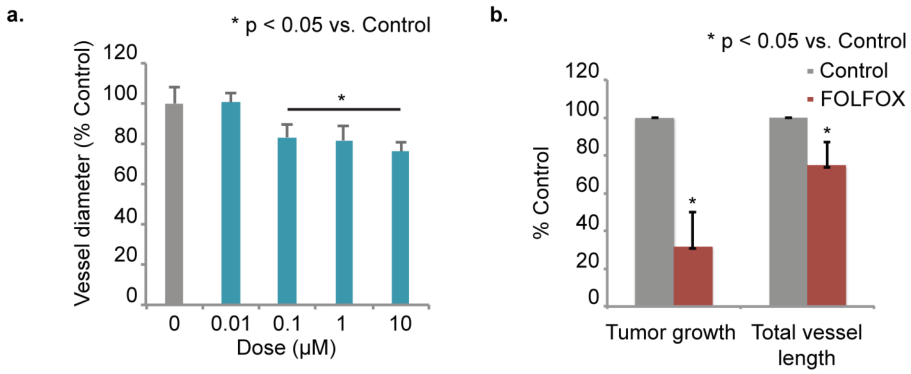

Figure 3.7S: (a) Effect of Pazopanib on vessel diameter in the VMO. VMOs were exposed to drug from day 4 to 6 and then cultured for an additional 96 h. Data are normalized to day of first drug exposure and are shown as percentage of control. Quantification was performed as described in Materials and Methods. Three replicates per experiment, error bars show mean ± s.d ($n = 3$) ($p < 0.05$ vs control). (b) Effect of FOLFOX on tumor growth and total vessel length. Three replicates per experiment. Error bars show mean ± s.d ($n = 2$) ($p < 0.05$ vs control). Data shown are from the same experiment presented in Figure 2c.

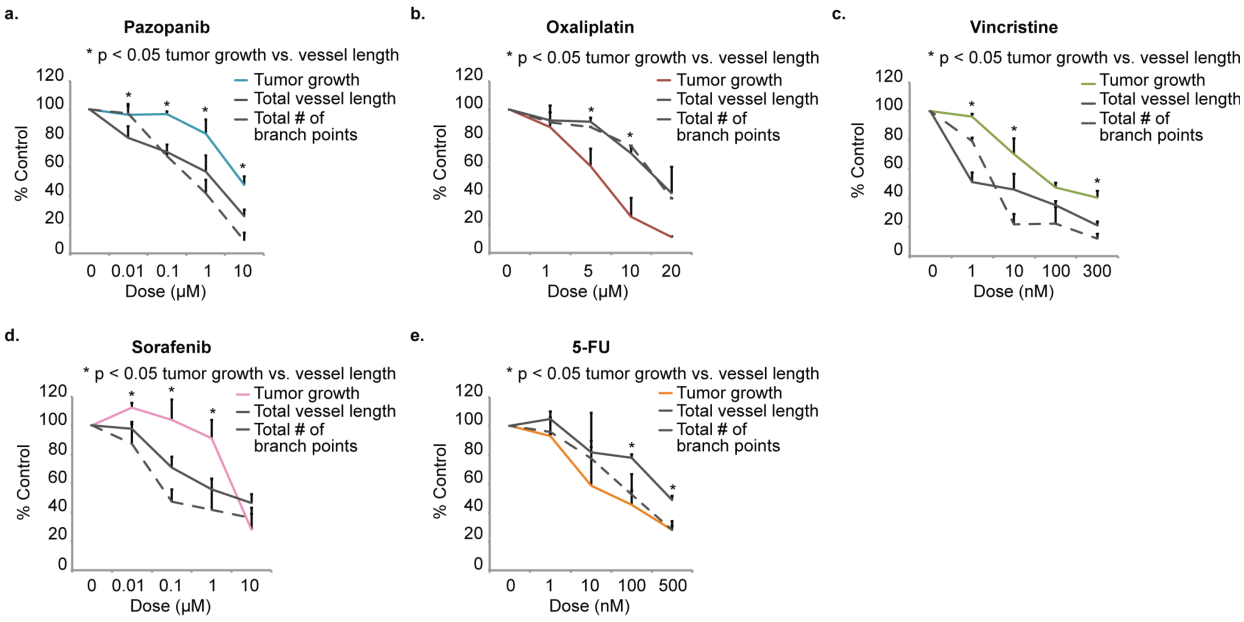

Figure 3.8S: (a-e) Dose response curves of several anti-cancer agents that differentially target HCT116 tumor growth or vasculature in the VMT platform. VMTs were exposed to drug after 4 to 7 days in culture and then monitored for an additional 96 h. Oxaliplatin, Vincristine, and 5-FU were removed from the media at 48 h. Pazopanib and Sorafenib were present for the full 96 h. Data are normalized to time of first drug exposure and are shown as percentage of control. Three replicates per experiment. Error bars show mean ± s.d (n = 2- 5) ($p < 0.05$ tumor growth vs total vessel length).

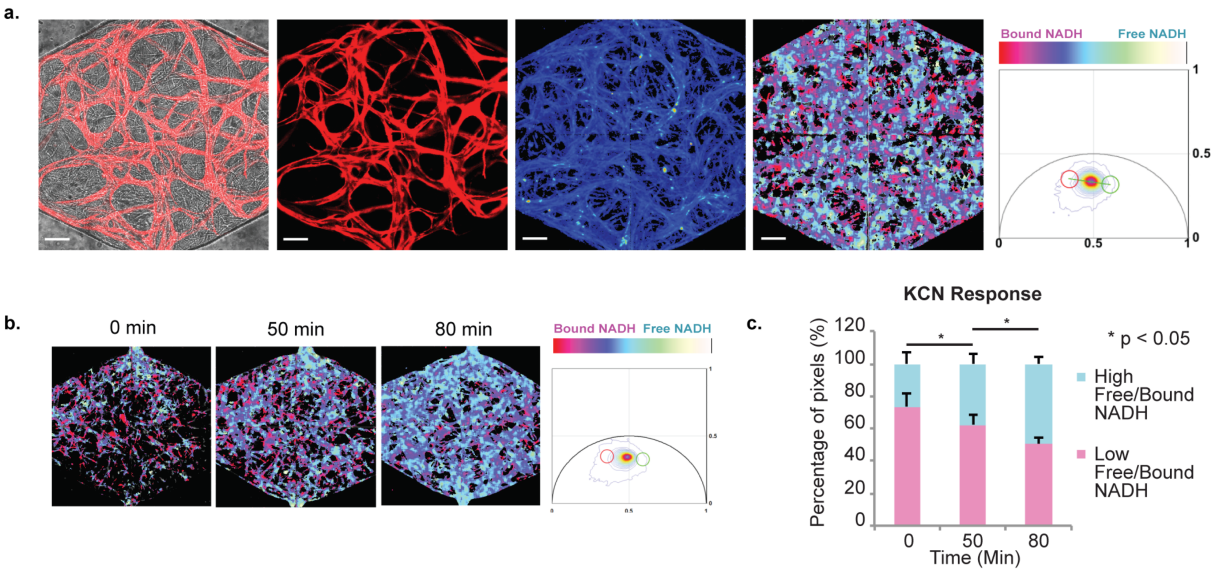

Figure 3.9S: (a) Representative FLIM imaging from a VMO. Lentivirally-transduced EC (red) overlaid onto the brightfield image (left) and alone (center left). Two-photon (2PE) microscopy showing NADH average fluorescence intensity (center) and FLIM NADH map (center right) from the same tissue chamber. NADH FLIM phasor distribution used to create the free/bound NADH color scale (right). (Scale bar 100 μm). (b-c) Chemical disruption of metabolism in the VMO. (b) NADH FLIM map of the tissue chamber before and after 80min of KCN exposure. (c) Quantification of the response of cells to KCN showing poisoning of mitochondrial function by KCN. Shown are mean ± s.d of 3 replicates ($p < 0.05$).

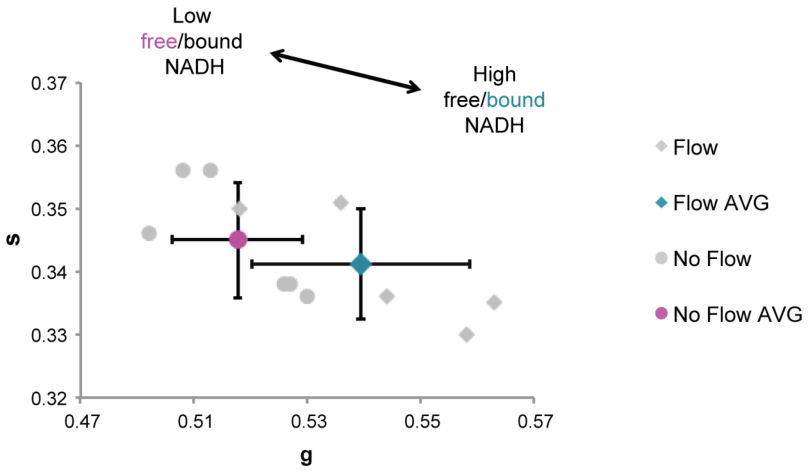

Figure 3.10S: Phasor scatter plot showing a significantly different ratio of free-bound NADH for the vasculature in the absence of flow compared to the presence of flow. Data were obtained 72h after the flow was reduced. Error bars show mean ± s.d ($p < 0.05$).

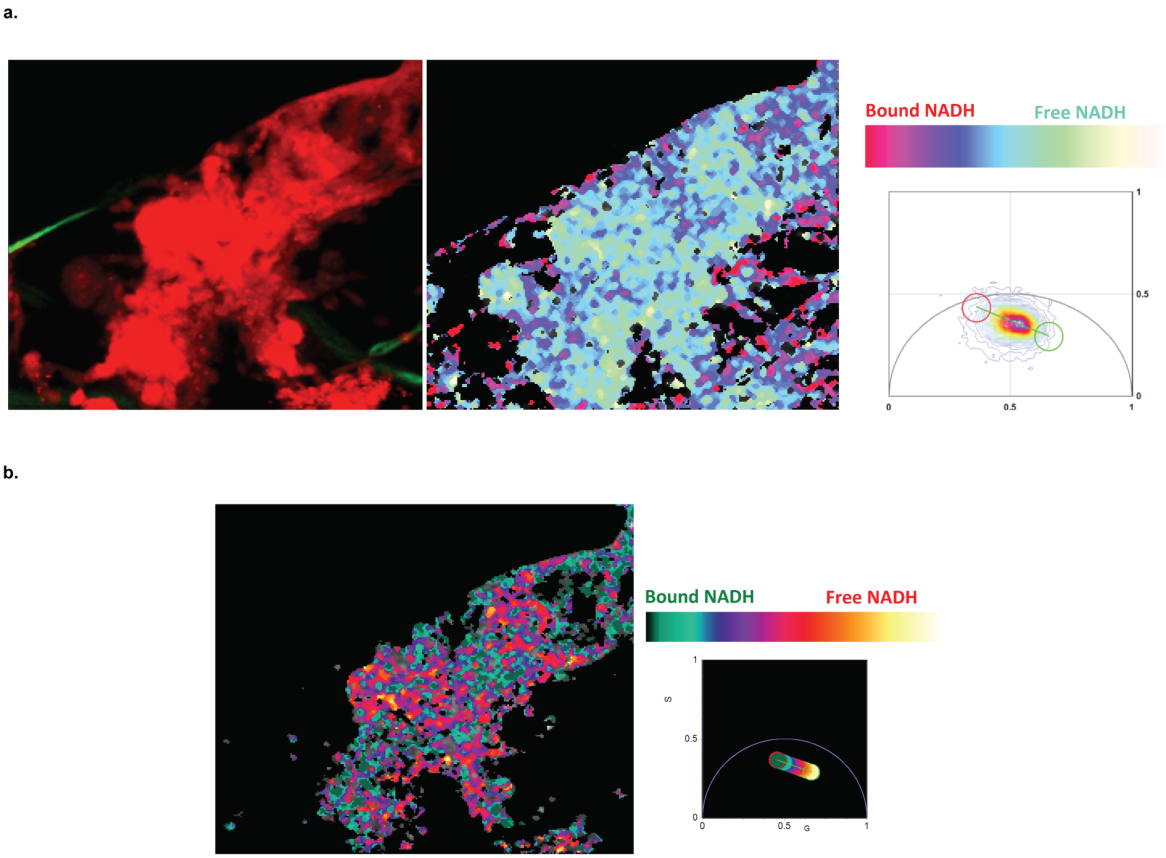

Figure 3.11S: (a) MCF-7 tumor (red) within a VMT and corresponding 2PE-FLIM map showing the tumor cells and surrounding stroma. (b) NADH FLIM phasor distribution of the same tumor color-coded within the tumor only. Note heterogeneous metabolic profile of the tumor.

CHAPTER 4

A vascularized and perfused organ-on-a-chip platform for large-scale drug screening applications

Duc T.T. Phan, ‡ Xiaolin Wang, ‡ Brianna M. Craver, Agua Sobrino, Da Zhao, Jerry C. Chen, Lilian Y.N. Lee, Steven C. George, Abraham P. Lee *, and Christopher C.W. Hughes *

(‡ Contributed equally as first authors, * Contributed equally as senior corresponding authors)

Originally published in Lab on a Chip 2017, 17:511-520

4.1 Abstract

There is a growing awareness that complex 3-dimensional (3D) organs are not well represented by monolayers of a single cell type – the standard format for many drug screens. To address this deficiency, and with the goal of improving screens so that drugs with good efficacy and low toxicity can be identified, microphysiological systems (MPS) are being developed that better capture the complexity of *in vivo* physiology. We have previously described an organ-on-a-chip platform that incorporates perfused microvessels, such that survival of the surrounding tissue is entirely dependent on delivery of nutrients through the vessels. Here we describe an arrayed version of the platform that incorporates multiple vascularized micro-organs (VMOs) on a 96-well plate. Each VMO is independently-addressable and flow through the micro-organ is driven by hydrostatic pressure. The platform is easy to use, requires no external pumps or valves, and is highly reproducible. As a proof-of-concept we have created arrayed vascularized micro tumors (VMTs) and used these in a blinded screen to assay a small library of compounds, including FDA-approved anti-cancer drugs, and successfully identified both anti-angiogenic and anti-tumor drugs. This 3D platform is suitable for efficacy/toxicity screening against multiple tissues in a more physiological environment than previously possible.

4.2 Introduction

Despite continuous advances in drug screening methodology, only a small fraction of drug candidates achieve approval by the US Food & Drug Administration (FDA) for clinical use. As recently reported, over 80% of drug candidates fail during phase II and phase III clinical trials due to lack of efficacy and/or adverse events [1]. These issues are not identified during preclinical studies, largely due to the lack of effective screening methods that can mimic the complexity of human tissue and provide rapid, reliable screening readouts.

The urgent need for an innovative approach to better mimic human drug responses in preclinical studies has driven the development of "organ-on-a-chip" technologies or microphysiological systems (MPS). Utilizing advances in microfluidic technology and 3-dimensional (3D) cell culture techniques, these systems aim to recapitulate the complexity found in vivo, which includes: 3D structure; heterogeneous cellularity; cell–cell interactions; the presence of a complex extracellular matrix (ECM); perfused vasculature; and, biomechanical forces (e.g. shear forces generated by fluid flow) [2]. In recent years, efforts to develop MPS have been focused on recreating human organs such as heart, liver, lung, and brain at the level of their smallest functional unit for toxicity testing and limited drug screening [3-7]. In parallel, several "disease-on-a-chip" platforms have also been developed to model human diseases for basic science research [8, 9]. While these organ-on-a-chip platforms have demonstrated significant improvements in mimicking human organs and disease stages over traditional 2D monolayer culture systems, they are still, in many cases, at the proof-of-concept stage. Many of these platforms require complex peripheral equipment and accessories to operate and maintain, and thus may not be ideally suited for larger-scale compound screening.

Recently, we have developed methods to generate per- fused, vascularized human microtissues in vitro [10, 11]. While we have demonstrated the use of our microfluidic system to create vascularized micro-organs (VMO) and vascularized microtumors (VMT) *in vitro* for drug screening [11], this proto- type was not designed for larger-scale drug screening. Specifically, the former iteration is cumbersome with large medium reservoirs required, which necessitates a larger amount of drug. This is not practical for screening novel compounds, which during the development phase are often only synthesized in small quantities. Additionally, the 96-well plate for- mat is compatible with standard robotic and fluorescent plate readers. To address this need we have redesigned the plat- form to create arrays of standardized and highly reproducible VMOs. The platform conforms to the size and arrangement of a standard 96-well plate and consists of 12 independently addressable tissue units (VMOs) with fluid flow driven by hydro- static pressure. Each unit can be fed with a different drug or drug dose. The platform is user- friendly, does not require external pumps or valves, is easy to load due to the incorporation of independent pressure regulator circuits [12], and re- quires minimal training to operate. Finally, tissues can be easily extracted from each unit for subsequent gene expression analysis. While a multitude of different tissue-specific cell types can be incorporated into the tissue, here we demonstrate the utility of the platform using colon tumor cells.

4.3 Materials and Methods

Platform design

The platform is custom-fitted into a standard 96-well plate format. The design is presented in Figure 4.1 and consists of two polydimethylsiloxane (PDMS) layers assembled to a commercial 96-well plate (FLUOTRACTM 600, Greiner Bio-One) with the bottom of specific wells removed to align with the plat- form (Figure 4.1A). The 2 mm thick middle layer consists of 12 microfluidic device units (denoted as the PDMS device layer) and the bottom layer is a thin transparent polymer mem- brane (HT-6240, Rogers Corp).

Since liquid evaporation at the corner and edge wells is faster than the inner wells of 96-well plates, only 12 microfluidic device units (U1–U12) are usually arrayed within the inner well area to ensure optimal culture condition. For a single unit, 6 horizontal wells (W1–W6) are utilized. The tissue unit consists of 3 tissue chambers (T1–T3) positioned within the footprint of a single well, with one gel loading inlet (L1) and outlet (L2) located at two additional wells (Fig. 1B and C). Based on a previous design, each tissue chamber is 2 mm in length and 1 mm in width, connected to two 100 μm wide microfluidic channels through 50 μm wide capillary burst valves [11]. The tissue chambers, and the outer microfluidic channels are 100 μm deep. To facilitate a robust hydrogel loading process, an on-chip pressure regulator module with one redundant gel outlet (PR) is integrated into each unit [12]. The pressure regulator unit consists of pressure- releasing burst valves that maintain a lower burst pressure at the communication pores of the tissue chamber, and diversion channels that act as an escape route for redundant gel once the injection pressure is over the burst pressure limit. The microfluidic channels are coupled in an asymmetrical design with one medium inlet (M1) and outlet (M2) and in-line fluidic resistors,

which generates interstitial flow across the tissue chambers, while minimizing the area used for each device unit on a 96-well plate (Fig. 1C).

Platform fabrication

Due to the larger configuration required for the 96-well plate format, the PDMS device layer cannot be directly fabricated using soft lithography on a 3 or 4 inch SU-8 silicon mold. To address this challenge, a customized polyurethane master mold is fabricated using 2-part polyurethane liquid plastic (Smooth Cast 310, Smooth-On Inc.) and a micro-molding technique (Figure 4.1S.a) [13]. The PDMS layer is then replicated from the customized polyurethane master mold and holes are punched for inlets and outlets (Figure 4.1S.b). After the micro-molding process, the platform is assembled in two steps. The PDMS layer is first attached to the bottom of a 96- well plate by a chemical gluing method [14]. Briefly, the plastic bottom of the 96-well plate is immersed into a 2% (v/v) aqueous solution of 3-mercaptopropyl trimethoxysilane (Sigma-Aldrich) diluted in 98% methanol, for 1 minute. After hydrolysis and nucleophilic reaction, the alkoxysilane-terminated substrate on the plastic bottom is rinsed with distilled water and dried with nitrogen. The surface-modified well plate and the PDMS layer are then treated with oxygen plasma for 2 minutes, aligned, and bonded together. The 150 μm thin transparent membrane is then bonded to the bottom of the PDMS device layer by treating with oxygen plasma for an additional 2 minutes. To stabilize the bottom layer, the plastic protective sheet on one side of the polymer membrane is kept, while the other side is removed to allow bonding to the PDMS device layer. This protective sheet replaces the glass coverslip traditionally used for microfluidic devices. Although the glass coverslip provides better mechanical support, it hinders the extraction of cells within the tissue chambers for further molecular analysis. The

fully assembled platform (Fig. 4.1S.c). is placed in 60 °C oven overnight, covered with a standard 96-well plate polystyrene lid, and sterilized using UV light for 30 minutes prior to use. A low-power view of 3 tissue chambers inside a single well is shown in Figure 4.1S.d.

Cell culture

Human endothelial colony-forming cell-derived endothelial cells (ECFC-EC) are isolated from cord blood as previously described and with IRB approval [15]. After selection for the CD31+ cell population, ECFC-EC are expanded on fibronectin-coated flasks and cultured in EGM-2 (Lonza). ECFC-EC are then transduced with lentiviruses encoding various fluorescent proteins (mCherry/Addgene: C2 or Venus- GFP/Addgene: V2) and used between passages 4–6. Human normal lung fibroblasts (NHLF) are purchased from Lonza and cultured in DMEM (Corning) containing 10% FBS (Gemini Bio). NHLF are used between passages 6–8. HCT116 colorectal cancer cells, a gift from the UC Irvine Chao Family Comprehensive Cancer Center, are transduced with lentiviruses encoding various fluorescent proteins (including azurite blue/Addgene: azurite). Cells are cultured in DMEM (Corning) containing 10% FBS (Gemini Bio). All cells are cultured at 37^{o}C/20% O_2/5% CO_2.

Loading of tissue chambers

VMO and VMT are established in the platform as previously described [11]. Briefly, ECFC-EC and NHLF are harvested and resuspended at a 1:1 ratio for a final density of 10^7 cells per mL in 10 mg mL^{-1} fibrinogen solution (Sigma-Aldrich). The cell-matrix mixture is quickly mixed in 3 U mL^{-1} thrombin and loaded into the tissue chambers of each unit on the plat- form. By integrating a pressure regulator unit, the fibrin gel is confined inside the tissue chamber with

a smooth gel–air interface at the capillary burst valve. After allowing gel polymerization for 15 minutes, microfluidic channels are coated with mouse natural laminin (1 mg mL^{-1}, Thermo Fisher) for 15 minutes before replacing with cell culture medium EGM-2 (Lonza). Hydrostatic pressure is established at the inlet and outlet medium reservoir wells to generate laminar flow along the microfluidic channels and the interstitial flow across tissue chambers. Hydrostatic pressure is restored to initial levels, and flow direction is switched, every 24 hours to ensure constant culture medium flow and bi-directional cell stimulation. Medium is replaced every other day after embedding.

Immunostaining

The platform is fixed for immunostaining by perfusing 4% paraformaldehyde (PFA) through the medium inlet for 30 minutes at room temperature. After fixing, PFA is replaced with 1× DPBS to wash for 1 hour at room temperature, or over- night at 4^{o}C. The platform is inverted and the bottom polymer membrane is carefully removed. Subsequent procedures are performed using a micropipettor. Each tissue units are washed with 1× DPBS once before permeabilizing for 15 minutes with 0.5% Triton-X100 diluted in DPBS. After permeabilization, tissue units are blocked with 10% goat or donkey serum for 1 hour at room temperature. Each tissue unit are then incubated with polyclonal rabbit anti-human Claudin-5 (Abcam) or rabbit anti-human VE-Cadherin (Enzo Life Sciences) primary antibodies (1:2000 dilution in 5% serum) for 1 hour at room temperature. After washing with 1× DPBS, tis- sue units are incubated with goat or donkey anti-rabbit secondary antibodies (1:2000 dilution in 5% serum) for 45 minutes before washing with DPBS and counter-staining with DAPI. Finally, anti-fade solution is added on top of each tissue unit before mounting with a glass coverslip.

Finite element simulation

Finite element simulations for interstitial flow through ECM embedded in the tissue chamber is performed using COMSOL Multiphysics 5.0 (Comsol Inc., Burlington, MA, USA). The Brinkman's equation is employed for momentum transportation through a porous fibrin gel with low permeability (1.5×10^{-13} m2) confined in the tissue chamber, and is driven by the hydrostatic pressure drop over a period of 24 hours, as previously described [16].

Drug exposure studies

Each device unit containing VMO or VMT is exposed to a standard primary screening concentration of 1 μM. Compounds are obtained from the National Cancer Institute (NCI) Approved Oncology Compound Plate or purchased from Selleck Chemicals. All compounds are dissolved in di- methyl sulfoxide (DMSO) and diluted in the culture medium with less than 0.01% DMSO. For a standard primary screening assay, after culturing for 7 days to allow full development of each tissue unit, culture medium is replaced by medium containing the drugs at the desired concentration, and delivered through the microfluidic channels using the hydrostatic pressure gradient. Hydrostatic pressure is restarted and flow direction is switched every 24 hours. Tissues are exposed to compounds for 72 hours before quantifying the effect on total vessel length and tumor growth.

Cell viability in response to drugs in 2D monolayer cultures is quantified using an XTT assay. Briefly, 10000 cells (ECFC-EC or HCT116) are seeded in triplicate in a 96-well plate and allowed to grow for 24 hours prior to treatment with drugs at 1 μM. XTT assays are performed

after 72 hours of drug exposure and cell viability is normalized to control wells without drug treatment according to the manufacturer's protocol (Sigma-Aldrich).

Time-lapse imaging and time course analysis

Time-lapse image sequences and time course images are taken using a Nikon Ti-E Eclipse epifluorescent microscope with a 4× Plan Apochromat Lambda objective. For close-up imaging of the tissue chambers, a 1.5× intermediate magnification setting is used. For vessel quantitative analysis, total vessel length and vessel percentage area are quantified using AngioTool (National Cancer Institute). For tumor growth quantitative analysis, fluorescent intensity is processed and analyzed using ImageJ (National Institute of Health). Briefly, images are thresholded to select for the fluorescent tumor region, and the mean fluorescence intensity is measured within the threshold region. Tumor total fluorescent intensity is de- fined as the product of the fluorescent area and the mean fluorescent intensity within that region. Final values of vessel and tumor growth quantitative analysis are normalized to initial values at time zero of drug exposure. Three replicates (tissue units) are examined per experiment. Confocal imaging of fluorescent immunostaining is performed on a Leica TCS SP8 confocal microscope using a 20× multi-immersion objective with 2× digital zoom setting. Where adjustments are made to images, these are performed on the entire image, and all images in that experimental group are adjusted to the same settings.

RNA isolation and qRT-PCR analysis

For RNA isolation, the plastic cover underneath the platform is removed and the PDMS region containing the 3 tissue chambers is extracted using a sterile scalpel. Each PDMS piece is transferred into a 1.5 mL tube and resuspended in Trizol for cell lysis. Supernatant is then transferred into a new 1.5 mL tube to extract RNA. Isolated RNA is treated with Turbo DNase (Invitrogen) for 20 minutes. Total purified RNA is synthesized into cDNA using iScript cDNA Synthesis Kit (BioRad) and used for quantitative real-time polymerized chain reaction (qRT-PCR). Average cycle threshold (Ct) values are normalized to 18S expression levels and all samples are measured in triplicate. Primers are designed using PrimerQuest Tool and synthesized by Integrated DNA Technologies. Primer sequences are listed in the Table 4.1S.

Statistical analysis

Data are shown as mean ± standard deviation unless stated. Estimated means, and standard deviation are calculated using Microsoft Excel. Comparison between experimental groups of equal variance is analyzed using student's t-test or one-way ANOVA followed by Dunnett's test for multiple comparisons using GraphPad Prism 7.0. Number of replicates is indicated in the legends. The level of significance is set at $p < 0.05$.

4.4 Results

Finite element simulation of interstitial flow required to induce vasculogenesis

VMOs are generated in this platform through the process of vasculogenesis. In a previous study, we have demonstrated the importance of interstitial flow and the optimal conditions to induce vasculogenesis [16]. We performed time-dependent flow simulations to optimize the hydrostatic pressure, as this device is limited to the smaller volume that a single well can hold (maximum volume: 382 μL) compared to a larger volume in the plastic/glass medium reservoir previously utilized (Figure 4.2). To maximize the interstitial flow duration, the inlet medium volume was initially set to V_{inlet} = 382 μL (P_{inlet} = 10.9 mmH2O or 106.82 Pa) correlating with the maximum well volume, and the outlet medium volume was set to V_{outlet} = 50 μL (P_{outlet} = 1.38 mmH2O or 13.52 Pa) correlating with the minimum volume after accounting for liquid evaporation. Fig. 2A shows hydrostatic pressure (color scale) and flow velocity profile (streamline) in a whole tissue unit at steady state. Interstitial flow across the tissue chamber was then examined to determine if it is sufficient to induce vasculogenesis, based on the limits we previously established [16]. Because of the coupled microfluidic channel design, the hydrostatic pressure difference at the inlet and outlet reduces over time, leading to reduction in interstitial flow. This gives rise to concern of insufficient induction of vasculogenesis inside the tissue chambers. To address this issue, flow simulation was performed for 24 hours with the initial hydrostatic pressure setting (http://www.rsc.org/suppdata/c6/lc/c6lc01422d/c6lc01422d2.mov). he hydrostatic pressure and interstitial flow velocity in both vertical (Figure 4.2B) and horizontal (Figure 4.2S). directions are within the optimal range (0.1–11 μm^{-1}) previously reported [16] to continuously induce vasculogenesis. As shown in Figure 4.2B, each line represents the hydrostatic pressure and interstitial flow velocity vertically across a tissue chamber from time T

= 0 hour to T = 24 hours. Over the course of 24 hours, the hydrostatic pressure difference is maintained between 8 to 19 Pa (0.82 to 1.94 mmH2O), and the interstitial flow velocity is maintained between 1.22 to 22.36 μm s^{-1}. In Figure 4.2S, flow simulation in the horizontal direction across a tissue chamber indicates that the hydrostatic pressure difference is uniform, ranging between 57.8 and 59.2 Pa (5.89 to 6.03 mmH2O), and the interstitial flow velocity is maintained between 0.37 and 2.67 μm s^{-1}. A summary of the flow simulation is shown in Table 1. We conclude from these studies that if the hydrostatic pressure difference at the medium inlet and outlet is reset every 24 hours, then sufficient interstitial flow is maintained across the tissue chambers to induce vasculogenesis.

Generation of vascularized tissues is highly reproducible

Three important factors were considered when designing the platform: user-friendliness, reproducibility, and robustness. Although monolayer and spheroid screening systems do not accurately represent tissue complexity, they are still widely adopted due to their simplicity and user-friendliness. Micro-fluidic systems, while providing a dynamic flow environment, often require additional equipment to support the micro-fluidic device, as well as extensive user training. To address these issues, the flow system utilized in our platform is solely driven by hydrostatic pressure, thus eliminating the need for external pumps and tubing. In addition, to improve user- friendliness and reproducibility, an on-chip pressure regulator that facilitates reproducible hydrogel loading was integrated into each unit on the platform [12]. This integration has minimized the required training time to successfully embed the cell-matrix mixture into each unit down to a single day, thereby alleviating a major bottleneck in our earlier

studies. The process is highly reproducible with, on average, 11 out of 12 units successfully loaded on each platform.

Successfully loaded device units developed robust and uniform vascular networks within 7 days. Figure 4.3A shows vascular networks formed inside the 3 tissue chambers on day 7. To confirm vascular perfusion, 70 kDa FITC dextran (25 μg mL^{-1}) was introduced to the medium inlet and tissue units were monitored for 30 minutes. As shown in the same figure, 70 kDa dextran was perfused throughout the vasculature in the three tissue chambers. Perfusion is highly consistent in 12 tissue units within a single platform, as shown in Figure 4.3S. While anastomotic connections between the vascular net- works and the microfluidic channels formed naturally in all 12 tissue units, the seal is not always as tight as we see when lining EC inside the microfluidic channels [10]. Immunostaining of tight junctions (Claudin-5) and adherens junctions (VE-Cadherin) on day 7 post-embedding in Figure 4.3B and C demonstrated a mature, high integrity vasculature.

The vessel area percentage and total vessel length in each tissue chamber were quantified to assess vascular formation on a successfully loaded platform (Figure 4.4). Quantification demonstrated that the percent vessel coverage and total vessel length between the tissue chambers (n = 36 tissue chambers) in a single platform (n = 12 units) are highly consistent, with a coefficient of variation (CV) equal to 10.2% and 9.8%, respectively (Figure 4.4A). To further assess the reproducibility be- tween different platforms, the average percent vessel coverage and total vessel length of each unit on two independent platforms were quantified (Figure 4.4B). These are also consistent, with CV equal to 12.4% and 11.9% respectively. We com- pared these CVs to a standard 2D assay. We plated 10000 fluorescent-tagged EC into each well of two 96-

well plates (n = 36 wells, 2 plates) and allowed the cells to adhere for 2 hours. Fluorescent intensity was then measured in each well using a fluorescent plate reader. The calculated CV for these monolayer cultures in 2 independent well plates was 12.8% (Figure 4.4S). Thus, the calculated CVs of 2D monolayer culture versus complex 3D cultures in our platform are compatible, showing that our system is highly robust and reproducible.

Analysis of gene expression in the platform

An important advance over previous iterations of the platform, which were also limited to single units versus the twelve we have here, is our ability to extract RNA for gene expression analysis. To demonstrate the potential of the platform for gene expression analysis, units were challenged with TNF-α (20 ng mL^{-1}, n = 12) for 24 hours, or were left untreated (n = 12), and total RNA was extracted for analysis of VCAM-1, E-Selectin, and ICAM-1 by qRT-PCR. TNF-α is a known strong inducer of all three genes in EC [17]. Figure 4.5 shows average gene expression levels of TNF-α treated cells com- pared to control, from 3 independent experiments. Consistent with previous reports [17], TNF-α increased expression of VCAM-1 (average 2.4 fold), E-Selectin (average 3.3 fold), and ICAM-1 (average 6.8 fold). These results demonstrate the potential use of our platform for studying gene expression levels in a 3D, vascularized and perfused tissue *in vitro*.

Drug screening validation

We have previously reported a vascularized tumor model using an early iteration of our microfluidic platform and demonstrated its application for anti-cancer drug screening [11]. To demonstrate the potential use of our platform for anti-cancer drug screening at a larger scale, the

colorectal cancer cell line HCT116 was embedded with EC and stromal cells to create a VMT in each device unit. The VMTs were allowed to develop for 7 days prior to drug exposure. To confirm vascular perfusion in each VMT, 70 kDa rhodamine B dextran (25 μg mL^{-1}) was introduced to the medium inlet and tissue units were monitored for 30 minutes (Fig. 6A). All 12 VMTs within a single platform had perfused vascular networks (Figure 4.5S).

A blinded, primary drug screening at 1 μM concentration was performed using a panel of FDA-approved anti-cancer compounds aliquoted and coded by an investigator not involved in this study: bortezomib, vincristine, CP-673451, linifanib, tamoxifen, axitinib, sorafenib, mitomycin C, vorinostat, and gemcitabine. For negative control com- pounds, isoprenaline and propranolol were chosen. A summary of these compounds and their targets is shown in Table 4.2S. VMTs were allowed to develop for 7 days before exposure to drugs. Images of vasculature and tumors were captured before drug treatment to compare drug effects after 72 hours. As shown in Figure 4.6B, tested compounds showed a wide range of efficacy. Representative images before and after 72 hours of drug treatment are shown in Figure 4.6C and Figure 4.6S. Isoprenaline and propranolol, two negative control com- pounds, showed no effect on either tumor growth or the vasculature. Bortezomib and linifanib effectively targeted both tumor growth and the vasculature. Other compounds have preferential effects on either tumor growth or the vasculature. Tamoxifen, mitomycin C, gemcitabine, and vorinostat were more effective in targeting tumor growth, while vincristine and axitinib showed preferential effects on targeting the vasculature. Over longer treatment times targeting the vasculature also reduces tumor growth due to reduced nutrient supply [11].

We performed power calculations based on these data, with an alpha (significance level) of 0.05 and a power of 0.8, for both anti-vessel and anti-tumor responses. For drugs such as bortezomib, vincristine, mitomycin C, gemcitabine, vorinostat and tamoxifen the required number of replicates for seeing anti-tumor effects was 4–7, well within the range of the platform. When assaying for anti-vascular effects we found that the required number of replicates for bortezomib, vincristine, linifanib, axitinib and sorafenib was 2–4, again well within the range of the platform.

Tumor cells and EC behave quite differently in 2D cultures than they do in 3D [11] and so we compared the efficacy of the above panel of drugs against the same tumor cells and EC used above, but in 2D monolayer cultures. Perhaps not surprisingly we saw dramatic differences (Figure 4.7S), including the ineffectiveness of drugs such as mitomycin C, gemcitabine, and vorinostat on HCT116 cells in 2D com- pared to their strong anti-proliferative effects in the VMT. Similarly, several drugs were detrimental to EC viability in 2D but had little to no effect on vascular stability in 3D cultures.

In conclusion, highly reproducible VMTs can be grown in this platform and used for drug screening with robust read- outs for drug efficacy on tumor growth and the associated vasculature.

4.5 Discussion

The development of this platform represents a significant advance in the development of drug discovery tools. Building on our previous work that generated in vitro perfused, vascularized microtissues, we have standardized the platform design to fit into a 96-well plate format, making it more suit- able for larger-scale drug screening applications. One of the major advantages of this platform compared to other micro- physiological systems is its simple, user-friendly design that requires no external pumps or tubing, and minimal user training to load and operate. The platform is compact and can be easily transferred between laboratories, requiring no additional equipment beyond a standard incubator. Highly reproducible, living vascular networks form inside the tissue chambers allowing for a more physiologic representation of human tissues than has been previously possible in other drug-screening platforms. A small fluid volume requirement for each tissue unit allows for large-scale primary drug screenings at low cost. In particular, for novel compound development, where compound synthesis is expensive, only a small quantity of the compound is required. In addition, RNA extraction from the tissue chambers allows for gene expression analysis and probing of mechanism.

A power analysis based on the data presented here suggests that for compounds with efficacy similar to those tested, a number of replicates between 3 to 7 may well be sufficient to reliably identify hits. For smaller effects the number of replicates may be unreasonably high. This, combined with the higher complexity of the platform compared to standard 96- or 384-well plate assays, leads us to conclude that the VMT platform will be better suited to preclinical testing of a smaller subset of compounds (<100) rather than screens of large libraries containing tens of thousands of compounds.

While the VMT platform has many advantages, there are still some limitations in our approach. First, due to the limited volume of the wells in a 96-well plate, the optimal hydro-static pressure difference cannot be maintained for more than 24 hours. As a result, it is necessary to add additional medium each day to maintain the hydrostatic pressure head and a constant fluid flow rate. However, this could be addressed in future work by customizing a taller 96-well plate that can hold more volume per single well, or a plug-in adapter to increase the well depth for the standard 96-well plate.

Second, because of a smaller hydrostatic pressure difference between the inlet and outlet, the flow velocity generated in this platform is approximately twice lower than the physio- logical blood flow velocity through capillaries [18], resulting in a lower shear stress exerted on the vascular wall. Our estimation for shear stress exerted on the vascular wall in this platform is 2 to 3 times lower than what vascular capillaries experience in vivo [19]. Thus, the platform has some limitations when studying the effects of shear stress on vascular gene expression and morphology. However, it is worth noting that shear stress is the product of flow rate and fluid dynamic viscosity. Blood is a non-Newtonian fluid with high fluid dynamic viscosity, thus the shear stress exerted on the vascular wall in vivo is higher than cell culture medium, a Newtonian fluid that is comprised mainly of water. A higher shear stress could be achieved with the current flow rate if the cell culture medium is modified to increase its dynamic viscosity, something we are currently examining.

It should be noted that the vasculature in the VMTs is leakier compared to the vasculature in VMOs discussed earlier, and the degree of leakiness varies widely between each VMT on a single platform. This phenomenon is perhaps not surprising, as tumor-associated vasculature is

known to be leakier than normal vasculature [20]. Thus, the VMTs in this platform may be a useful model of the tumor microenvironment in vivo.

Although the screening readout is robust, manual operations under the microscope are still required for drug efficacy analysis. Thus, before the platform becomes truly useful for screening with a larger set of compounds the quantification and data analysis processes needs to be automated. This can be done through a customized fluorescent plate reader, or an automated microscope camera system to capture images at different time points. In addition, a machine-learning algorithm can be utilized to interpret data and predict potential "hit" candidates for secondary screening. We are currently exploring these approaches.

4.6 Conclusions

In this paper, we have presented a novel organ-on-chip plat- form comprising human vascularized microtissues suitable for drug screening applications. The platform is custom- fitted to a standard 96-well plate format with a simple, easy- to-operate design. Vascularized microtissues grown in this platform are highly reproducible and the vasculature is fully functional. In addition, RNA can be extracted from the tis- sues for gene expression analysis. Finally, we show that the VMT platform can successfully identify anti-cancer and anti- vascular drugs. This platform is an advance in the field of organ-on-chip research and it will be a useful tool for drug discovery.

4.7 Author contributions

D. T. T. P. and X. W. designed and implemented the plat- form, performed experiments, interpreted data, and wrote the manuscript. B. M. C. performed experiments, analyzed and interpreted data. A. S. contributed knowledge to drug se- lection and the blind screening experiment. D. Z. contributed to finite element simulation and platform microfabrication. J. C. C. and L. Y. N. L. performed experiments and analyzed data. S. C. G. contributed knowledge to project development and edited the manuscript. A. P. L. and C. C. W. H. conceived the project, interpreted data, and wrote the manuscript. All authors read and approved the manuscript.

4.8 Conflict of interests

S. C. G., A. P. L., and C. C. W. H. are founders of 4Design Bio-sciences, LLC and Kino Biosciences Inc.

4.9 Acknowledgements

The authors would like to thank Chinh Tran for help with microfabrication, and Michaela Shuler Hatch and Kimberly Lim for help with cell isolation. This work was supported by grants from the National Institutes of Health: R01 CA180122 (PQD5), and UH3 TR00048. C. C. W. H. receives support from the Chao Family Comprehensive Cancer Center (CFCCC) through an NCI Center Grant award P30A062203. X. W. receives support from National Natural Science Foundation of China (No. 31600781).

4.10 References

1. Arrowsmith, J. and P. Miller, *Trial watch: phase II and phase III attrition rates 2011-2012.* Nat Rev Drug Discov, 2013. **12**(8): p. 569.
2. Fabre, K., C. Livingston, and D. Tagle, *Organs-on-chips (microphysiological systems): tools to expedite efficacy and toxicity testing in human tissue.* Exp Biol Med (Maywood), 2014. **239**(9): p. 1073-7.
3. Brown, J., et al., *Recreating blood-brain barrier physiology and structure on chip: A novel neurovascular microfluidic bioreactor.* Biomicrofluidics, 2015. **9**(5).
4. Esch, M., et al., *Modular, pumpless body-on-a-chip platform for the co-culture of GI tract epithelium and 3D primary liver tissue.* Lab Chip, 2016. **16**(14): p. 2719-29.
5. Huh, D., et al., *Reconstituting organ-level lung functions on a chip.* Science 2010. **328**(5986): p. 1662-8.
6. Mathur, A., et al., *Human iPSC-based cardiac microphysiological system for drug screening applications.* Sci Rep, 2015.
7. Shi, P., et al., *Synapse microarray identification of small molecules that enhance synaptogenesis.* Nat Commun, 2011. **2**(510).
8. Jeon, J., et al., *Human 3D vascularized organotypic microfluidic assays to study breast cancer cell extravasation.* Proc Natl Acad Sci U S A, 2015. **112**(1): p. 214-9.
9. Kim, H., et al., *Contributions of microbiome and mechanical deformation to intestinal bacterial overgrowth and inflammation in a human gut-on-a-chip.* Proc Natl Acad Sci U S A, 2016. **113**(1): p. E7-15.
10. Wang, X., et al., *Engineering anastomosis between living capillary networks and endothelial cell-lined microfluidic channels.* Lab Chip, 2016. **16**(2): p. 282-90.
11. Sobrino, A., et al., *3D microtumors in vitro supported by perfused vascular networks.* Sci Rep, 2016.
12. Wang, X., et al., *An on-chip microfluidic pressure regulator that facilitates reproducible loading of cells and hydrogels into microphysiological system platforms.* Lab Chip, 2016. **16**(5): p. 868-76.
13. Desai, S., D. Freeman, and J. Voldman, *Plastic Masters-rigid templates for soft lithography.* Lab Chip, 2009. **9**(11): p. 1631.
14. Wu, W., et al., *Instantaneous room temperature bonding of a wide range of non-silicon substrates with poly(dimethylsiloxane) (PDMS) elastomer mediated by a mercaptosilane.* Lab Chip, 2015. **15**(13): p. 2819-25.
15. Melero-Martin, J., et al., *In vivo vasculogenic potential of human blood-derived endothelial progenitor cells.* Blood, 2007. **109**(11): p. 4761-8.
16. Hsu, Y., et al., *Full range physiological mass transport control in 3D tissue cultures.* Lab Chip, 2013. **13**(1): p. 81-9.
17. Mackay, F., et al., *Tumor necrosis factor alpha (TNF-alpha)-induced cell adhesion to human endothelial cells is under dominant control of one TNF receptor type, TNF-R55.* J Exp Med., 1993. **177**(5): p. 1277-86.
18. Ivanov, K., M. Kalinina, and Y. Levkovich, *Blood flow velocity in capillaries of brain and muscles and its physiological significance.* Microvasc Res, 1981. **22**(2): p. 143-55.
19. Papaioannou, T. and C. Stefanadis, *Vascular wall shear stress: basic principles and methods.* Hellenic J Cardiol, 2005. **46**(1): p. 9-15.

20. McDonald, D. and P. Baluk, *Significance of blood vessel leakiness in cancer.* Cancer Res, 2002. **62**(18): p. 5381-5.

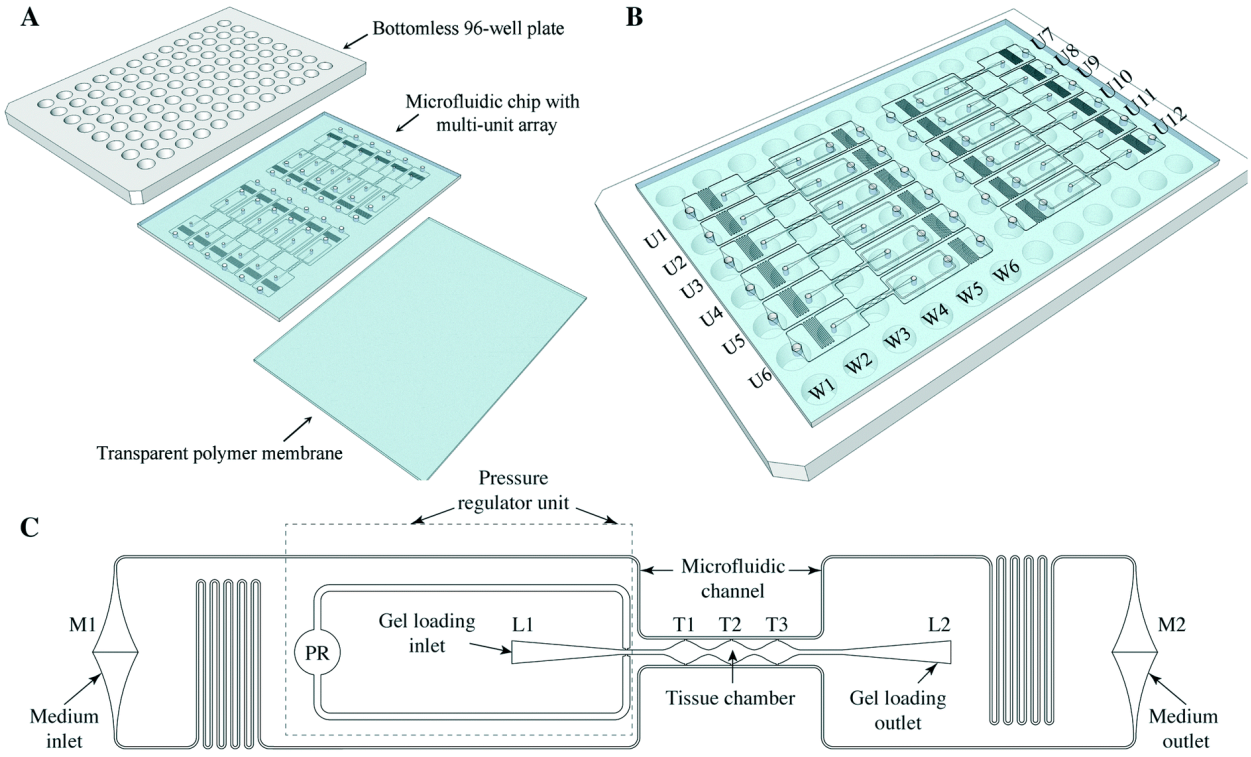

Figure 4.1: Microfluidic platform design. (A) Schematic of the platform assembly. The PDMS layer containing the microfluidics, and a transparent polymer membrane are bonded to a bottomless 96-well plate. (B) Schematic of a fully assembled platform (viewed from below), with 6 tissue units arranged on half of the well plate (U1–U6), and another 6 tissue units arranged on the opposite side. Each tissue unit occupies 6 horizontal wells (W1–W6). In practice, tissue is loaded through U1/W2 or U1/W4, and medium flows from U1/W1 to U1/W6. The pressure regulator outflow occupies U1/W5. (C) Schematic of one tissue unit, which consists of 3 tissue chambers (T1–T3) connected to 2 adjacent microfluidic channels, 2 gel loading ports (L1–L2), 2 medium ports (M1 and M2), and one pressure regulator unit (PR).

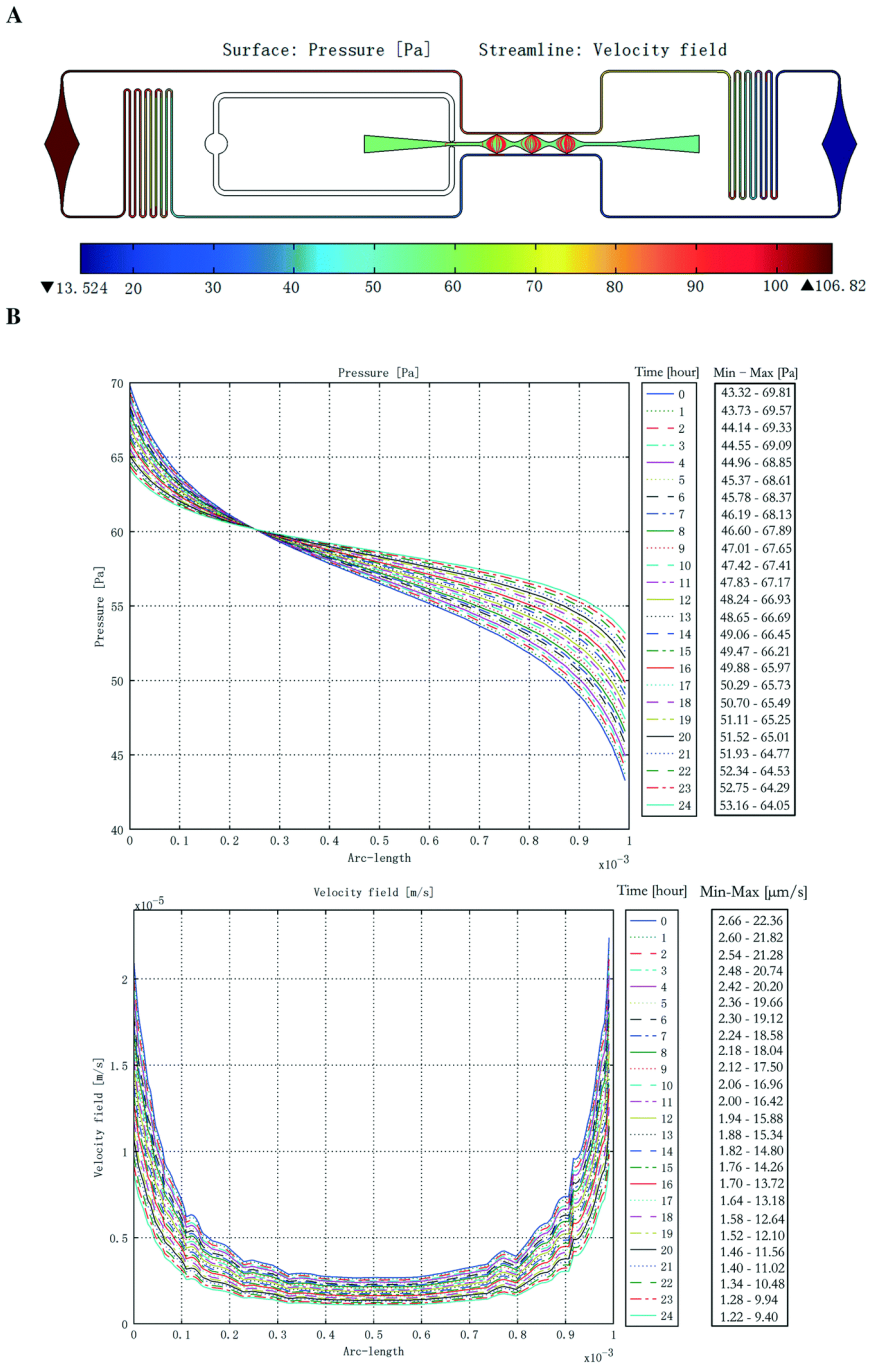

Figure 4.2: Finite element simulation of the interstitial flow required to induce vasculogenesis. (A) Simulated hydrostatic pressure (color scale. Unit: Pa) and flow velocity (streamline) of a whole tissue unit at steady state. (B) Simulated hydrostatic pressure (unit: Pa) and flow velocity (unit: m s^{-1}) in vertical direction across a tissue chamber from time $t = 0$ hour to $t = 24$ hours.

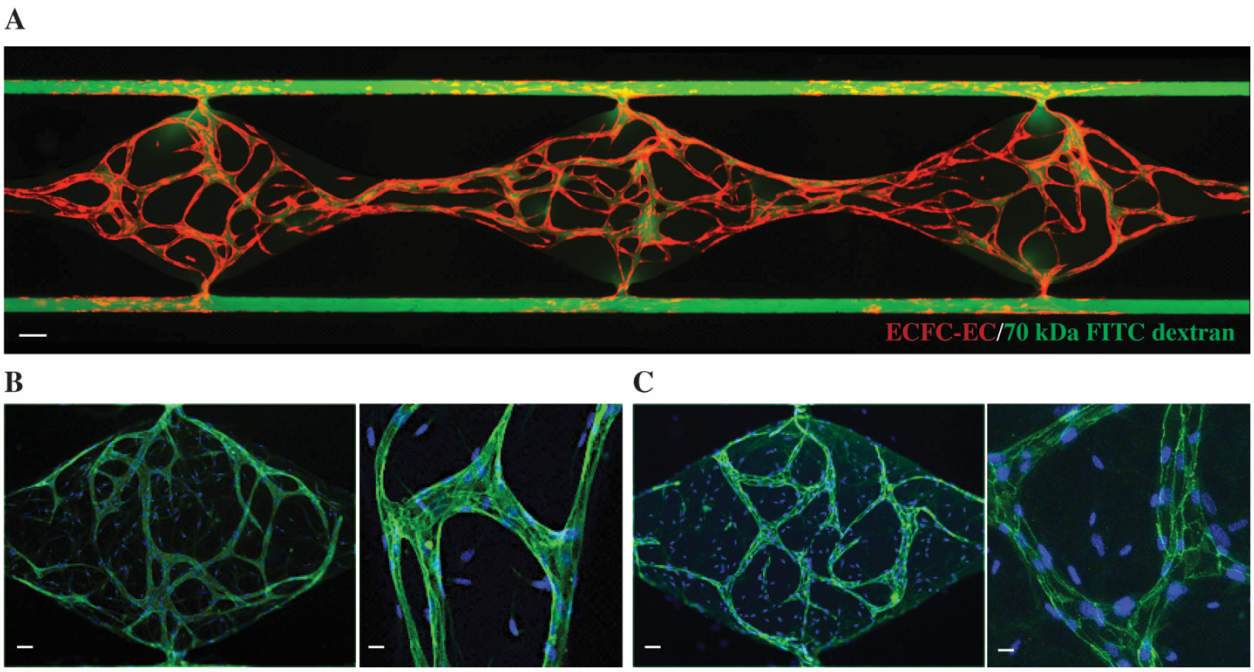

Figure 4.3: Vascular network formation inside one tissue unit. (A) ECFC-EC (mCherry) formed vascular networks inside the 3 tissue chambers on day 7. 70 kDa FITC-dextran was introduced to the medium inlet and allowed to perfuse through the vasculature for 30 minutes. Scale bar = 100 μm. (B) Immunostaining of Claudin-5 (Alexa Fluor 488) and DAPI for nuclei under 4× and 20× microscope objectives. Scale bar = 50 μm. (C) Immunostaining of VE-Cadherin (Alexa Fluor 488) and DAPI for nuclei under 4× and 20× microscope objectives. Scale bar = 50 μm.

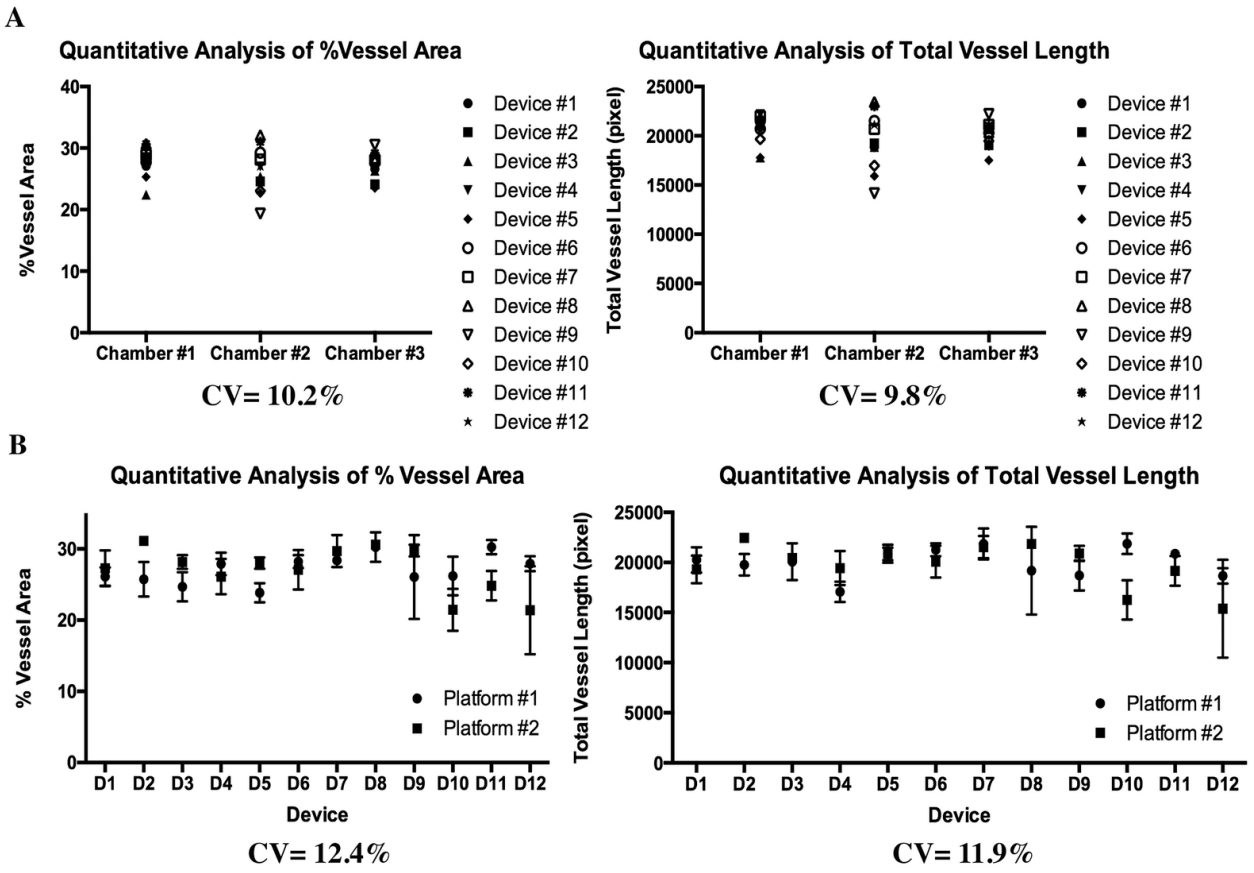

Figure 4.4: Quantitative analysis of vascular networks formed inside the platform. (A) Quantitative analysis of percentage vessel area and total vessel length between the tissue chambers (n = 36 tissue chambers) in a single platform (n = 12 tissue units). (B) Quantitative analysis of the average percentage vessel area and total vessel length of each tissue unit on 2 independent platforms.

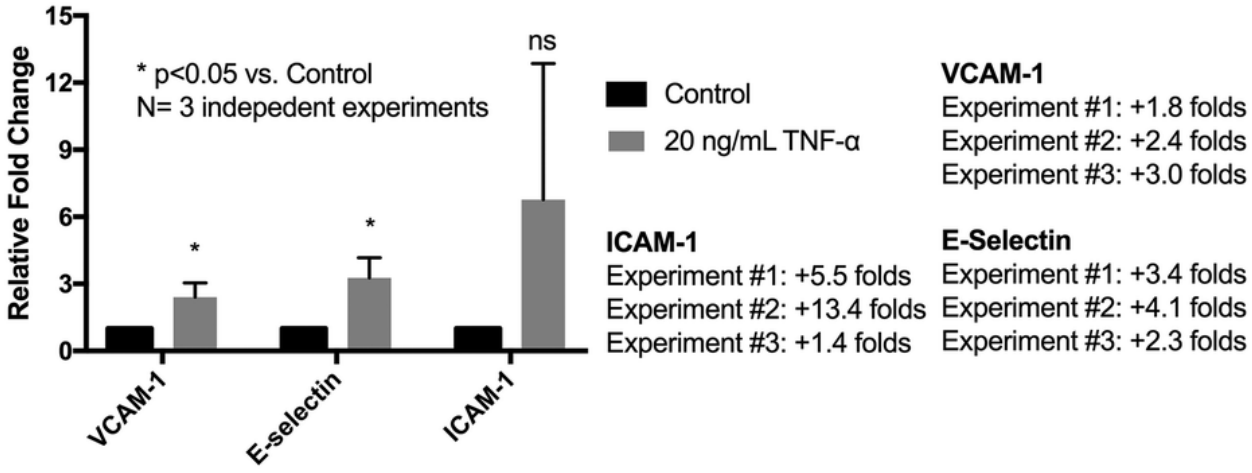

Figure 4.5: Gene expression analysis of VCAM-1, E-Selectin, and ICAM-1 in the platform. Tissue units were treated with TNF-α (20 ng mL^{-1}) for 24 hours and RNA was extracted for qRT-PCR analysis. Data represent mean values of 3 independent experiments ± SEM.

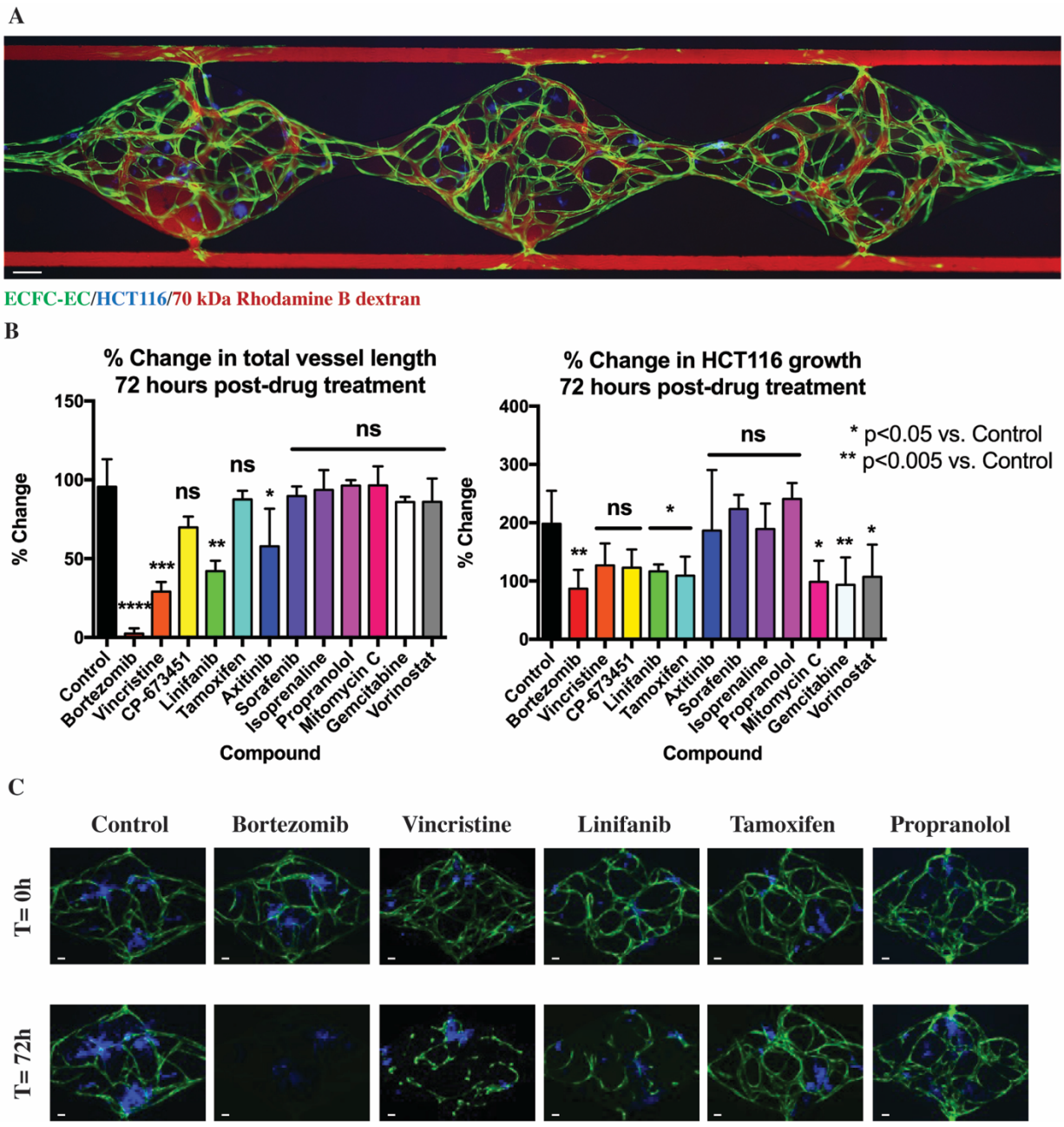

Figure 4.6: VMT in the platform and drug screening validation. (A) ECFC-EC (Venus) formed vascular networks inside the 3 tissue chambers around the HCT116 colorectal cancer cells (Azurite) on day 7. 70 kDa rhodamine B-dextran was introduced to the medium inlet and allowed to perfuse through the vasculature for 30 minutes. Scale bar = 100 µm. (B) Primary drug screening was performed on VMTs after 7 days of culture. On day 7, 1 µM concentration of 12 compounds was added to the medium inlet and allowed to perfuse through the vasculature. Drug efficacy on tumor growth and the associated vasculature was quantified after 72 hours. Data are shown as mean ± standard deviation of 4 replicates per compound. (C) Representative images before (t = 0 h) and after (t = 72 h) of drug treatment. Scale bar = 50 µm.

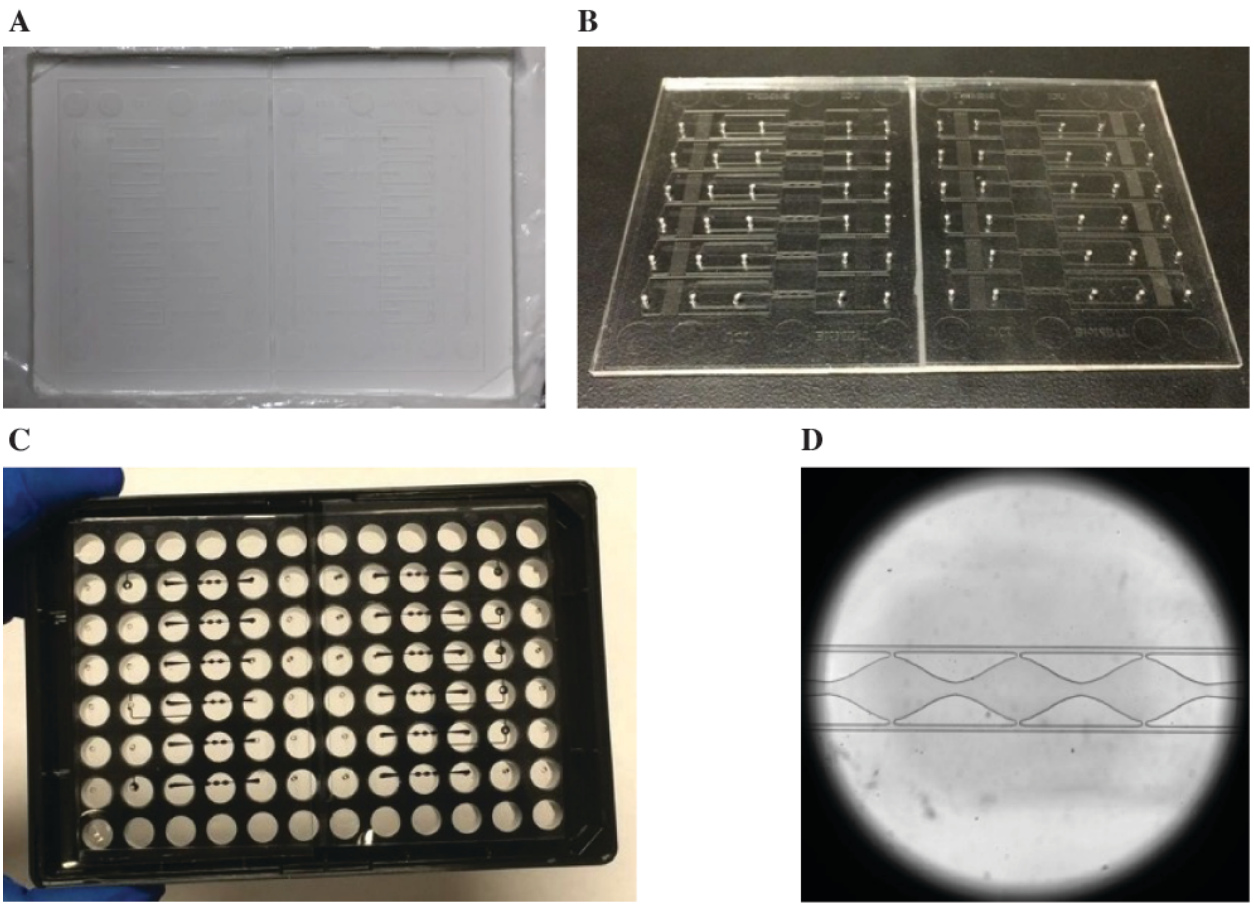

Figure 4.1S: Platform fabrication. (A) A customized master mold is fabricated using 2-part polyurethane liquid plastic and a micro-molding technique. (B) A PDMS device layer is replicated from the polyurethane master mold, and holes are punched for inlets and outlets. (C) A bottom view of a fully assembled platform. (D) A low-power view of 3 tissue chambers inside a single well.

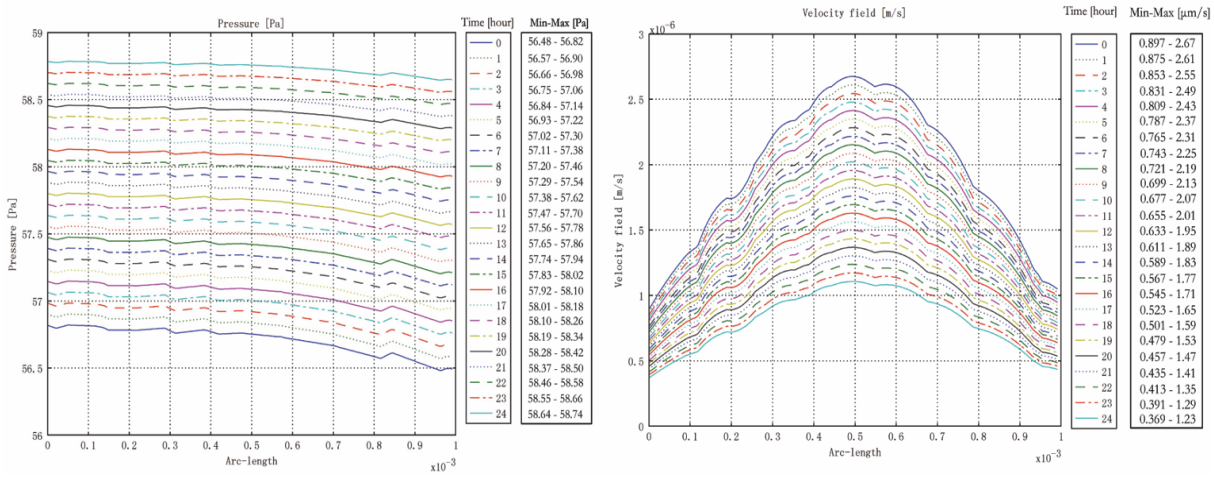

Figure 4.2S: Finite element simulation of hydrostatic pressure and interstitial velocity flow in horizontal direction of a tissue chamber.

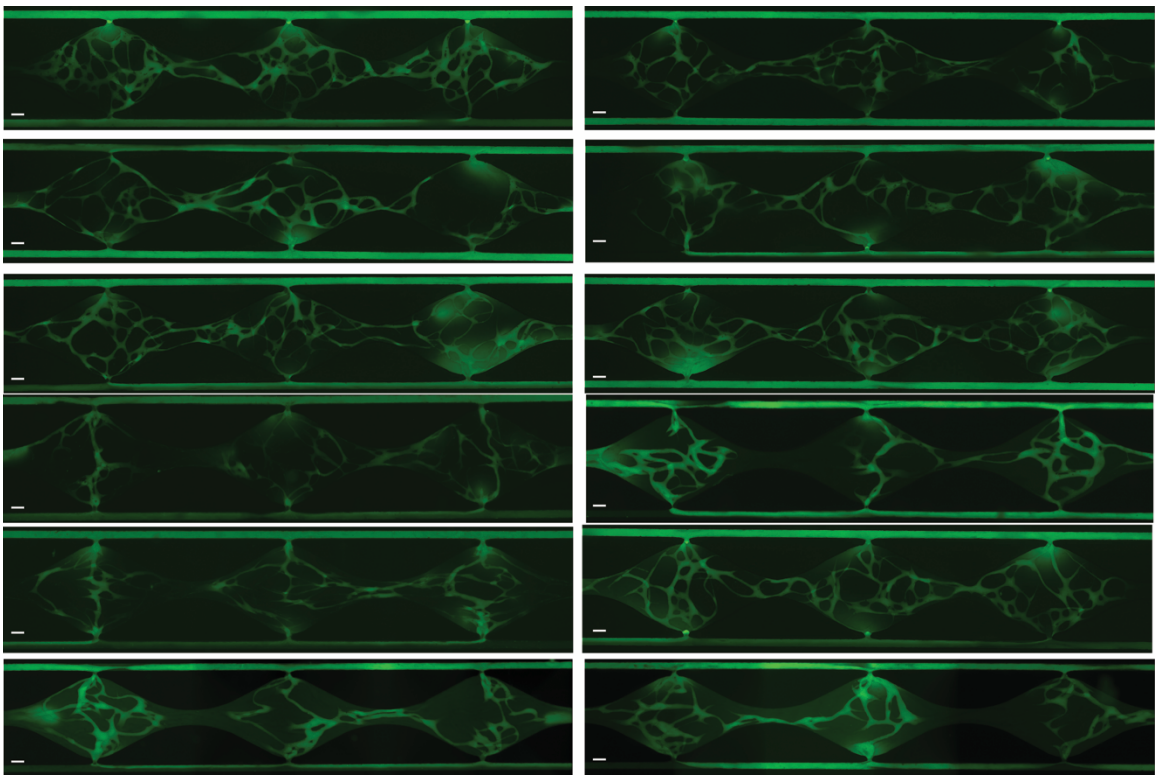

Figure 4.3S: 70 kDa-FITC dextran perfusion in 12 tissue units within a single platform. Scale bar = 100 μm.

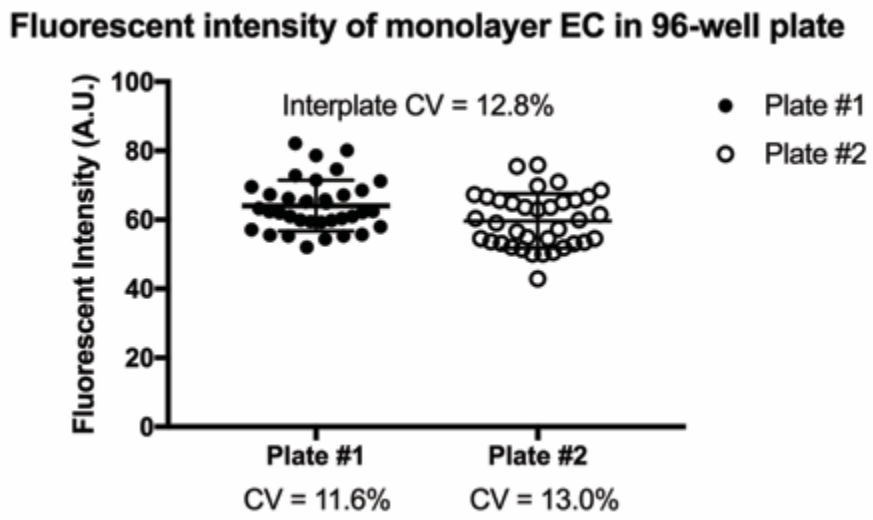

Figure 4.4S: Coefficient of variation (CV) of a standard 2D monoculture assay. Fluorescent-tagged endothelial cells were plated in 2 independent 96-well plates and allowed to adhere for 2 hours. Fluorescent intensity in each well was measured using a fluorescent plate reader and used to calculate the CV.

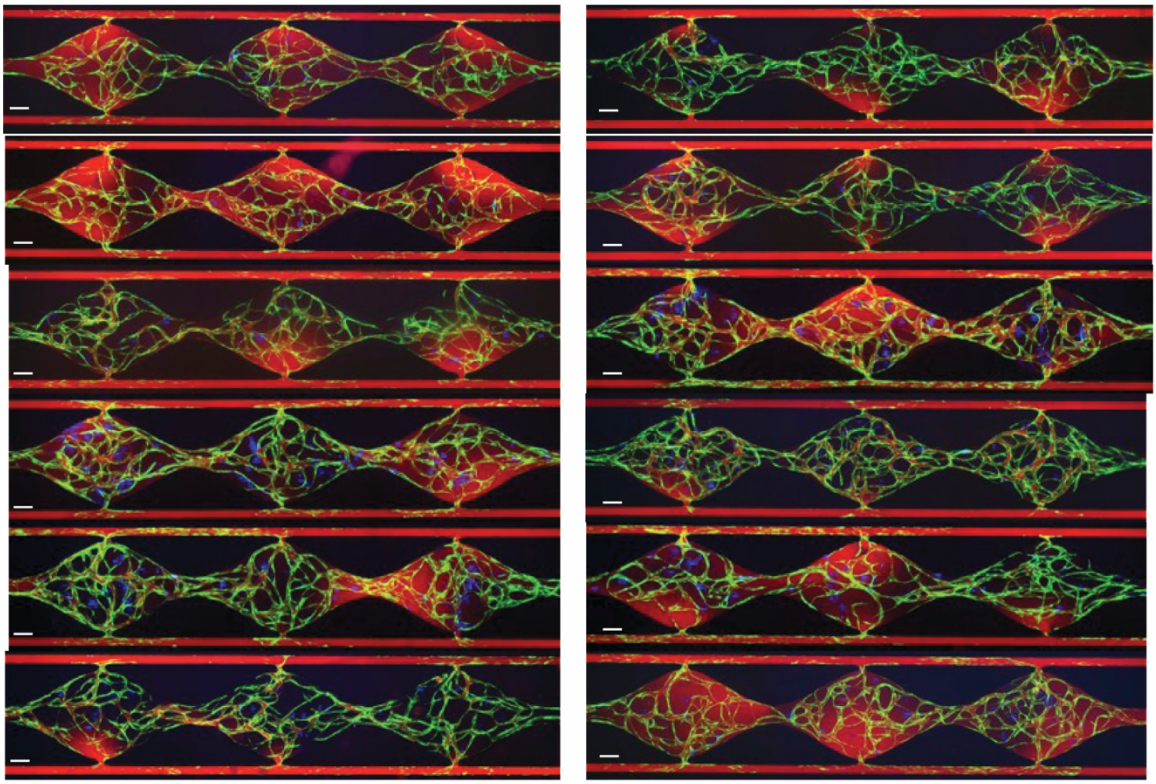

Figure 4.5S: 70 kDa-Rhodamine B dextran perfusion in 12 VMTs within a single platform. Scale bar = 100 μm.

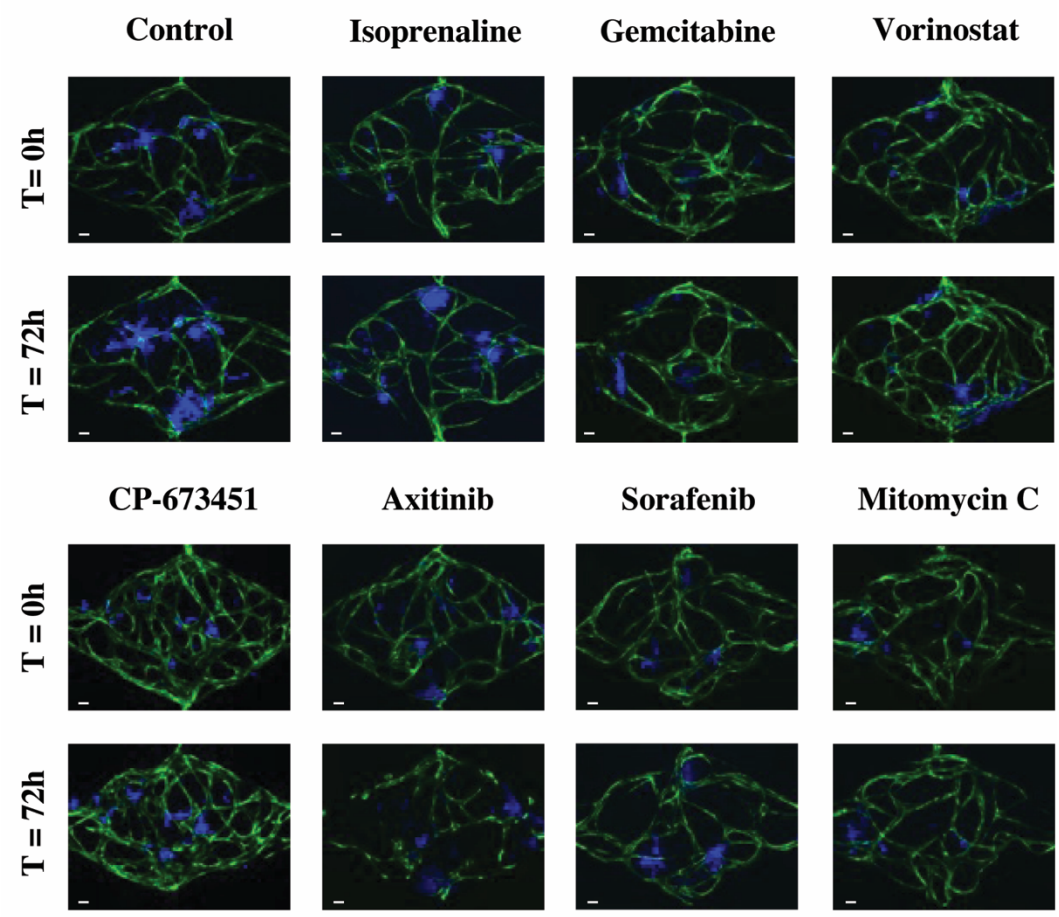

Figure 4.6S: Representative images before (T= 0h) and after (T= 72h) of drug treatment in the VMTs. Scale bar = 50 µm.

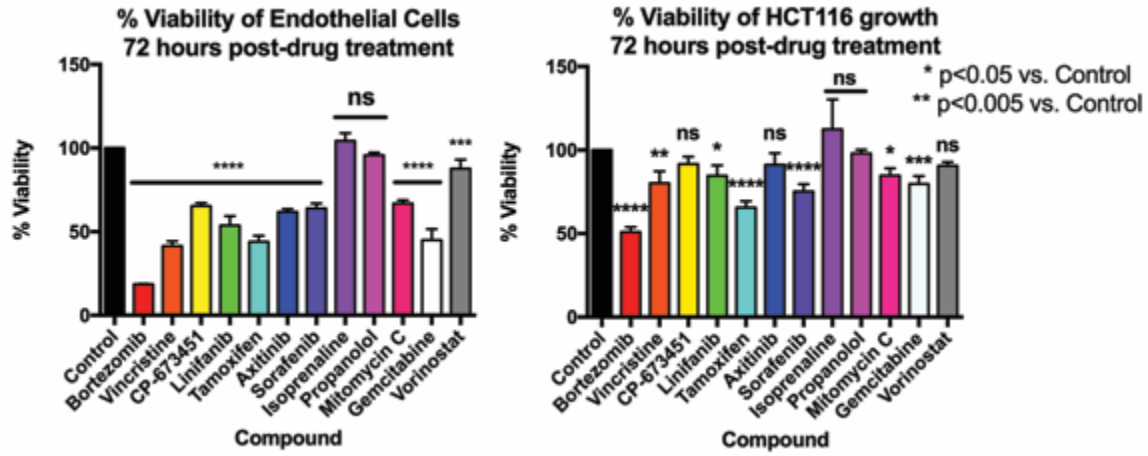

Figure 4.7S: Blinded, primary drug screening at 1 µM in 2D monoculture assay. Cell viability was quantified using XTT assay after 72 hours of drug treatment.

Table 4.1S: Sequence of qRT-PCR primers.

Gene Name	Sequence 5'→3'	
18S	CCCCGGCCGTCCCTCTTA	Forward
	CGCCCCCTCGATGCTCTTAG	Reverse
ICAM-1	CAGAGGTTGAACCCCCACAGT	Forward
	TCTGAGACCTCTGGCTTCGT	Reverse
E-selectin	CCGTCCGCCAGCCTCAGAAT	Forward
	TAGCCTCGCTCGGGGTTGGAC	Reverse
VCAM-1	CCATTTGACAGGCTGGAGAT	Forward
	TACTGTGGGCAGAGAATCCA	Reverse

Table 4.2S: Summary of drug compounds and their targets.

Compound	Target(s)
Bortezomib	20S Proteosome
Vincristine	Microtubule inhibitor
CP-673451	Multi-tyrosine kinase inhibitor (Concentration ≤1 μM: PDGFR-α/β, c-Kit, VEGFR1/2)
Linifanib	Potent ATP-competitive VGEFR/PDGFR inhibitor
Tamoxifen	Estrogen receptor antagonist
Axitinib	Multi-tyrosine kinase inhibitor (Concentration ≤1 μM: VEGFR1/2/3, PDGFR-α/β)
Sorafenib	Multi-tyrosine kinase inhibitor (Concentration ≤1 μM: VEGFR2, Raf, PDGFR-β, c-Kit, FGFR1)
Isoprenaline	β-adrenergic receptor agonist
Propranolol	β-adrenergic receptor inhibitor
Mitomycin C	DNA synthesis inhibitor
Gemcitabine	DNA synthesis inhibitor
Vorinostat	HDAC inhibitor

Source: Selleck Chemicals.

SUPPLEMENTARY CHAPTER

Blood–brain barrier-on-a-chip: Microphysiological systems that capture the complexity of the blood–central nervous system interface

Duc T.T. Phan, R. Hugh F. Bender, Jillian W. Andrejecsk, Agua Sobrino, Stephanie J. Hachey, Steven C. George, and Christopher C.W. Hughes

Originally published in Experimental Biology and Medicine 2017, 242(17):1669-1678.

S1 Abstract

The blood–brain barrier is a dynamic and highly organized structure that strictly regulates the molecules allowed to cross the brain vasculature into the central nervous system. The blood–brain barrier pathology has been associated with a number of central nervous system diseases, including vascular malformations, stroke/vascular dementia, Alzheimer's disease, multiple sclerosis, and various neurological tumors including glioblastoma multiforme. There is a compelling need for representative models of this critical interface. Current research relies heavily on animal models (mostly mice) or on two-dimensional (2D) *in vitro* models, neither of which fully capture the complexities of the human blood–brain barrier. Physiological differences between humans and mice make translation to the clinic problematic, while monolayer cultures cannot capture the inherently three-dimensional (3D) nature of the blood–brain barrier, which includes close association of the abluminal side of the endothelium with astrocyte foot-processes and pericytes. Here we discuss the central nervous system diseases associated with blood–brain barrier pathology, recent advances in the development of novel 3D blood–brain barrier -on-a-chip systems that better mimic the physiological complexity and structure of human blood–brain barrier, and provide an outlook on how these blood–brain barrier-on-a-chip systems can be used for central nervous system disease modeling.

S2 Introduction

The blood-brain barrier (BBB) is a dynamic and highly organized structure that strictly regulates the passage of molecules from the brain vasculature into the central nervous system (CNS) and thereby functions as a critical defense system that protects the brain from toxins and infection. The barrier results from a combination of extensive tight and adherens junctions between cerebral endothelial cells (CECs), which dramatically reduce the rate of transcytosis relative to vessels outside of the CNS. Additionally, both pericytes (PCs) and astrocytes, located on the abluminal side of the endothelium, provide critical support for this barrier. Dysfunction of the BBB is associated with a number of CNS diseases, including vascular malformations, stroke/vascular dementia, Alzheimer's disease, multiple sclerosis, and various neurological tumors including glioblastoma multiforme, and thus understanding this critical interface will be crucial in combating these pathologies. While current research relies heavily on rodent models and two-dimensional (2D) *in vitro* systems, neither can fully recapitulate the complexities of the human BBB. The three-dimensional (3D) nature of microvasculature and its association with PCs and astrocytes precludes the use of 2D model systems, and physiological differences between humans and mice, such as species differences in the P-glycoprotein (P-gp) transport of drug molecules across the BBB, make translation of mouse studies to the clinic problematic [1] . In this review, we discuss CNS diseases associated with BBB pathology, recent advances in the development of novel 3D BBB-on-a-chip systems that better mimic the physiological complexity and structure of human BBB, and provide an outlook on how these BBB-on-a-chip systems can be used for CNS disease modeling.

S3 Structure and function of the BBB

The BBB is a complex, dynamic, and highly organized structure consisting of four specialized components that together form the neurovascular unit (NVU). These components include: 1) specialized CECs that form the microvascular network; 2) a basal lamina that supports the abluminal surface of the endothelium; 3) PCs that wrap around these vessels; and 4) astrocyte end feet that extend to the CECs (Figure S1a) [2]. The anatomical structure and functions of this neurovascular unit have been reviewed extensively elsewhere [3]; therefore, for the purpose of this review, we only highlight the key BBB features that are relevant for the specific pathologies we discuss below.

Of the BBB components, the endothelium is the primary gatekeeper for ion exchange, transportation of neurotransmitters, essential water-soluble nutrients and metabolites, and the efflux of neurotoxins. This regulatory function relies on a combination of specific ion channels and active transporters expressed on the endothelial surface [3, 4]. At the cellular level, CECs express several proteins that contribute to adherens junctions (AJ) and tight junctions (TJ) at the interface between neighboring CECs (Figure S1b). These junctions function to significantly reduce paracellular diffusion of macromolecules from the blood plasma to the brain parenchymal region. AJs, consisting of cadherins that are associated with cytoplasmic scaffolding proteins such as alpha, beta, and gamma catenin, function to hold neighboring cells together while also providing structural support [5]. TJs on the other hand consist of occludin and claudin family proteins that are linked to numerous cytoplasmic scaffolding proteins, including ZO-1, ZO-2, and ZO-3, and act to tighten the contact surface between neighboring cells [6]. While occludin is considered a major component of TJs, particularly those found on CECs, evidence has shown that a functional BBB can still form in occludin-deficient mice [7]. This suggests that other

proteins enriched in BBB TJs, such as marveld2, cingulin-like-1, and pard3, perform redundantly to maintain BBB barrier function even in the absence of occludin [8].

While some lipid-soluble molecules are able to cross the BBB by passive diffusion, non-lipid-soluble molecules require active transport by transporter proteins on both the luminal and abluminal surfaces of the endothelium. These transporters are classified into two main families: soluble carriers (SLC), which transport a variety of organic molecules and inorganic ions according to their affinities with a specific transporter, and ATP-binding cassette (ABC) transporters, which actively transport a variety of substrates such as biosynthetic precursors, vitamins, and metabolites using an ATP-dependent process (Figure S1b) [3]. The specificity of these transporter families has important implications for both BBB pathology and the development of pharmacologic agents capable of crossing the BBB. For example, the SLC transporter GLUT1 normally functions as the primary BBB glucose transporter, yet mutations in this transporter are known to contribute to pathophysiological disorders such as Alzheimer's disease (AD), epilepsy, ischemia, and traumatic brain injury [9]. On the other hand, ABC transporters such as ABCB1 (P-gp), ABCG2 (BCRP), and the ABCC subfamily (ABCC1, ABCC2, and ABCC4), which normally serve as efflux pumps to remove toxins from the brain, pose challenges to drug delivery to the CNS. Many useful, lipid-soluble drugs that theoretically can cross the BBB according to their partition coefficient are unintentional substrates for these efflux transporters, thus preventing their accumulation in brain tissue [10].

In addition to the SLC and ABC transporters, molecules can be transported across the BBB through endothelial transcytosis. A unique feature of CECs compared to other types of endothelial cells (EC) in the body is that they have a one to two log lower level of transcytosis

[11], thus further increasing the selectivity of the BBB [12]. Endothelial transcytosis can be receptor-mediated for ligands such as transferrin and insulin, or caveolae-mediated for low-density proteins (LDL), all of which are important for CNS activities [13].

The basal lamina surrounding the abluminal side of CECs consists of proteoglycans and basement membrane proteins such as fibronectin, laminin, and collagen IV, all of which contribute to selective filtering of microparticles [14, 15]. Disruption of the basal lamina, and subsequent BBB disruption, is implicated in several pathological conditions, such as Alzheimer's disease (AD), multiple sclerosis (MS) and stroke, and is a major step in facilitating tissue inflammation [16]. Sharing the basal lamina with the CECs are the PCs. These cells wrap around the microvessels and play various roles at the BBB. They have been shown to regulate both BBB-specific gene expression patterns in EC, and endothelial transcytosis, and also induce polarization of astrocyte end-feet surrounding the CNS blood vessels [17]. Astrocytes are involved in various processes in the brain, such as regulating ion and water concentration, facilitating neurotransmitter clearance, and matching oxygen and glucose transportation to neuronal activity [18]. Although the role of astrocytes in regulating the BBB is still not fully understood, several *in vitro* studies have shown that they can induce barrier properties in cerebral and other types of EC [19]. In addition, recent findings have shown that astrocytes release nitric oxide, arachidonic acid, and prostaglandins, all of which can regulate vessel diameter to control blood flow [20].

Together, CECs, the basal lamina, PCs, and astrocytes cooperate to form a selectively permeable barrier that actively regulates the type and quantity of molecules that traffic from the blood into the CNS. While each component is critical to normal BBB function, defects in

individual components can lead to BBB dysfunction, enhanced permeability, and subsequent CNS disease.

S4 The role of BBB dysfunction in CNS diseases

Vascular malformations

Disruption in the normal flow of blood to the brain, either by malfunctioning capillaries or hemorrhaging vessels, can have devastating effects, including mental deficits, epileptic fits, headaches, balance deficits, and psychiatric disorders [21]. There are a number of vascular malformations that can cause such disruptions, including cerebral cavernous malformations (CCMs) [22] and arteriovenous malformations (AVMs). CCMs form as the result of mutations in the CCM1, 2 or 3 genes, and are composed of tight clusters of small, thin-walled capillaries that often support only minimal blood flow, and in the case of CCM2, have a disrupted BBB [23]. AVMs are lesions in which blood flows directly from arteries/arterioles to veins/venules, thereby bypassing downstream capillary beds. While these lesions can occur in other tissues, AVMs in the brain cause particularly severe symptoms, likely as a result of the reduced oxygen that results from the lack of a capillary bed between the oxygenated arterial blood and the venous return. AVMs are often congenital and are a major component of several hereditary disorders, including hereditary hemorrhagic telangiectasia (HHT, also known as Osler–Weber–Rendu disease), Wyburn–Mason syndrome, and Sturge–Weber syndrome [24]. While mutations in several genes have been identified to cause these diseases, specific pathological mechanisms are still unknown. In HHT, for example, which is an autosomal dominant disease, mutations of endoglin (ENG) or Alk1 (ACVRL1) are responsible for the majority of cases, but the location of developing lesions remains unpredictable [25 – 27]. Several contributing factors may determine where these lesions form, including: local trauma, such as a wound, that triggers angiogenesis [26, 28], alterations of blood flow [29], or altered mural cell recruitment and deficient interactions with the endothelium [30]. This final hypothesis is of particular interest in the context of the BBB, as disruption of

pericyte function may also lead to breakdown of the BBB. Accurately evaluating the role of BBB dysfunction in AVM formation will require a platform that faithfully recreates the intricate structure of brain microvasculature and surrounding BBB components. Such a platform must recapitulate the endogenous branching of native vasculature as this is an essential component of AVM lesions. BBB-on-a-chip technologies that allow for physiologic vascular network formation will provide a novel approach for studying the pathogenesis of cerebral vascular malformations.

Alzheimer's disease

Growing evidence suggests that BBB dysfunction is a major contributor in disorders of cognitive decline in the CNS. In one such disorder, Alzheimer's disease (AD), a major driver of pathology, is the accumulation of amyloid-β (Aβ) peptide in the form of amyloid plaques in the brain [31]. Transportation of Aβ across the BBB plays a crucial role in determining peptide concentration in the CNS, and its pathological consequence in AD [32]. In individuals affected by AD, BBB dysfunction has been correlated with pathological progression, as measured by decreased tight junction protein expression, thickening basal lamina, and increased vascular permeability [33]. With the failure of several large drug trials designed to lower the Aβ load in the brain of AD patients, efforts have focused on developing therapies around other AD-associated defects, such as vascular dysfunction. In recent years, a "two-hit" vascular hypothesis has been proposed, in which a pre-existing, non-AD related disease causes vascular dysfunction and subsequently accelerates the development of AD [34]. Metabolic disorders such as type 2 diabetes (T2D) and the related hyperglycemic condition are linked to vascular abnormality and hyperpermeability [35]. T2D is now considered an additional risk factor for AD progression in

addition to aging [36]. Longitudinal studies have shown that T2D patients have an increased risk of Alzheimer's disease by 50–100% [37]. Thus, it is hypothesized that T2D is the first hit that causes vascular malfunctions, leading to an imbalance in amyloid transportation across the BBB and an acceleration of AD development. A BBB-on-a-chip model would be an ideal platform for investigating BBB transport of Aβ and the potential role of hyperglycemia in driving disease progression.

Stroke & vascular dementia

Microvessel BBB dysfunction is also considered a contributing factor in ischemic stroke and non-Alzheimer's cognitive decline (vascular dementia). Nevertheless, how BBB dysfunction leads to the onset of these diseases has yet to be fully elucidated. While ischemic stroke is most commonly attributed to decreased blood flow due to vessel blockage in the brain, recent theories suggest that BBB permeability and microbleeds in the brain may significantly contribute to disease pathology [38]. Magnetic resonance imaging (MRI) of individuals who have suffered lacunar stroke (25% of all ischemic stroke individuals) reveals accumulation of the contrast agent gadolinium in brain white matter, indicating BBB permeability at these sites [39]. A detailed evaluation across 31 clinical studies indicates that BBB permeability increases not only with age, but is also higher in individuals with dementia [40]. BBB permeability appears especially important in vascular dementia, as these individuals have higher vascular leak compared to individuals with AD. While these studies demonstrate a strong correlation between BBB damage and disease onset, they cannot determine whether BBB dysfunction is a primary cause or a consequence of stroke and vascular dementia. This question has been partially addressed using a spontaneous hypertensive stroke-prone rat (SHRSP) model where sequential

MRIs have revealed that BBB permeability precedes immune infiltration at specific foci in the brain [41]. While the SHRSP rat model recapitulates human small vessel pathology quite well, there is still a critical need in the stroke field to develop better tools to model changes in microvasculature relevant to stroke pathology. BBB-on-a-chip models offer tremendous potential for recreating microvasculature in the laboratory that will allow controlled study of the mechanics of BBB permeability and immune infiltration as they relate to the process of stroke.

Multiple sclerosis

In healthy individuals, oligodendrocytes generate a myelin sheath that insulates CNS neuronal axons and facilitates signal propagation to neighboring neurons. However, in the neuroinflammatory disease multiple sclerosis (MS), these myelin sheaths are degraded by activated immune cells, leading to damage and death of the underlying neurons. While the exact mechanisms of MS remain unclear, one leading hypothesis suggests that CEC dysfunction and breakdown of the BBB are critical steps to the pathogenesis of this disease. Indeed, inflammation and blood vessel damage are evident at both active and chronic MS lesion sites in brain white matter when compared to healthy individuals [42, 43]. More specifically, recent evidence suggests that localized BBB breakdown is the result of several processes, including: (1) increased inflammation and activation of CECs; (2) decreased expression of CEC junction proteins; and (3) increased adhesion and extravasation of T cells. Elevated levels of the proinflammatory cytokines interferon-γ and TNF-α have been observed in individuals with MS and are thought to function in activating CECs [44]. Subsequent *in vitro* studies demonstrated that the presence of these cytokines, or whole serum from MS patients, can trigger breakdown of the BBB by downregulating the key junctional proteins occludin, VE-cadherin, and ZO-1 [42,

45]. The loss of these junction proteins compromises the integrity of the BBB and allows T cells to cross the endothelium. Despite evidence supporting this model of MS pathogenesis, controversy remains regarding the role of proinflammatory cytokines [46, 47] and the requirement of selectins for T cell extravasation [48, 49]. Significant clarity on MS pathogenesis is likely to be gained through human-specific, tissue-on-a-chip platforms that more accurately model MS when compared to existing experimental autoimmune encephalomyelitis (EAE) mouse models, which are the current standard for MS studies [50].

Glioblastoma

Glioblastoma multiforme (GBM) is a high-grade brain tumor arising from astrocytes. The high growth rate and relative insensitivity of these tumors to pharmacologic agents contribute to an especially poor prognosis for individuals with GBM [51]. The inability of these agents to significantly affect GBM growth is largely due to their limited transport across the BBB. Paradoxically, high-grade GBM are characterized by major alterations to normal vascular function, including down-regulation of key TJ proteins and increased BBB permeability [51-54]. Nevertheless, local disruption within the tumor vasculature is not sufficient to allow drug penetration in relevant quantities to effectively target GBM growth [54]. Moreover, cell migration may be increased across a newly permeable BBB, thereby facilitating the development of brain metastases [55]. The mechanisms underlying the inability of pharmacologic agents to cross the BBB have yet to be fully elucidated, but one possibility is altered expression of junction proteins. Recent work shows that the CEC receptor molecule Roundabout 4 (Robo4) is upregulated in an *in vitro* BBB model of GBM, resulting in a less permeable BBB [56]. In this same model, genetic deletion of Robo4 increased BBB permeability by down-regulation of the

key TJ proteins ZO-1, occludin-1 and claudin-5. These results suggest that despite overall increased BBB permeability in GBM, Robo4 may maintain relative impermeability of the BBB against anti-tumor therapeutic agents [57]. Additionally, the affinity of some anti-tumor drugs for the ABC efflux transporter proteins likely prevents their accumulation in GBM tumors [57]. The importance of tumor vasculature in providing nutrients to growing tumor cells has spurred efforts to develop anti-angiogenic therapies targeting GBM [58]. However, new data suggest that these therapies may not prolong overall patient survival when added to the standard of care [59]. Indeed, an anti-angiogenic regimen may impair the efficacy of chemotherapy in the GBM by compromising intratumoral delivery of these agents [60]. Although existing organ-on-a-chip platforms have sought to combine vasculature and GBM tumor components [61], these platforms will be further enhanced by the addition of a functioning BBB.

S5 The current state of BBB organ-on-a-chip models

Currently, *in vivo* models (most frequently, mice) are considered the standard for studies on the BBB and related CNS diseases [62]. These models are especially conducive to multilevel evaluation of complex tissues while allowing for pharmacodynamic and pharmacokinetic evaluation of potential pharmacologic agents. While these models have contributed significantly to new discoveries of BBB mechanics, their utility is inherently limited by physiological differences between humans and rodents, which often impede reliable translation to the clinic.

Microphysiological systems (MPS) combine the advantages of *in vivo* and *in vitro* models of tissue and organs by using microfluidics technology to incorporate dynamic fluid flow within a 3D environment that better mimics native tissues [63, 64]. One unique feature of these organs-on-a-chip that extends far beyond 2D and animal models is the capability to recapitulate patient-specific pathology [64]. While animal models provide a platform for studying complex diseases beyond 2D systems, these same models fail to capture human inter-individual genetic differences that may contribute to disease. Therefore, future studies will require the use of advanced MPS approaches to better evaluate patient-specific disease etiologies, with the ultimate goal being the development of truly personalized therapies. To this end, several BBB-on-a-chip models have been developed within the past five years (Table S1) [65 – 74].

Overall, these BBB organ-on-a-chip models better recapitulate the physical structure and physiological complexity of the human BBB by incorporating a 3D environment and in some cases exposing the endothelium to physiological fluid flow. In particular, fluid flow and shear stress are critical contributors to EC structure and function related to vascular network formation

[75]. The barrier function of these models is broadly improved over traditional 2D Transwell assays, as assessed by dextran diffusion across the endothelium. While the utility of these models has been examined elsewhere [63, 76], there are several challenges with these systems that must be considered in the development of future platforms and for the adoption of organ-on-a-chip systems for BBB disease modeling.

First, the geometry and dimensions of the blood vessel compartment within these systems do not truly represent cerebral blood vessels *in vivo*. The blood vessel compartment in all but two models (Herland *et al.* and Kim *et al.*) has a square or rectangular cross section, in contrast to the circular cross section found in living blood vessels. Additionally, the dimensions of these vessels vary in diameter, from 100 μm up to millimeter sizes. For comparison, in the human brain, cerebral capillaries are 7–10 μm in diameter [77], while arterioles and venules are 50–100 μm in diameter [78]. This difference in geometry is important as it can alter the distribution of shear stress on the endothelial surface. While shear stress positively influences BBB functions, square or rectangular cross-section channels do not have uniform shear stress distribution compared to circular cross-section channels under steady laminar flow. This shear stress is particularly important in regulating two transcription factors Krueppel-like factor (KLF2 and KLF4) that suppress endothelial responses to inflammatory stimuli such as TNF-α to maintain a quiescent phenotype [79]. A non-uniform shear stress distribution could potentially affect how EC respond to inflammatory signals inside the channel.

Second, the models listed in Table 5.1 all consist of a single channel and more appropriately represent a single blood vessel rather than a network of interacting vasculature. As such, the BBB-on-a-chip models have been unable to recapitulate the hierarchical branching of *in vivo*

vasculature, which is a defining feature of microvascular networks. Further, branch points are often the foci where many defects originate, as these regions are exposed to the most turbulent flow. Thus, it is clear that while a single channel approach may prove useful in understanding basic blood vessel biology, these models cannot adequately reproduce and interrogate disease phenotypes inherent to more complex, hierarchical vascular networks.

Third, the anatomical structure of the human NVU is not truly represented in these models. The physical contacts and interactions between CECs, the basal lamina, PC, and astrocytes require a 3D environment and the absence of an intervening membrane such as that present in Transwells. Of all the models listed in Table 1, the closest to the anatomical structure of a human NVU *in vivo* is reported by Herland *et al*. However, even in this model, which does have direct contact between CEC and astrocytes unimpeded by an artificial membrane, all four components of the human NVU were not present together, there was no capillary network (see above), and the single vessel was considerably wider than normal brain capillaries.

Lastly, the most recent platforms demonstrate a trend away from rodent CECs towards more ambitious approaches that employ human CECs. While it remains a challenge to obtain human CECs and maintain their specific phenotypes *in vitro*, it is crucial to utilize human cell sources when possible. Transcriptional profiling of human CECs versus mouse CECs reveals differences in immune response genes, tight junction proteins, transporters, and cell surface receptors, all of which are important features of the BBB [80]. It is also notable that commercially available, immortalized human brain CEC lines perform inconsistently in these modeling systems and there are no specific lines which appear optimal for *in vitro* modeling [81]. In terms of a co-culture system, it has been demonstrated that the presence of PC and/or astrocytes enhances EC barrier

functions *in vitro* [82], and so it will be essential to incorporate these cells into BBB-on-a-chip models. Indeed, the majority of models discussed in this review incorporate PC and/or astrocytes in co-culture. However, not all models utilize a human cell source, nor do they capture the 3D structure of the neurovascular unit. Despite the anatomical deficiencies in many of these models, some useful outputs can be obtained. For example, transport characteristics of the barrier can be assessed quite easily with the use of fluorescent or radioactive tracers, although in most of these systems only blood-to-brain transport is readily measurable. Inflammatory responses of the endothelium can also be assessed, along with leukocyte adhesion, although as discussed above, the flow characteristics may be disrupted to the point where the endothelium is more sensitive to inflammatory stimuli than would be the case *in vivo*. Finally, in only a limited number of these models can the interactions between the EC and the pericytes and astrocytes be investigated, as in many cases an artificial membrane separates the cell types. There is clearly much still to be done in creating fully representational BBB models *in vitro*.

S6 Outlook

While efforts to develop more complex, sophisticated *in vitro* BBB-on-a-chip platforms have advanced significantly in recent years, challenges remain in utilizing these models to study CNS diseases.

As discussed above, animal cells are still widely used in BBB-on-a-chip platforms due to the limited availability of human tissues. While these models are useful for comparison to *in vivo* studies, there must also exist a 'gold standard' to benchmark for clinical translation [83, 84]. Although challenges remain in differentiation protocols, recent advances in deriving brain endothelium from human induced pluripotent stem cells (iPSCs) [83, 85] adds another to the list of brain cell types that can be used to create clinically relevant models for CNS disease. Particularly for complex CNS syndromes, it is crucial to investigate whether the pathology involves cell types other than those primarily thought to be involved, and these could include CEC. As previously discussed, perturbation of vascular integrity in the BBB has been implicated in diverse neurological disorders. To understand the role of the BBB in neurological diseases, it will be essential to develop a fully functional *in vitro* model that integrates multiple human cell types within a perfused vascular network and appropriate ECM. This prototypical BBB-on-a-chip will allow real-time study of events leading to neurovascular compromise, such as aberrant angiogenesis – often in the presence of a tumor, deregulated transport across the BBB, inflammation, and arterial dysfunction. It should also allow for meaningful screening of CNS-targeting drugs that must penetrate the BBB to enable effectiveness [84]. BBB-on-a-chip platforms that can incorporate patient-derived iPSC to model specific diseases, or patient-derived tumor tissue to model brain cancer, have the potential to lower many barriers to drug discovery.

Furthermore, BBB-on-a-chip platforms generated from iPSCs (or cancer cells) that are isolated from unique populations of patients can be studied to reveal patient-specific, gene–drug interactions based on differential treatment response. These adaptations may facilitate drug discovery targeted to specific genetic subgroups and inform patient stratification in clinical trial design.

In addition to cell sourcing, incorporation of other key components of the BBB such as PC, astrocytes, and a brain-like ECM environment should be considered for future *in vitro* model development. These components are often neglected, yet they are potentially as important as the EC in driving CNS pathological conditions *in vivo*. As such it will be critical to incorporate them into BBB-on-a-chip models.

Aside from platform development, new standardized criteria for quantitative evaluation of BBB functions are required. Traditionally, Transendothelial Electrical Resistance (TEER) and vascular permeability of molecules with different molecular weights have been used to assess the barrier properties in 2D Transwell assays. However, in new BBB-on-a-chip models, this may no longer prove to be a viable metric. As shown in Table 1, the majority of these models do not assess TEER due to challenges in probing electrical resistance inside complex microfluidic configurations. Other factors, such as the presence of co-cultured cells and ECM, the materials used for device fabrication, and ionic composition in cell culture medium could affect TEER measurements, hindering comparison between different BBBs-on-a-chip. Thus for future model development, TEER should not be considered as a major benchmark for barrier functions. Vascular permeability, on the other hand, is more useful and relevant to evaluate vascular integrity relevant to BBB function. In general, if the permeability of reference molecules

measured in the BBB-on-a-chip model is close to physiological levels, the model can be considered to mimic the BBB *in vivo*, at least for transport studies. Fluorescently tagged 70 kDa dextran is routinely used as a reference to determine vascular permeability, partially due to its close molecular weight to albumin (MW = 68 kDa), a major protein present in the bloodstream. Under physiologic conditions, little to no albumin can cross the BBB *in vivo*, thus vascular permeability of 70 kDa dextran in BBB-on-a-chip models should be minimal, and can be considered a benchmark to evaluate BBB properties within the platform. Nevertheless, several factors need to be considered when comparing vascular permeability in these models relative to *in vivo* results. For instance, the dextran concentration, the flow rate, and the pressure difference between compartments (or inside and outside of the vascular channel) could affect permeability measurements. While there is no perfect *in vitro* model that can reflect all aspects of the BBB *in vivo*, it is critical to understand the limitations and caveats of each modeling platform. Thus, standardization for measuring vascular permeability is required, and the permeability coefficient should be reported with specific parameters related to that measurement such as flow rate, dextran concentrations, and exposure duration.

Over the past five years, we have significantly improved the methodology to generate perfused human microvascular networks in our organ-on-a-chip system [86, 87]. In addition, we have demonstrated that this system can be adapted to model the tumor microenvironment *in vitro* for therapeutic screening [88]. These results are important milestones in our platform development effort, providing an opportunity to adapt the system for different organ-specific applications. With a vision to create an *in vitro* BBB model to study CNS diseases, we have been developing a BBB-on-a-chip that incorporates perfused human blood vessels, a brain-like ECM environment, PC and astrocytes. As a proof-of-concept, we have

cultured human endothelial colony forming cell-endothelial cells (ECFC-EC), PC enriched from human stroma, and astrocytes derived from human neural stem cells in an ECM consisting of several basement membrane and interstitial structural proteins (Figure 5.2). We observed multicellular interactions between PC, astrocytes and the microvasculature. Furthermore, we found that the presence of astrocytes increases expression of several key adherens and tight junction genes, such as VE-Cadherin and Claudin-5. We are currently exploring the use of iPSC-derived EC, along with strategies to induce a brain-type phenotype, with the goal of enhancing barrier functions in our system. Current limitations of the system include: problems sourcing low passage human brain EC, which likely will prove essential for generating the correct pericyte-EC and astrocyte-EC interactions; maintaining the correct extracellular environment, which will likely need to be bathed in a CSF-like medium; and modeling the BBB in different parts of the brain, as there is a growing awareness that astrocytes differ in different regions and the BBB may have differential selectivity in some (possibly congruent) regions. In summary, by combining the permeability assays, non-invasive optical imaging of metabolism [89], and incorporation of multiple cell types (including glioma cells), we believe this system will provide unprecedented insights into the functions of the BBB in health and disease.

S7 Contribution

DTTP and RHFB wrote and edited the manuscript. DTTP prepared the table and figures. DTTP, RHFB, JWA, AG, and SJH contributed knowledge and wrote the disease section. DTTP contributed know- ledge and wrote the current state of BBB organ-on-a-chip model and outlook section. SJH contributed knowledge and wrote the outlook section. SCG and CCWH conceived the idea, wrote, and edited the manuscript. All authors read and approved the manuscript.

S8 Acknowledgements

This work was supported by the following grants: UH3 TR000481 (SCG) and R01 PQD5-CA180122 (CCWH).

S9 Conflict of interests

Christopher CW Hughes and Steven C George are founders of 4Design Biosciences, LLC and Kino Biosciences Inc., which have been established to commercialize the microfluidic platform mentioned in the text.

S10 References

1. Suzuyama N, Katoh M, Takeuchi T, Yoshitomi S, Higuchi T, Asashi S, Yokoi T. Species differences of inhibitory effects on P-glycoprotein-mediated drug transport. J Pharm Sci. 2007;96(6):1609-18.
2. Hawkins B, Davis T. The blood-brain barrier/neurovascular unit in health and disease. Pharmacol Rev. 2005;57(2):173-85.
3. Cardoso F, Brites D, Brito M. Looking at the blood-brain barrier: molecular anatomy and possible investigation approaches. Brain Res Rev. 2010;64(2):328-63.
4. Abbott N, Patabendige A, Dolman D, Yusof S, Begley D. Structure and function of the blood-brain barrier. Neurobiol Dis. 2010;37(1):13-25.
5. Wolburg H, Noell S, Mack A, Wolburg-Buchholz K, Fallier-Becker P. Brain endothelial cells and the glio-vascular complex. Cell Tissue Res. 2009;335(1):75-96.
6. Wolburg H, Lippoldt A. Tight junctions of the blood-brain barrier: development, composition and regulation. Vascul Pharmacol. 2002;38(6):323-37.
7. Saitou M, Furuse M, Sasaki H, Schulzke J, Fromm M, Takano H, Noda T, Tsukita S. Complex phenotype of mice lacking occludin, a component of tight junction strands. Mol Biol Cell. 2000;11:4131–42.
8. Daneman R, Zhou L, Agalliu D, Cahoy J, Kaushal A, Barres B. The mouse blood-brain barrier transcriptome: a new resource for understanding the development and function of brain endothelial cells. PLoS One. 2010;5(10).
9. Guo X, Geng M, Du G. Glucose transporter 1, distribution in the brain and in neural disorders: its relationship with transport of neuroactive drugs through the blood-brain barrier. Biochem Genet. 2005;43(3-4):175-87.
10. Löscher W, Potschka H. Blood-brain barrier active efflux transporters: ATP-binding cassette gene family. NeuroRx. 2005;2(1):86-98.
11. De Bock M, Van Haver V, Vandenbroucke R, Decrock E, Wang N, Leybaert L. Into rather unexplored terrain-transcellular transport across the blood-brain barrier. Glia. 2016;64(7):1097-123.
12. Stamatovic S, Keep R, Andjelkovic A. Brain endothelial cell-cell junctions: how to "open" the blood brain barrier. Curr Neuropharmacol. 2008;6(3):179-92.
13. Georgieva J, Hoekstra D, Zuhorn I. Smuggling Drugs into the Brain: An Overview of Ligands Targeting Transcytosis for Drug Delivery across the Blood-Brain Barrier. Pharmaceutics. 2014;6(4):557-83.
14. Kanwar Y, Linker A, Farquhar M. Increased permeability of the glomerular basement membrane to ferritin after removal of glycosaminoglycans (heparan sulfate) by enzyme digestion. J Cell Biol. 1980;86:688–93.
15. Lieleg O, Baumgärtel R, Bausch A. Selective filtering of particles by the extracellular matrix: an electrostatic bandpass. 97. 2009;6(1569-77).
16. Zlokovic B. The blood-brain barrier in health and chronic neurodegenerative disorders. Neuron. 2008;57(2):178-201.
17. Armulik A, Genové G, Mäe M, Nisancioglu M, Wallgard E, Niaudet C, He L, Norlin J, Linblom P, Strittmatter K, Johansson B, Betscholtz C. Pericytes regulate the blood-brain barrier. Nature. 2010;468(7323):557–61.
18. Sofroniew M, Vinters H. Astrocytes: biology and pathology. Acta Neuropathol. 2010;119(1):7-35.

19. Abbott N, Rönnbäck L, Hansson E. Astrocyte-endothelial interactions at the blood-brain barrier. Nat Rev Neurosci. 2006;7(1):41-53.
20. Gordon G, Mulligan S, MacVicar B. Astrocyte control of the cerebrovasculature. Glia. 2007;55(12):1214-21.
21. Ajiboye N, Chalouhi N, Starke R, Zanaty M, Bell R. Cerebral arteriovenous malformations: evaluation and management. Sci World J. 2014;2014:1-6.
22. Gross B, Du R. Cerebral cavernous malformations: natural history and clinical management. Expert Rev Neurother. 2015;15(7):771-7.
23. Choquet H, Pawlikowska L, Lawton M, Kim H. Genetics of cerebral cavernous malformations: current status and future prospects. J Neurosurg Sci. 2015;59(3):211-20.
24. Thomas J, Surendran S, Abraham M, Rajavelu A, Kartha C. Genetic and epigenetic mechanisms in the development of arteriovenous malformations in the brain. Clinical Epigenetics. 2016;8:78.
25. Peacock H, Caolo V, Jones E. Arterovenous malformations in hereditary haemorrhagic telangiectasia: looking beyond ALK1-NOTCH interactions. Cardiovascular Research. 2016;109:196-203.
26. Arthur H, Geisthoff U, Gossage J, Hughes C, Lacombe P, Meek M, Oh P, Roman R, Trerotola S, Velthuis S, Woodercak-Donahue W. Executive summary of the 11th HHT international scientific conference. Angiogenesis. 2015;18:511-24.
27. Sam C, Li F, Liu S. Inherited neurovascular diseases affecting cerebral blood vessels and smooth muscle. Metab Brain Dis. 2015;30:1105-16.
28. Choi E, Kim Y, Choe S, Tak Y, Garrido-Martin E, Chang M, Lee Y, Oh P. Enhanced responses to angiogenic cues underlie the pathogenesis of hereditary hemorrhagic telangiectasia 2. PLoS One. 2013;8(5).
29. Corti P, Young S, Chen C, Patrick M, Rochon E, Pekkan K, Roman B. Interaction between alk1 and blood flow in the development of arteriovenous malformations. Development. 2011;238(8):1573-82.
30. Shovlin C. Hereditary haemorrhagic telangiectasia: pathology, diagnosis and treatment. Blood Reviews. 2010;24:203-19.
31. Wisniewski T, Ghiso J, Frangione B. Biology of A beta amyloid in Alzheimer's disease. Neurobiol Dis. 1997;4(5):313-28.
32. Zlokovic B, Ghiso J, Mackic J, McComb J, Weiss M, Frangione B. Blood-brain barrier transport of circulating Alzheimer's amyloid beta. Biochem Biophys Res Commun. 1993;197(3):1034-40.
33. Kelleher R, Soiza R. Evidence of endothelial dysfunction in the development of Alzheimer's disease: Is Alzheimer's a vascular disorder? Am J Cardiovasc Dis. 2013;3(4):197-226.
34. Zlokovic B. Neurovascular pathways to neurodegeneration in Alzheimer's disease and other disorders Nat Rev Neurosci. 2011;12(12):723-38.
35. Scalia R, Gong Y, Berzins B, Zhao L, Sharma K. Hyperglycemia is a major determinant of albumin permeability in diabetic microcirculation: the role of mu-calpain. Diabetes. 2007;56(7):1842-9.
36. Carlsson C. Type 2 diabetes mellitus, dyslipidemia, and Alzheimer's disease. J Alzheimers Dis. 2010;20(3):711-22.
37. Biessels G, Staekenborg S, Brunner E, Brayne C, Scheltens P. Risk of dementia in diabetes mellitus: a systematic review. Lancet. 2006;5(1):64-74.

38. Wardlaw J, Sandercock P, Dennis M, Starr J. Is breakdown of the blood-brain barrier responsible for lacunar stroke, leukoaraiosis, and dementia? Stroke. 2003;34(3):806-12.
39. Wardlaw J, Doubal F, Armitage P, Chappell F, Carpenter T, Muñoz Maniega S, Farrall A, Sudlow C, Dennis M, Dhillon B. Lacunar stroke is associated with diffuse blood-brain barrier dysfunction. Ann Neurol. 2009;65(2):194-202.
40. Farrall A, Wardlaw J. Blood-brain barrier: ageing and microvascular disease--systematic review and meta-analysis. Neurobiol Aging. 2009;30:337-52.
41. Sironi L, Guerrini U, Tremoli E, Miller I, Gelosa P, Lascialfari A, Zucca I, Eberini I, Gemeiner M, Paoletti R, Gianazza E. Analysis of pathological events at the onset of brain damage in stroke-prone rats: a proteomics and magnetic resonance imaging approach. J Neurosci Res. 2004;78(1):115-22.
42. Kirk J, Plumb J, Mirakhur M, McQuaid S. Tight junctional abnormality in multiple sclerosis white matter affects all calibres of vessel and is associated with blood-brain barrier leakage and active demyelination. J Pathol. 2003;201(2):319-27.
43. Plumb J, McQuaid S, Mirakhur M, Kirk J. Abnormal endothelial tight junctions in active lesions and normal-appearing white matter in multiple sclerosis. Brain Pathol. 2002;12(2):154-69.
44. Hohnoki K, Inoue A, Koh CS. Elevated serum levels of IFN-gamma, IL-4 and TNF-alpha/unelevated serum levels of IL-10 in patients with demyelinating diseases during the acute stage. J Neuroimmunol. 1998;87(1-2):27-32.
45. Minagar A, Long A, Ma T, Jackson TH, Kelley RE, Ostanin DV, Sasaki M, Warren A, Jawahar A, Cappell B, Alexander J. Interferon (IFN)-beta 1a and IFN-beta 1b block IFN-gamma-induced disintegration of endothelial junction integrity and barrier. Endothelium. 2003;10(6):299-307.
46. Bahbouhi B, Berthelot L, Pettre S, Michel L, Wiertlewski S, Weksler B. Peripheral blood CD4+ T lymphocytes from multiple sclerosis patients are characterized by higher PSGL-1 expression and transmigration capacity across a human blood-brain barrier-derived endothelial cell line. J Leukoc Biol. 2009;86(5):1049-63.
47. Ottum PA, Arellano G, Reyes LI, Iruretagoyena M, Naves R. Opposing Roles of Interferon-Gamma on Cells of the Central Nervous System in Autoimmune Neuroinflammation. Front Immunol. 2015;6:539.
48. Doring A, Wild M, Vestweber D, Deutsch U, Engelhardt B. E- and P-selectin are not required for the development of experimental autoimmune encephalomyelitis in C57BL/6 and SJL mice. J Immunol. 2007;179(12):8470-9.
49. Engelhardt B. Immune cell entry into the central nervous system: involvement of adhesion molecules and chemokines. J Neurol Sci. 2008;274(1-2):23-6.
50. Croxford AL, Kurschus FC, Waisman A. Mouse models for multiple sclerosis: historical facts and future implications. Biochim Biophys Acta. 2011;1812(2):177-83.
51. Omuro A, DeAngelis L. Glioblastoma and other malignant gliomas: a clinical review. JAMA. 2013;310(17):1842-50.
52. Papadopoulos M, Saadoun S, Woodrow C, Davies D, Costa-Martins P, Moss R, Krishna S, Bell B. Occludin expression in microvessels of neoplastic and non-neoplastic human brain. Neuropathol Appl Neurobiol. 2001;27(5):384-95.
53. Liebner S, Fischmann A, Rascher G, Duffner F, Grote E, Kalbacher H, Wolburg H. Claudin-1 and claudin-5 expression and tight junction morphology are altered in blood vessels of human glioblastoma multiforme. Acta Neuropathol. 2000;100(3):323-31.

54. Dhermain F, Hau P, Lanfermann H, Jacobs A, van den Bent M. Advanced MRI and PET imaging for assessment of treatment response in patients
with gliomas. Lancet Neurol. 2010;9(9):906-20.
55. Jia W, Lu R, Martin T, Jiang W. The role of claudin-5 in blood-brain barrier (BBB) and brain metastases Mol Med Rep. 2014;9(3):779-85.
56. Cai H, Liu W, Xue Y, Shang X, Liu J, Li Z, Wang P, Liu L, Hu Y, Liu Y. Roundabout 4 regulates blood-tumor barrier permeability through the modulation of ZO-1, Occludin, and Claudin-5 expression. J Neuropathol Exp Neurol. 2015;74(1):25-37.
57. Régina A, Demeule M, Laplante A, Jodoin J, Dagenais C, Berthelet F, Moghrabi A, Béliveau R. Multidrug resistance in brain tumors: roles of the blood-brain barrier. Cancer Metastasis Rev. 2001;20(1-2):13-25.
58. Popescu A, Purcaru S, Alexandru O, Dricu A. New perspectives in glioblastoma antiangiogenic therapy. Contemp Oncol (Pozn). 2016;20(2):109-18.
59. Scribner E, Saut O, Province P, Bag A, Colin T, Fathallah-Shaykh H. Effects of anti-angiogenesis on glioblastoma growth and migration: model to
clinical predictions. PLoS One. 2014;9(12).
60. de Groot J, Reardon D, Batchelor T. Antiangiogenic therapy for glioblastoma: the challenge of translating response
rate into efficacy. Am Soc Clin Oncol Educ Book. 2013.
61. Rape A, Ananthanarayanan B, Kumar S. Engineering strategies to mimic the glioblastoma microenvironment. Adv Drug Deliv Rev. 2014:79-80.
62. Abbott N. Prediction of blood-brain barrier permeation in drug discovery from in vivo, in vitro and in silico models. Drug Discov Today Technol. 2004;1(4):407-16.
63. van der Helm M, van der Meer A, Eijkel J, van den Berg A, Segerink L. Microfluidic organ-on-chip technology for blood-brain barrier research. Tissue Barriers. 2016;4(1).
64. Bhatia S, Ingber D. Microfluidic organs-on-chips. Nat Biotechnol. 2014;32(8):760-72.
65. Wang Y, Abaci H, Shuler M. Microfluidic blood-brain barrier model provides in vivo-like barrier properties for drug permeability screening. Biotechnol Bioeng. 2016.
66. Herland A, van der Meer A, FitzGerald E, Park T, Sleeboom J, Ingber D. Distinct Contributions of Astrocytes and Pericytes to Neuroinflammation Identified in a 3D Human Blood-Brain Barrier on a Chip. PLoS One. 2016.
67. Brown J, Pensabene V, Markov D, Allwardt V, Neely M, Shi M, Britt C, Hoilett O, Yang Q, Brewer B, Samson P, McCawley L, May J, Webb D, Li D, Bowman A, Reiserer R, Wikswo J. Recreating blood-brain barrier physiology and structure on chip: A novel neurovascular microfluidic bioreactor. Biomicrofluidics. 2015;9(5).
68. Deosarkar S, Prabhakarpandian B, Wang B, Sheffield J, Krynska B, Kiani M. A Novel Dynamic Neonatal Blood-Brain Barrier on a Chip. PLoS One. 2015;10(11).
69. Sellgren K, Hawkins B, Grego S. An optically transparent membrane supports shear stress studies in a three-dimensional microfluidic neurovascular unit model. Biomicrofluidics. 2015;9(6).
70. Kim J, Kim H, Im S, Chung S, Kang J, Choi N. Collagen-based brain microvasculature model in vitro using three-dimensional printed template. Biomicrofluidics. 2015;9(2).
71. Prabhakarpandian B, Shen M, Nichols J, Mills I, Sidoryk-Wegrzynowicz M, Aschner M, Pant K. SyM-BBB: a microfluidic Blood Brain Barrier model. . Lab Chip. 2013;13(6):1093-101.
72. Achyuta A, Conway A, Crouse R, Bannister E, Lee R, Katnik C, Behensky A, Cuevas J, Sundaram S. A modular approach to create a neurovascular unit-on-a-chip. Lab Chip.

2013;13(4):542-53.
73. Griep L, Wolbers F, de Wagenaar B, ter Braak P, Weksler B, Romero I, Couraud P, Vermes I, van der Meer A, van den Berg A. BBB on chip: microfluidic platform to mechanically and biochemically modulate blood-brain barrier function. Biomed Microdevices. 2013;15(1):145-50.
74. Yeon J, Na D, Choi K, Ryu S, Choi C, Park J. Reliable permeability assay system in a microfluidic device mimicking cerebral vasculatures. Biomed Microdevices. 2012;14(6):1141-8.
75. Cucullo L, Hossain M, Puvenna V, Marchi N, Janigro D. The role of shear stress in Blood-Brain Barrier endothelial physiology. BMC Neurosci. 2011;12:40.
76. Wolff A, Antfolk M, Brodin B, Tenje M. In Vitro Blood-Brain Barrier Models-An Overview of Established Models and New Microfluidic Approaches. J Pharm Sci. 2015;104(9):2727-46.
77. Duvernoy H, Delon S, Vannson J. The vascularization of the human cerebellar cortex. Brain Res Bull. 1983;11(4):419-80.
78. Wiedeman M. Dimensions of blood vessels from distributing artery to collecting vein. Circ Res. 1963;12:375-8.
79. Atkins G, Jain M. Role of Krüppel-Like Transcription Factors in Endothelial Biology. Circ Res. 2007;100(12).
80. Urich E, Lazic S, Molnos J, Wells I, Freskgård P. Transcriptional profiling of human brain endothelial cells reveals key properties crucial for predictive in vitro blood-brain barrier models. PLoS One. 2012;7(5).
81. Rahman N, Rasil A, Meyding-Lamade U, Craemer E, Diah S, Tuah A, Muharram S. Immortalized endothelial cell lines for in vitro blood-brain barrier models: A systematic review. Brain Res 2016;1642:532-45.
82. Wang Y, Wang N, Cai B, Wang G, Li J, Piao X. In vitro model of the blood-brain barrier established by co-culture of primary cerebral microvascular endothelial and astrocyte cells. Neural Regen Res. 2015;10(12):2011-7.
83. Bellin M, Marchetto M, Gage F, Mummery C. Induced pluripotent stem cells: the new patient? Nat Rev Mol Cell Biol. 2012;13(11):713-26.
84. Pamies D, Hartung T, Hogberg H. Biological and medical applications of a brain-on-a-chip. Exp Biol Med (Maywood). 2014;239(9):1096-107.
85. Lippmann E, Azarin S, Kay J, Nessler R, Wilson H, Al-Ahmad A, Palecek S, Shusta E. Derivation of blood-brain barrier endothelial cells from human pluripotent stem cells. Nat Biotechnol. 2012;30(8):783-91.
86. Wang X, Phan D, Sobrino A, George S, Hughes C, Lee A. Engineering anastomosis between living capillary networks and endothelial cell-lined microfluidic channels. Lab Chip. 2016;16(2):282-90.
87. Wang X, Phan D, Zhao D, George S, Hughes C, Lee A. An on-chip microfluidic pressure regulator that facilitates reproducible loading of cells and hydrogels into microphysiological system platforms. Lab Chip. 2016;16(5):868-76.
88. Sobrino A, Phan D, Datta R, Wang X, Hachey S, Romero-López M, Gratton E, Lee A, George S, Hughes C. 3D microtumors in vitro supported by perfused vascular networks. Sci Rep. 2016.
89. Stringari C, Cinquin A, Cinquin O, Digman M, Donovan P, Gratton E. Phasor approach to fluorescence lifetime microscopy distinguishes different metabolic states of germ cells in a live tissue. Proc Natl Acad Sci U S A. 2011;108(33):13582-7.

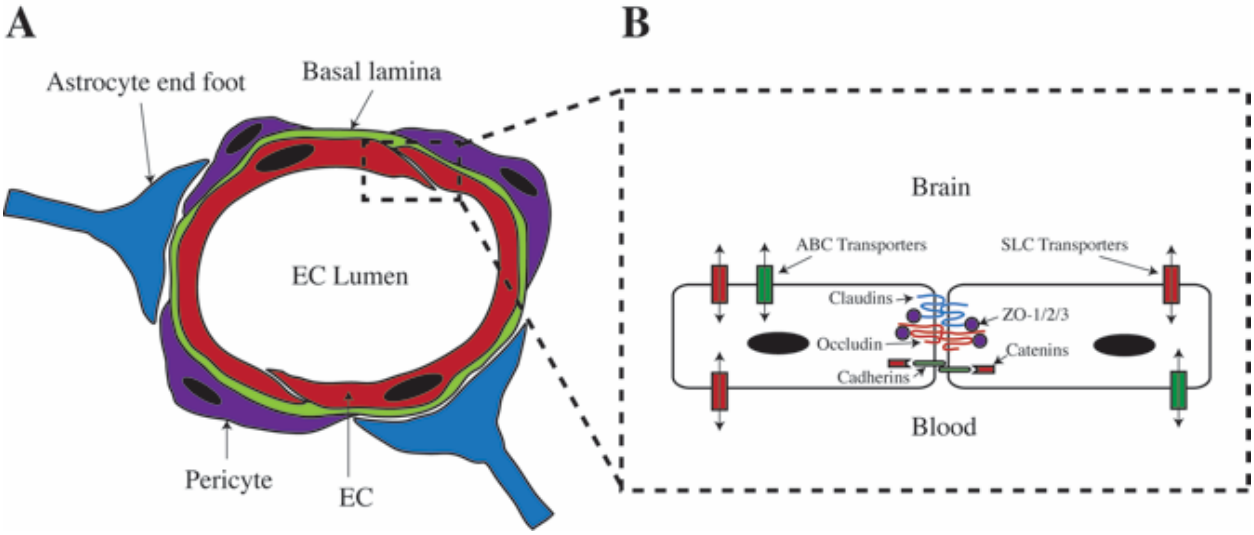

Figure S1: The human blood–brain barrier (BBB). (a) The human NVU consists of CECs forming the blood vessel, the basal lamina, pericyte, and astrocyte end foot. (b) Tight junctions, adherens junctions, SLC transporters, and ABC transporters of CECs.

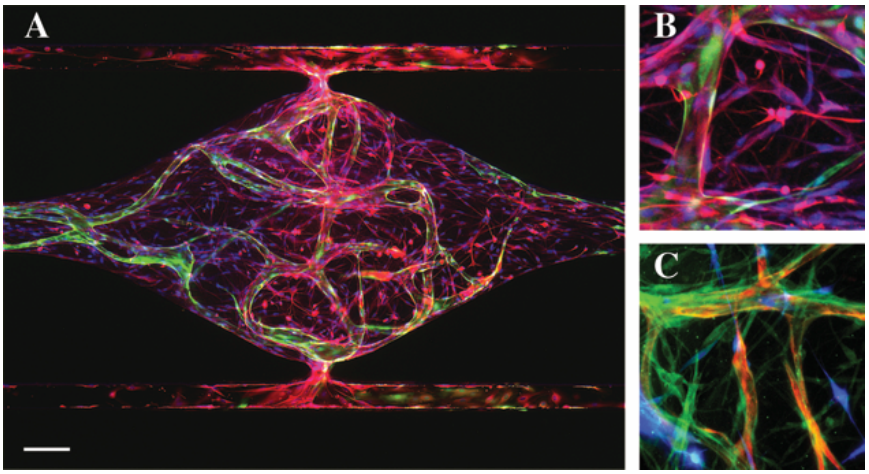

Figure S2: BBB-on-a-chip supported by living microvascular network. (a) Global view of astrocytes (GFAP – red) and the microvascular network formed by ECFC-EC (green) inside a tissue chamber. Nuclei were stained with DAPI (blue). Scale bar 1⁄4 100 mm. (b) Astrocytes (GFAP – red) lay down end feet and interact with the vessel (green). (c) Pericytes (PDGFR-b – green) wrap around the vessel (red) and interact with astrocytes (blue).

Year Published	Reference	Geometry/Dimension of blood vessel channel (width x height)	Endothelial Cell Source	Co-cultured Cells	TJ Qualitative Assessment	Transendothelial Electrical Resistance (TEER) Measurement	Permeability Test	Physiological Test	Shear Stress *
2016	Wang YI, et al (Ref #65)	Polycarbonate insert and micro-channel (300 μm x 160 μm)	Human iPSC-derived brain EC	Primary rat astrocytes (Life Technologies)	Claudin-5, ZO-1	2000-4000 $\Omega.cm^2$	4, 20, and 70 kDa dextran (0.5 mg/mL) = 10^{-7} to 10^{-8} cm^2/s	Exposure to small molecule drugs (caffeine, doxorubicin)	2-3 mPa
2016	Herland A, et al (Ref #66)	Square PDMS channel (1 mm x 20 mm) filled with collagen I gel to pattern a circular channel.	Primary human brain microvascular EC (Cell Systems)	Primary human brain pericytes (Cell Systems) + astrocytes (Sciencell)	VE-Cadherin, ZO-1	N/A	3 kDa dextran (5ug/mL) = 2-3 x 10^{-6} cm^2/s	Exposure to TNF-α	~100 mPa (5 minutes once a day)
2015	Brown JA, et al (Ref #67)	Rectangular PDMS channel (6.2 mm x 100 μm)	Primary human brain microvascular EC (Applied Cell Biology)	Primary human pericytes (Sciencell), astrocytes (ATCC), and human iPSC-derived glutamatergic neurons	ZO-1	1950-2210 $\Omega.cm^2$	10 and 70 kDa dextran (relative comparison)	Exposure to glutamate, ascorbate, cold shock	2 mPa
2015	Deosarkar SP, et al (Ref #68)	Rectangular PDMS channel (200 μm x 100 μm)	Primary rat brain capillary EC	Primary rat astrocytes	ZO-1	N/A	40 kDa dextran = 1.1-2.9 x 10^{-6} cm^2/s	N/A	0.38-7.6 mPa
2015	Sellgren KL, et al (Ref #69)	Rectangular PDMS channel (1 mm x 150 μm)	Immortalized mouse brain EC - bEnd.3 (ATCC)	Immortalized mouse astrocytes – C8D1A (ATCC)	Claudin-5	N/A	70 kDa dextran = ~ 9 x 10^{-7} cm^2/s	N/A	500 mPa
2015	Kim JA, et al (Ref #70)	Circular collagen gel channel (235-360 μm diameter)	Immortalized mouse brain EC - bEnd.3 (ATCC)	N/A	ZO-1	N/A	40 kDa dextran = 2.7 x 10^{-7} to 6.03 x 10^{-10} cm^2/s	Hyperosmotic exposure with mannitol	N/A
2013	Prabhakarpandian B, et al (Ref #71)	Rectangular PDMS channel (200 μm x 100 μm)	Rat brain EC (RBE4)	N/A (+Astrocyte conditioned media)	ZO-1, Claudin-1	N/A	3-5 kDa dextran (relative comparison)	Pgp efflux activity of Rhodamine 123 under Verapamil	3 mPa
2013	Achyuta AK, et al (Ref #72)	Rectangular PDMS channel (10 mm x 100 μm)	Rat brain EC (RBE4)	E18 neural cells	ZO-1	N/A	3 kDa dextran (relative comparison)	Exposure to TNF- α	N/A
2013	Griep LM, et al (Ref #73)	Rectangular PDMS channel (500 μm x 100 μm)	Immortalized human brain EC (hCMEC/D3)	N/A	ZO-1	37-120 $\Omega.cm^2$	N/A	Exposure to TNF- α	600 mPa
2012	Yeon JH, et al (Ref #72)	Rectangular PDMS channel (25 μm in height)	Primary HUVEC (Sciencell)	N/A (+Astrocyte conditioned media)	ZO-1	N/A	4, 40, 70 kDa dextran (relative comparison)	N/A	N/A

Table S1: Summary of current BBB organ-on-chips and their key features.

Note: "N/A" indicates no reported value or no measurement. Asterisk (*): Shear stress was reported in mPa, Pa, or dyn/cm^2. For simplicity, all reported values were converted to mPa. (1 dyn/cm^2 = 100mPa)

CHAPTER 5

A perfused neurovascular unit-on-a-chip platform to study neurovascular diseases

Duc T.T. Phan, Brianna M. Craver, Da Zhao, Jerry C. Chen, Koyinsola B. Oloja,
Abraham P. Lee, and Christopher C.W. Hughes

5.1 Abstract

The blood-brain barrier (BBB) is a dynamic and highly organized structure that strictly regulates molecular transportation between the brain vasculature and the central nervous system (CNS), and thereby protects the brain from toxins and infection. The BBB is formed by cerebral endothelial cells, pericytes, astrocytes, and the basal lamina that they share. Together, these four components form a neurovascular unit (NVU). *In vivo* rodent models are still considered the standard for studies on the BBB and related CNS diseases. While they have contributed significantly to new discoveries of BBB mechanics, their utility remains limited by physiological differences between humans and rodents, which often impede reliable translation to the clinic. With advances in microphysiological systems (MPS) and organs-on-a-chip (OOC) in recent years, there is a growing interest in developing BBB-on-a-chip models to better study CNS diseases, and evaluate patient-specific disease etiologies, with the ultimate goal of truly personalized therapies. With a vision to create an *in vitro* BBB model to study CNS diseases, we have developed a neurovascular unit-on-a-chip that incorporates perfused human blood vessels, a brain-like extracellular matrix environment, pericytes, and astrocytes. In this system, we observed natural formation of the NVU over the course of 7 days, and interactions of four components of the NVU similar to *in vivo*. Finally, we confirmed a tighter vascular barrier of the NVU compared to non-BBB vessels.

5.2 Introduction

The blood-brain barrier (BBB) is a dynamic and highly organized structure that strictly regulates molecular transportation between the brain vasculature and the central nervous system (CNS), and thereby protects the brain from toxins and infection [1]. The barrier results from a combination of extensive tight and adherens junctions between cerebral endothelial cells (CEC), which dramatically reduce the rate of transcytosis relative to vessels outside of the CNS. Additionally, both pericytes (PCs) and astrocytes, located on the abluminal side of the vasculature, provide critical support for this tight barrier [1]. Together, CEC, PC, astrocytes, and the basal lamina that they share form a neurovascular unit (NVU).

In vivo rodent models are considered the standard for studies on the BBB and related CNS diseases [2]. These models are useful to evaluate the pharmacodynamic and pharmacokinetics of potential pharmacologic agents in complex, living tissues. While they have contributed significantly to new discoveries of BBB mechanics, their utility remains limited by physiological differences between humans and rodents, which often impede reliable translation to the clinic [2-4].

The challenge remains in recapitulating the tight vascular barrier function *in vitro*. The standard *in vitro* system to study biotransportation across the BBB has been the Transwell assay, in which CEC are cultured on top of the Transwell membrane, while the PC and/or the astrocytes are cultured in the bottom chamber well, or on the reverse side of the membrane. However, this model has been proven to be ineffective to recapitulate the high selectivity of brain microvasculature *in vivo*. Part of this may well be due to the large separation between the CEC and the other cell types, something not seen in the physiologic NVU. Attempts to mimic the 3D *in vivo* environment are still limited to static co-culturing of CEC, PC, and astrocytes embedded

in extracellular matrix (ECM) [5]. Although there are interactions between each cell type in the ECM, the vasculature is not fully functional and no true BBB is formed.

With advances in microphysiological systems (MPS) and organs-on-a-chip (OOC) in recent years, there is a growing interest in developing BBB-on-a-chip models to better study CNS diseases, and evaluate patient-specific disease etiologies, with the ultimate goal of truly personalized therapies [6]. Over the past five years, we have significantly improved the methodology to generate perfused human microvascular networks in our OOC [7, 8]. With a vision to create an *in vitro* BBB model to study CNS diseases, we have developed a neurovascular unit-on-a-chip (NVUC) that incorporates perfused human blood vessels, a brain-like ECM environment, PC and astrocytes. In this NVUC, we observed natural formation of the NVU over the course of 7 days, and interactions of four components of the NVU similar to *in vivo*. Finally, we confirmed a tighter vascular barrier in the NVUC compared to our generic perfused vascular network model.

5.3 Materials and Methods

Platform fabrication

The microfluidic platform is fabricated as previously described [8]. Briefly, the PDMS device layer is casted in a custom-made plastic mold, punched holes for inlets/outlets, and bonded to a bottom-less, 96-well plate (Greiner Bio-One). Two PDMS membranes are then bonded to this well plate/PDMS device assembly to complete a microfluidic platform consists of 12 tissue units. The assembled microfluidic platform is sterilized using UV for 30 minutes prior to experiments.

Cell culture

Human endothelial colony forming cell-derived endothelial cells (ECFC-EC) are isolated from cord blood and expanded on gelatin-coated flasks in EGM-2 (Lonza) as previously described [7, 8]. The methods are carried out in accordance with the approved guidelines and with approval from UC Irvine's Institutional Review Board. ECFC-EC are used between passages 4-7. To induce a brain-like phenotype for ECFC-EC, cells are plated at 50% confluency and treated with 1 μM all-trans retinoic acid (Sigma-Aldrich) for 48 hours prior to loading into the microfluidic device. Normal human lung fibroblasts (NHLFs) are purchased from Lonza, cultured in DMEM (Corning) containing 10% Fetal Bovine Serum (FBS, Gemini Bio Products). While these cells in different lots all express perivascular cell markers (NG2, CD90, and PDGFR-β), there are considerable differences between lots, thus for further studies, cells that express higher level of these markers are characterized and selected using flow cytometry. Characterized and selected cells are then assigned as perivascular cells (PVC) used between passages 6-9. Astrocytes are differentiated from human neural stem cells as previously described

and used between passages 19-21 [9]. ECFC-EC, perivascular cells, and astrocytes are transduced with lentivirus to express fluorescent proteins (mCherry, GFP, or Azurite).

Loading of tissue chambers

Vascularized tissues are established in the platform as previously described [7, 8]. Briefly, cells are harvested and combined at their respective cell densities (ECFC-EC = 10^7 cells/mL, PVC = $5x10^6$ cells/mL, and/or astrocytes = $2.5x10^6$ cells/mL) in a mixture of ECM containing 80% volume of 10 mg/mL fibrinogen (Sigma-Aldrich), 10% volume of 1 mg/mL fibronectin (Sigma-Aldrich), and 10% volume of 1 mg/mL laminin (ThermoFisher). The cell-matrix mixture is quickly mixed in 3 U/mL thrombin and loaded into the tissue chambers of each unit on the platform. After allowing gel polymerization for 15 minutes, microfluidic channels were coated with mouse natural laminin (1 mg/mL, Thermo Fisher) for 15 minutes before replacing with cell culture medium EGM-2 (Lonza). Hydrostatic pressure is established at the inlet and outlet medium reservoir wells to generate laminar flow along the microfluidic channels and the interstitial flow across tissue chambers. Hydrostatic pressure is restored to initial levels, and flow direction is switched, every 24 hours to ensure constant culture medium flow and bi-directional cell stimulation. Medium is replaced every other day after embedding.

Gene expression analysis

Gene expression analysis is performed as previously described [8]. Briefly, the plastic cover underneath the platform is removed and the PDMS region containing the 3 tissue chambers is extracted using a biopsy punch-out. The punched-out piece is transferred into a 1.5 mL tube and resuspended in Trizol for cell lysis. Supernatant is then transferred into a new 1.5 mL tube to extract RNA, then purified with Turbo DNase (Invitrogen) for 20 minutes. Total purified RNA is

synthesized into cDNA using iScript cDNA Synthesis Kit (BioRad), and used for quantitative real-time polymerized chain reaction (qRT-PCR). Average cycle threshold (Ct) values are normalized to 18S expression levels and all samples are measured in triplicate. Primers are designed using PrimerQuest Tool and synthesized by Integrated DNA Technologies. Primer sequences are listed in the Table 6.1.

Immunostaining

The platform is fixed for immunostaining by perfusing 4% paraformaldehyde (PFA) through the medium inlet for 30 minutes at room temperature following by washes with PBS for 1 hour at room temperature, or overnight at 4^{o}C. The platform is inverted and the bottom polymer membrane is carefully removed and the tissue chamber regions is extracted using a biopsy punch-out. The extracted PDMS tissue unit is transferred into 24-well plate and immersed face-down in PBS. Each tissue unit is permeabilized for 20 minutes with 0.05-0.1% Triton-X100 diluted in PBS. After permeabilization, tissue units are blocked with 10% goat serum for 1 hour at room temperature. Each tissue unit are then incubated with primary antibodies (1:1000 dilution in 5% serum and 0.05% Triton-X100) overnight at 4^{o}C. After washing with PBS to remove excess primary antibodies, tissue units are incubated with goat secondary antibodies (1:2000 dilution in 5% serum and 0.05% Triton-X100) for 30 minutes before washing with DPBS. Nuclei is counter-stained with DAPI when needed. Finally, anti-fade solution is added on top of each tissue unit before mounting with a glass coverslip.

Vascular permeability quantification

Vascular permeability quantification is performed as previously described [7]. Briefly, medium is replaced by 10 kDa-FITC or 70 kDa FITC-dextran (Sigma-Aldrich) diluted in DPBS in the reservoir with highest hydrostatic pressure to a final concentration of 50 μg/mL, and allowed to perfuse through the microfluidic channel. An image of background fluorescent intensity is acquired prior to addition of the dye. After allowing FITC-dextran to fully perfuse the microvascular network, time-lapse images are acquired every 15 minutes for a time course up to 90 minutes. The diffusive component of the solute permeability coefficient P is calculated using the equation previously described by quantifying the background average fluorescence intensity (I_b), the initial average fluorescence intensity (I_i) step change after FITC-dextran influx reached equilibrium at the initial time point, and the final average fluorescence intensity (I_f) of 8 central regions of a tissue chamber. Two to three independent experiments for 10 kDa and 70 kDa permeability coefficient quantification are obtained for statistical analysis.

Statistical analysis

Data are shown as mean ± standard deviation unless otherwise stated. Estimated means, and standard deviation are calculated using Microsoft Excel. Comparison between experimental groups of equal variance is analyzed using Student's t-test or one-way ANOVA followed by Dunnett's test for multiple comparisons using GraphPad Prism 7.0. Number of replicates is indicated in the legends. The level of significance is set at $p < 0.05$.

5.4 Results

Establishing a neurovascular unit-on-a-chip:

ECFC-EC are a highly plastic cell type that can adapt to tissue-specific phenotypes depending on the microenvironment [9]. We have previously shown that ECFC-EC can form a good vascular network in our platform, and they can maintain a good barrier function *in vitro* [7]. We believe that ECFC-EC can be induced to adapt a brain-specific endothelial phenotype to replace primary brain EC in our system. All-trans retinoic acid (ATRA) is a metabolite of retinol (vitamin A) and it has been previously shown to induce blood-brain barrier properties in EC [10]. Thus, we took this approach to induce a brain-specific phenotype for the ECFC-EC. We plated ECFC-EC at 50% confluency and treated the cells with 1 uM ATRA (Sigma-Aldrich) for 48 hours. While a higher concentration of ATRA has been shown to further enhance brain-EC phenotype [10], we found it suppressed vascular formation in 3D (data not shown). For the control condition, we plated ECFC-EC at the same density without ATRA in cell culture medium. After treating cells with ATRA, we embedded the cell-matrix mixture into the microfluidic platform and monitored for 7 days. Figure 5.1 summarizes the experimental setup for the NVUC. For the control experimental setup, we embedded a standard vascularized micro-organ (VMO) platform as previously described [7, 8].

We observed vascular formation in the NVUC as early as Day 2 post-embedding, and the vascular network continued to mature over the course of 7 days similar to the control VMO. To monitor EC-astrocyte interactions in our NVUC, we transduced ECFC-EC and astrocytes with lentivirus to express fluorescence constitutively (ECFC-EC: mCherry, astrocytes: Azurite). Astrocytes stayed healthy post-embedding, proliferated, and migrated toward the newly formed vascular network. By Day 7 post-embedding, we can observe astrocytes tracking along and

extended their end-feet toward the vessels (Figure 5.2). To demonstrate that these vessels are fully perfusable, we introduced fluorescent micro-beads (2 um in diameter) to the medium inlet and allowed them to flow through the vascular network (Figure 5.2).

The human NVU consists of 4 components: the vasculature, PVC, astrocytes, and the basal lamina made of ECM proteins such as collagen IV, laminin, and fibronectin [11]. To demonstrate formation of a true neurovascular unit *in vitro*, we performed immunostaining on signature markers of brain-EC, PVC, and astrocytes in our NVUC after 7 to 10 days in culture. We observed high expression and localization of endothelial adherens and tight junction proteins (VE-Cadherin, Claudin-5, Occludin, and ZO-1) on the vascular network (Figure 5.3). Formation of endothelial tight junctions is a classic indicator of a BBB [1, 12, 13], and we were able to confirm this phenomenon in our NVUC. We have previously reported that in response to luminal flow, PVC (NG2+/CD90+) are recruited to the vascular network and subsequently wrap around the vessels, similarly to *in vivo* [1]. In our NVUC, we also observed PDGFR-β+ cells wrapped around the vessels, or located in close proximity to the vascular network (Figure 5.4A). Similar to our initial observation using fluorescent-tagged astrocytes, when we performed immunostaining for GFAP, an astrocyte-specific marker, we observed GFAP+ cells were closely associated with the vascular network and they extended end-feet toward the vessels (Figure 5.4B). Finally, we confirmed formation of the basal lamina by immunostaining of collagen IV and laminin, two major basement membrane proteins (Figure 5.4C and D). Based on these results, we concluded that the structural features of the human NVU can be recapitulated in our system.

Validating BBB functions in the NVUC

We first analyzed expression levels of BBB signature genes using RNA collected from the NVUC and VMO control tissues. We chose 2 EC junctional genes (CDH5, OCLN) and 3 transporter genes (SCL2A1, ABCB1, ABCC4) for qRT-PCR. As shown in Figure 5.5, we observed a significant increase in gene expression levels of all 5 genes from the NVUC sample compared to control samples. This finding is consistent with previously reported RNA-Seq data obtained from *in vivo* samples [12, 13].

An important hallmark of a BBB is its highly regulated barrier function that selectively controls transport of molecules into and out of the vasculature [1, 2, 6]. Unlike other organs in the body, passive diffusion of large molecules (>70 kDa MW) is highly restricted in the brain [1, 2]. To test the vascular barrier functions of our NVUC after 7 days in culture, we perfused 70 kDa FITC-tagged dextran through the media inlet and observed extravascular leakage over a time course of 90 minutes. As a control we used a standard VMO platform and a VMO platform using ECFC-EC that were treated with 1 μM ATRA. When we quantified vascular permeability of 70 kDa FITC-dextran in 3 conditions, we observed a significant reduction of leak in the NVUC compared to controls (Figure 5.6A). Similarly, when using a smaller molecular weight FITC-tagged dextran (10 kDa), we also found reduced vascular permeability in the NVUC (Figure 5.6B). While we have yet to observe in our NVUC platform a bigger difference in vascular permeability expected in a true BBB [2, 3], we were able to gain a tighter barrier function compared to our baseline VMO platform.

6.5 Discussion

Based on the experimental results, we have recapitulated the human NVU structure and its cellular interactions *in vitro*. In this NVUC, we have incorporated a living vascular network, PVC and astrocytes, all in a basement membrane protein-rich microenvironment. We were able to foster vascular network formation and interactions of PVC and astrocytes with the vasculature over the course of 7 days. In contrast to previous in vitro BBB models, this vasculature is a naturally formed, living capillary network in a 3D native ECM, without the need of pre-patterned techniques. In addition, the cells show close apposition as they do *in vivo*, which is very different to what is seen in, for example, Transwell-based systems. Using fluorescent immunostaining, we confirmed formation of endothelial tight junctions (claudin-5, occludin, and ZO-1) in the vascular network, which is a hallmark of a mature, tight vascular barrier found in the brain. In addition, we observed PVC wrapping around the vessels and astrocytes extending their end-feet to interact with the vascular network, similar to what has been previously reported *in vivo* [1].

We found that ATRA treatment drove ECFC-EC to a brain-specific phenotype, resulting in increases in BBB genes, a tighter barrier function, and thus lower vascular permeability in the NVUC. We observed significant increases in expression levels of BBB signature genes (CDH5, OCLN, SLC2A1, ABCB1, and ABCC4) in the NVUC compared to the VMO controls. When we test for vascular permeability using 10 and 70-kDa fluorescent dextran over 60 to 90 minutes, we observed a 3 to 4-fold difference in permeability coefficient compared to the generic VMO platform. While we have not been able to achieve a bigger difference in vascular permeability as reported *in vivo* [2, 3], we are certain that the vascular barrier functions can be further enhanced. It is possible that the effect of ATRA on ECFC-EC is transient, and that the 48-hours pre-

embedding treatment does not prolong after the cells are in the device. However, when we continuously supply the NVUC with cell culture medium containing ATRA, we observed ECM contraction and collapse (data not shown). We believe this is due to over-contraction of the PVC, and that the concentration of ATRA supplied to the cell culture medium has an adverse effect on these cells. Thus, further optimization is needed to reduce gel contraction while maintaining a good vascular barrier function in the NVUC.

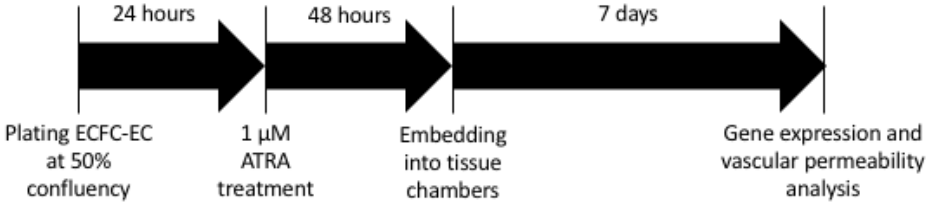

Figure 5.1: Experimental setup for the neurovascular unit-on-a-chip (NVUC). ECFC-EC are plated at 50% confluency and allowed to expand for 24 hours. Cells are then treated with 1 μM ATRA diluted in cell culture medium for 48 hours. After ATRA treatment, ECFC-EC are embedded into tissue chambers with perivascular cells, astrocytes, and brain-like extracellular matrix. Vascular networks are allowed to develop for 7 days prior to gene expression and vascular permeability analysis.

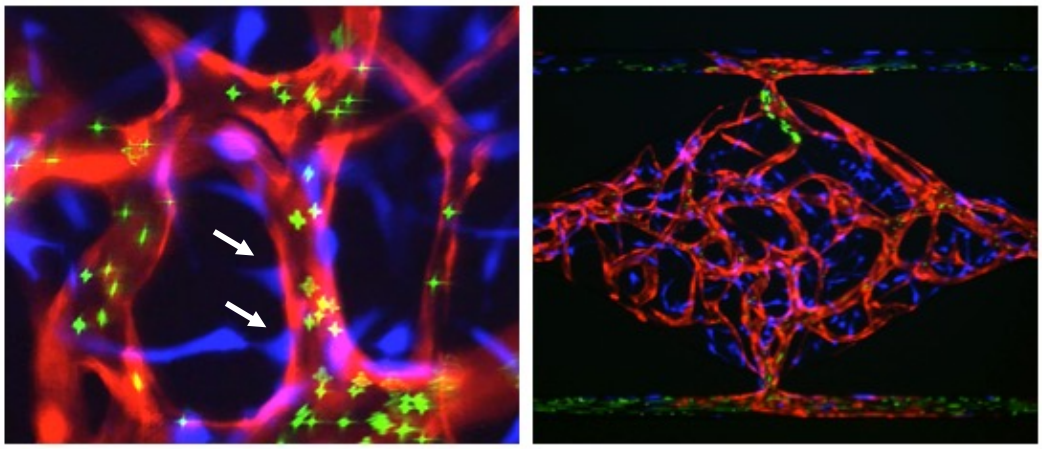

Figure 5.2: An *in vitro* human NVUC. ECFC-EC are transduced with lentivirus to express mCherry fluorescence, and astrocytes are transduced with lentivirus to express Azurite fluorescence. After 7 days in culture, a perfused vascular network is developed. Astrocytes-BFP (blue) are closely associated with the vasculature and extend their end-feet toward the vessel (white arrow). To demonstrate that the vascular network is fully perfusable, 2 μm FITC-tagged microbeads (green) are introduced into the medium inlet and allowed to flow through the vessels.

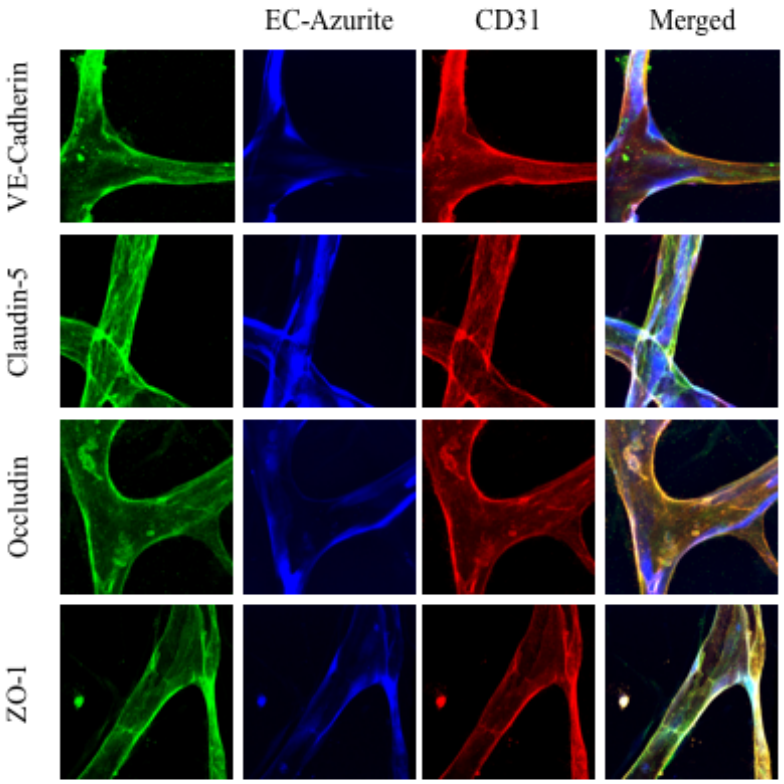

Figure 5.3: Endothelial adherens and tight junction expression and localization in the human NVUC. Immunostaining of endothelial junctional proteins VE-Cadherin, Claudin 5, Occludin, and ZO-1 (green) show localization to cell-cell appositions and the endothelial adhesion molecule CD31 (red). ECFC-EC are transduced with lentivirus to express Azurite fluorescence (blue).

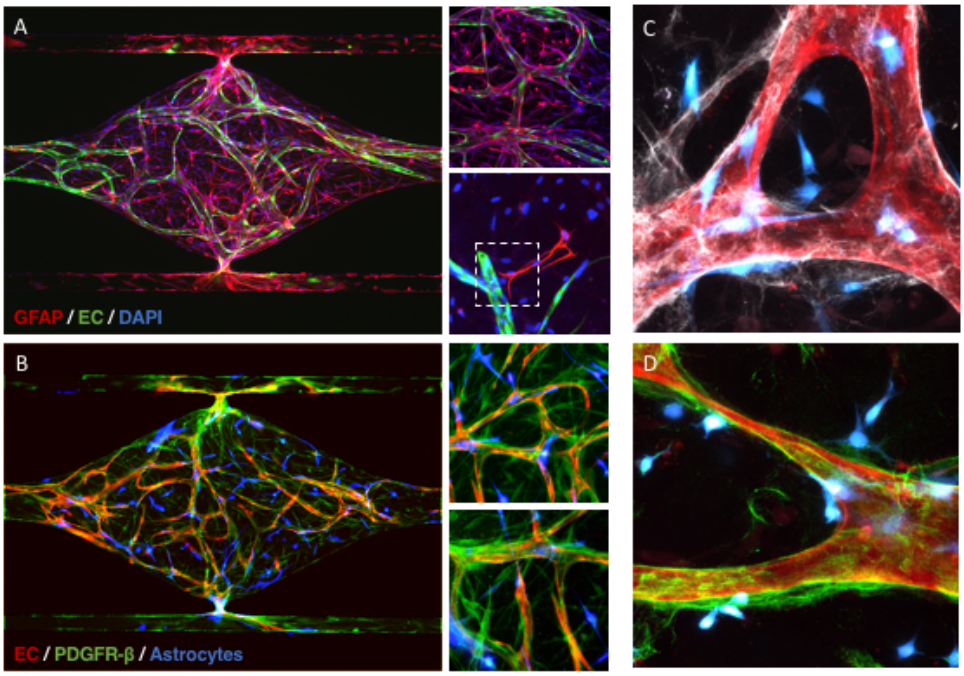

Figure 5.4: The presence of astrocytes, pericytes, and the basal lamina in the *in vitro* human NVUC. **(A)** Immunostaining of GFAP (red), a signature marker of astrocytes. Astrocytes are closely associated with the vascular network (green) and extend their end-feet to the vessels (white dash box). ECFC-FC are transduced with lentivirus to express GFP fluorescence **(B)** Immunostaining of PDGFR-β (green), a signature marker of pericytes. Pericytes wrap around the vessels (red) and interact with astrocytes (blue). ECFC-EC are transduced with lentivirus to express mCherry fluorescence, and astrocytes (GFAP+) are transduced to express Azurite fluorescence. **(C and D)** Immunostaining of collagen IV (white in C) and laminin (green in D), two major basement membrane proteins of the basal lamina. Collagen IV and laminin deposition are at the apical surface of the vessels. Astrocytes (blue) are closely associated with the vasculature and the basal lamina. Astrocytes are transduced with lentivirus to express Azurite fluorescence.

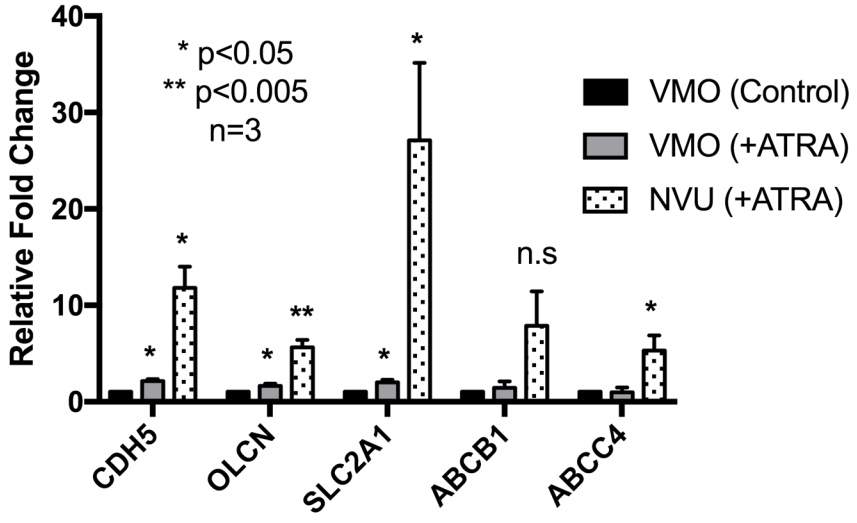

Figure 5.5: Gene expression analysis of BBB signature markers. Endothelial junctional genes (CDH5, OCLN) and transporter genes (SLC2A1, ABCB1, ABCC4) are highly expressed in the *in vitro* human NVUC. Data are shown as mean ± SEM of 3 biological replicates.

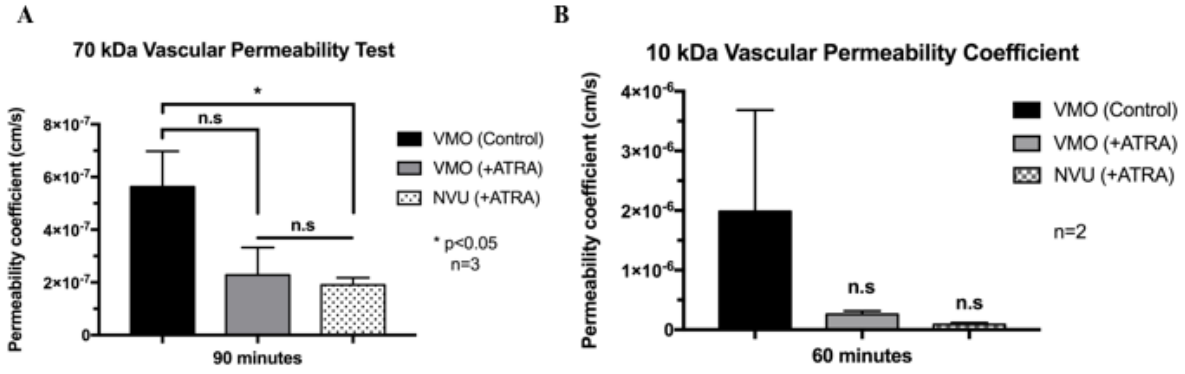

Figure 5.6: Vascular permeability analysis of the in vitro human NVUC. **(A)** Vascular permeability coefficient of 70-kDa dextran in the NVUC significantly reduces compared to the VMO controls (n=3 biological replicates). **(B)** Vascular permeability coefficient of 10-kDa dextran in the NVUC reduces compared to the VMO controls (n=2 biological replicates).

6.6 References

1. Daneman, R. and A. Prat, *The blood-brain barrier.* Cold Spring Harb Perspect Biol, 2015. **7**(1): p. a020412.
2. Abbott, N.J., *Prediction of blood-brain barrier permeation in drug discovery from in vivo, in vitro and in silico models.* Drug Discov Today Technol, 2004. **1**(4): p. 407-16.
3. Watanabe, K., et al., *In vivo assessment of the permeability of the blood-brain barrier and blood-retinal barrier to fluorescent indoline derivatives in zebrafish.* BMC Neurosci, 2012. **13**: p. 101.
4. Suzuyama, N., et al., *Species differences of inhibitory effects on P-glycoprotein-mediated drug transport.* J Pharm Sci, 2007. **96**(6): p. 1609-18.
5. Hopkins, A.M., et al., *3D in vitro modeling of the central nervous system.* Prog Neurobiol, 2015. **125**: p. 1-25.
6. Phan, D.T., et al., *Blood-brain barrier-on-a-chip: Microphysiological systems that capture the complexity of the blood-central nervous system interface.* Exp Biol Med (Maywood), 2017. **242**(17): p. 1669-1678.
7. Sobrino, A., et al., *3D microtumors in vitro supported by perfused vascular networks.* Sci Rep, 2016. **6**: p. 31589.
8. Phan, D.T.T., et al., *A vascularized and perfused organ-on-a-chip platform for large-scale drug screening applications.* Lab Chip, 2017. **17**(3): p. 511-520.
9. Arulmoli, J., et al., *Combination scaffolds of salmon fibrin, hyaluronic acid, and laminin for human neural stem cell and vascular tissue engineering.* Acta Biomater, 2016. **43**: p. 122-138.
10. Ferratge, S., et al., *Circulating endothelial progenitors in vascular repair.* Biomed Mater Eng, 2017. **28**(s1): p. S65-s74.
11. Lippmann, E.S., et al., *A retinoic acid-enhanced, multicellular human blood-brain barrier model derived from stem cell sources.* Sci Rep, 2014. **4**: p. 4160.
12. Thomsen, M.S., L.J. Routhe, and T. Moos, *The vascular basement membrane in the healthy and pathological brain.* J Cereb Blood Flow Metab, 2017. **37**(10): p. 3300-3317.
13. Hupe, M., et al., *Gene expression profiles of brain endothelial cells during embryonic development at bulk and single-cell levels.* Sci Signal, 2017. **10**(487).
14. Huntley, M.A., et al., *Dissecting gene expression at the blood-brain barrier.* Front Neurosci, 2014. **8**: p. 355.

CHAPTER 6

Discussion

7.1 Remarks

Over the past 5 years, substantial research and development in MPS and OOC technology have been made [1]. Various human tissue/organ models have been developed and validated against conventional *in vitro* and *in vivo* models with great success, and in certain cases MPS and OOC models have provided new insights on human physiological responses that have not been observed previously [2-6]. During this period, we and our collaborators have been contributing to this movement to overcome the status quo in studying human diseases and drug screening. From the original proof-of-concept on creating perfused vascular networks *in vitro* [7], we have: developed new methodologies to consistently generate perfused vascular networks that can support surrounding tissues; created vascularized micro-tumor models; and, resolved engineering challenges to scale up these systems to allow for moderately high-throughput drug screening applications [2, 8, 9].

We approached the development of our MPS/OOC from a biology-inspired perspective, as we believed that given an optimal microenvironment similar to the native tissue, cells can self-assemble into the native structure and regain their *in vivo* functions. While we utilized microfluidic technology and engineering approaches to develop our platform, we tried to promote a natural, self-assembled 3D microenvironment that would allow tissues to grow and develop. Leveraging our knowledge in creating blood vessels *in vitro* [10-15], we incorporated a vascular network into our platform via the processes of vasculogenesis and angiogenesis. More importantly, we made significant improvements in platform design and 3D cell culture techniques to promote anastomosis of the vascular network and the microfluidic system, such that nutrient delivery and waste removal depend on perfusion of this vasculature [8]. At this stage, tissue survival is entirely dependent on luminal flow through the vascular network similar

to *in vivo*. This *in vitro* vascularized microtissue became the baseline model for our subsequent research and development, and we keyed the term vascularized micro-organ (VMO) for this model.

After we were able to generate consistent vascularized microtissues *in vitro*, we turned our attention to solve challenges in scaling them up for drug screening applications. While others chose to connect their MPS/OOC platform to a pump system to generate fluid flow, we decided to use hydrostatic pressure to drive fluid flow in our platform. This allowed us to create a compact, self-contained system with full potential to scale up. Thus, we optimized the platform design that allows for 12 to 16 units to fit within a standard 96-well plate [9]. In this new platform, we were still able to generate highly consistent vascularized microtissues that are suitable for screening a small library of compounds [9].

While working on standardizing and scaling up our platform, we developed a vascularized micro-tumor (VMT) based on our baseline VMO model [2, 9]. As a proof-of-concept, we incorporated different cancer cell lines (e.g. colon, breast, skin and brain cancer cells) into the VMO platform, and used these micro-tumors to test anti-cancer drugs. When we validated dose responses of these VMTs against 2D screening assays and published *in vivo* data, we found that our VMT gave responses closer to *in vivo* [2]. In addition, with our VMT, we can distinguish anti-angiogenic and vascular disruption effects, a unique phenomenon that cannot be observed in traditional 2D screening [2]. More importantly, we were able to observe differential drug responses on the tumor, the associated tumor vasculature, or both [9].

As we continued to improve the VMO and VMT models, we started developing an *in vitro* model of the human neurovascular unit and the blood-brain barrier (BBB), in response to urgent needs for a better model to study diseases and drug delivery in the human central nervous

system (CNS) [16]. Building on our knowledge in MPS/OCC development, vascular biology, and neural stem cells, we have re-created the human neurovascular unit *in vitro*. We are currently optimizing and validating the vascular barrier functions of this model, in hopes that it will achieve true BBB properties. Successfully creating a true BBB *in vitro* model will provide a powerful tool to study human CNS diseases and drug delivery across the BBB.

7.2 Challenges and outlooks

While we have made significant progress in developing vascularized MPS/OCC within a short period of time, we recognize many challenges lying ahead that require our immediate attention and effort.

Platform development

At the current 96-well plate configuration with 12 to 16 tissue units and based on our statistical power calculation, screening a small library of 50-100 drug compounds is within capacity of our platform [9]. However, it is not feasible for high-throughput screening of hundreds to thousands of compounds. To achieve this capacity:

1. Platform manufacture needs to transition from a laboratory fabrication process to an industrial standard manufacturing process.
2. Platform handling and data processing require automation.

The platform is currently made of a silicone elastomer called Polydimethylsiloxane (PDMS) using soft lithography techniques. While this material is ideal for prototyping purposes, it is not suitable for industrial manufacturing process [17]. In addition, its inherent property of absorbing small hydrophobic molecules poses a major challenge to accurately determine effective doses of the screened compounds [18]. Thus, it is necessary to replace PDMS with a new class of thermoplastics that is optically clear, biocompatible and has low absorptivity for small hydrophobic molecules. Thermoplastics meet these criteria, and in addition are more compatible with industrial manufacturing processes such as hot embossing and injection molding, which will allow for large-scale platform manufacture at a lower cost [17].

In addition to manufacturing improvements, automation in platform handling and data processing is required. Currently, experimental procedures and data processing are performed manually or semi-manually by highly trained researchers. To achieve high throughput drug screening capacity, these steps will need to be performed by robotic systems. For instance, loading the cell-matrix mixture into the tissue chambers, changing cell culture media, and administering drugs to tissues can be automated with a liquid handling system. In addition, machine learning algorithms can be used to identify hit compounds and sort out false positives and false negatives in primary screens. Once hit compounds have been identified, highly trained researchers can make decisions on subsequent studies. Together with colleagues, we have been developing machine learning algorithms to identify hard-, soft-, or no-hit compounds that target the vascular network in our vascularized MPS/OOC (publication accepted).

Disease-specific and personalized MPS/OOC

At the current stage, cell sources used in our MPS/OOC come from primary isolations or commercial cell lines. These sources are limited, and often cannot truly represent disease-specific conditions. As we continue to improve our *in vitro* BBB model and develop new MPS/OOC, we recognize the importance of cell sourcing to overcome these limitations. With advances in induced-pluripotent stem cell and CRISPR/Cas9 gene editing technology, we can utilize these methods to generate disease-specific or personalized cell lines for use in MPS/OOC [19-21]. This will allow nearly unlimited cell sources for future research, and when coupled with advances in platform development and automation will unlock the full potential of high throughput screening at the personalized level.

7.3 References

1. Zhang, B. and M. Radisic, *Organ-on-a-chip devices advance to market.* Lab Chip, 2017. **17**(14): p. 2395-2420.
2. Sobrino, A., et al., *3D microtumors in vitro supported by perfused vascular networks.* Sci Rep, 2016. **6**: p. 31589.
3. Ronaldson-Bouchard, K., et al., *Advanced maturation of human cardiac tissue grown from pluripotent stem cells.* Nature, 2018. **556**(7700): p. 239-243.
4. Kim, H.J., et al., *Contributions of microbiome and mechanical deformation to intestinal bacterial overgrowth and inflammation in a human gut-on-a-chip.* Proc Natl Acad Sci U S A, 2016. **113**(1): p. E7-15.
5. Benam, K.H., et al., *Matched-Comparative Modeling of Normal and Diseased Human Airway Responses Using a Microengineered Breathing Lung Chip.* Cell Syst, 2016. **3**(5): p. 456-466.e4.
6. Barrile, R., et al., *Organ-on-Chip Recapitulates Thrombosis Induced by an anti-CD154 Monoclonal Antibody: Translational Potential of Advanced Microengineered Systems.* Clin Pharmacol Ther, 2018.
7. Moya, M.L., et al., *In vitro perfused human capillary networks.* Tissue Eng Part C Methods, 2013. **19**(9): p. 730-7.
8. Wang, X., et al., *Engineering anastomosis between living capillary networks and endothelial cell-lined microfluidic channels.* Lab Chip, 2016. **16**(2): p. 282-90.
9. Phan, D.T.T., et al., *A vascularized and perfused organ-on-a-chip platform for large-scale drug screening applications.* Lab Chip, 2017. **17**(3): p. 511-520.
10. Newman, A.C., et al., *The requirement for fibroblasts in angiogenesis: fibroblast-derived matrix proteins are essential for endothelial cell lumen formation.* Mol Biol Cell, 2011. **22**(20): p. 3791-800.
11. Newman, A.C., et al., *Analysis of stromal cell secretomes reveals a critical role for stromal cell-derived hepatocyte growth factor and fibronectin in angiogenesis.* Arterioscler Thromb Vasc Biol, 2013. **33**(3): p. 513-22.
12. Nakatsu, M.N. and C.C. Hughes, *An optimized three-dimensional in vitro model for the analysis of angiogenesis.* Methods Enzymol, 2008. **443**: p. 65-82.
13. Ghajar, C.M., et al., *The effect of matrix density on the regulation of 3-D capillary morphogenesis.* Biophys J, 2008. **94**(5): p. 1930-41.
14. Chen, X., et al., *Rapid anastomosis of endothelial progenitor cell-derived vessels with host vasculature is promoted by a high density of cotransplanted fibroblasts.* Tissue Eng Part A, 2010. **16**(2): p. 585-94.
15. Chen, X., et al., *Prevascularization of a fibrin-based tissue construct accelerates the formation of functional anastomosis with host vasculature.* Tissue Eng Part A, 2009. **15**(6): p. 1363-71.
16. Phan, D.T., et al., *Blood-brain barrier-on-a-chip: Microphysiological systems that capture the complexity of the blood-central nervous system interface.* Exp Biol Med (Maywood), 2017. **242**(17): p. 1669-1678.
17. Tsao, C.-W., *Polymer Microfluidics: Simple, Low-Cost Fabrication Process Bridging Academic Lab Research to Commercialized Production.* Micromachines, 2016. **7**(12): p. 225.

18. van Meer, B.J., et al., *Small molecule absorption by PDMS in the context of drug response bioassays.* Biochem Biophys Res Commun, 2017. **482**(2): p. 323-328.
19. Geraili, A., et al., *Controlling Differentiation of Stem Cells for Developing Personalized Organ-on-Chip Platforms.* Adv Healthc Mater, 2018. **7**(2).
20. Caballero, D., et al., *Organ-on-chip models of cancer metastasis for future personalized medicine: From chip to the patient.* Biomaterials, 2017. **149**: p. 98-115.
21. Low, L.A. and D.A. Tagle, *'You-on-a-chip' for precision medicine.* Expert Review of Precision Medicine and Drug Development, 2018. **3**(2): p. 137-146.